CHAPTER 7

THERMO-HYDRO-MECHANICAL ISOTROPIC RESULTS

7.1 Isothermal Suction Controlled Paths

7.1.1 Suction controlled swell or collapse / shrinkage under constant net mean stress

7.1.1.1 Testing results on the low-porosity packing

This chapter deals mainly with axially symmetric isotropic test results, however with the purpose of complementing the information of some plots, lateral stress oedometer results in terms of net mean stresses are also included. In some cases, the information corresponding to the deviatoric stress q is also indicated in the different diagrams, in order to have a better knowledge of the stress state and to clearly identify this type of oedometer results. The same stress state variables and work conjugate strain variables to those defined in section 6.1.1 and section 6.1.2 have been used. For axially symmetric conditions, the volumetric strain increment is defined as $\delta\varepsilon_v = \delta\varepsilon_1 + 2\delta\varepsilon_3$, while $\delta\varepsilon_s = 2(\delta\varepsilon_1 - \delta\varepsilon_3)/3$ stands for the shear strain increment, where $\delta\varepsilon_1$ and $\delta\varepsilon_3$ are the axial and radial strain increments, respectively. Main features of volume change behaviour were extensively described in chapter 6 and only complementary aspects are indicated in this chapter.

Several types of suction and stress paths have been followed, which are represented in Fig. 4.11, starting from an initial mean overconsolidation ratio of around 31. Fig. 7.1 shows time evolution of axial, radial, shear and volumetric strains, as well as water content and degree of saturation changes, that undergoes the soil sample upon applying a suction change starting from the initial condition to a final matric suction of 0.45 MPa under a constant isotropic net mean stress of $(\sigma_m\text{-}u_a)$=0.085 MPa and a constant temperature of 22ºC. Radial strain evolution corresponds to the intermediate part of the specimen, indicated with subscript 'c'. Strain ratio $\varepsilon_1/\varepsilon_{3c}$ evolution is also indicated for a complementary description of sample distortion upon main wetting. Isochrones of the progressive development of lateral profiles and radial strains at seven selected points of the specimen, as well as lateral strain average values throughout the sample height, are indicated in Fig. 7.4 following the sequence of the different stages represented in Fig. 7.1 with vertical dashed lines. These average values are also represented in Fig. 7.1, where no important differences due to end restraint effects from loading platens and wetting front advance are detected. However, inhomogeneous deformations are clearly detected as wetting front advances from both drainage ends. The degree of saturation evolution presented in Fig. 7.1 has been corrected taking into account the overall volume change determined form data presented in Fig. 7.4. A monotonic evolution of axial, radial and shear strains is observed for this stable packing upon main wetting.

Fig. 7.2 and Fig. 7.3 represent the equivalent plots for suction changes s_o = 0.45 MPa $\rightarrow$ s_f =0.20 MPa and s_o = 0.20 MPa $\rightarrow$ s_f =0.06 MPa, respectively. Isochrones of the progressive development of lateral profiles and lateral strains of the sample are indicated in Fig. 7.5 and Fig. 7.6 for the different stages represented with vertical dashed lines in the time evolution figures. An important aspect is the development of bulging at both ends due to the progressive advance of the wetting front, which is more remarkable in Fig. 7.5. This trend, which is still present in the following suction stage, tries to diminish as wetting fronts advance towards the central zone of the sample. This way, the electro-optical device allows to accurately detect irregularities and inhomogeneous deformation patterns throughout the sample height upon main wetting.

Results corresponding to the different equalisation stages in terms of axial, radial, shear and volumetric strains, as well as water content and degree of saturation changes, are indicated in Fig. 7.7, where main features of irreversible expansion upon main wetting and some irreversible shrinkage upon main drying are detected. Average lateral strains throughout the sample height have been considered; and shear and volumetric strains have been calculated based on these average lateral strain values, represented with hyphenated symbols. Differences between axial strains detected with both local LVDTs and associated with sample tilting, as well as differences between average radial strains, are also indicated, where no significant values are detected and where main differences are associated with the first wetting step. Shear strain development shows distortion of the sample upon main wetting, due to the anisotropic loading condition imposed to the specimen during static compaction leading to a preferential position of clay aggregates with their larger axis set horizontally. This way, higher swelling strains are expected in the axial direction, condition that is clearly observed in the experimental results. However, anisotropy decreases progressively upon suction induced plastic volumetric straining in the main wetting path at constant isotropic net stress, tending to a constant shear strain value of around -1.9% in the following drying-wetting cycle. In addition, strain ratio $\varepsilon_1/\overline{\varepsilon}_3$ increases during main wetting up to 1.5 and is maintained approximately constant upon subsequent main drying and scanning wetting paths, indicating that initial anisotropy has been completely erased. Further research work is needed to include these anisotropic phenomena induced by the fabrication history in an extension of the effects of the activation of the SD yield locus as defined by Gens and Alonso (1992), via some form of plastic behaviour inside the main yield surface or through a plastic anisotropy scaling function α mainly dependent on plastic volumetric strain and the current stress point: $\delta\varepsilon_s^p/\delta\varepsilon_v^p = \alpha(q/p, \varepsilon_v^p, \text{others})$. The progressive softening of soil sample upon main wetting due to irreversible swelling is also a relevant feature of behaviour, tending to a mean overconsolidation ratio of around 3 at the end of the wetting stage, calculated based on a yield stress of around 0.28 MPa detected in the following loading stage under nearly saturated states (refer to Fig. 7.20 and point A of Fig. 7.22).

Variation of volumetric strain, water content and degree of saturation changes obtained with the mini-isotropic cell (test series I17-0.085A in Table 4.3) and following the same wetting-drying cycles at the same net isotropic stress are also indicated in Fig. 7.7, where somewhat lower swelling strains and associated water content changes are detected upon main wetting. The differences can purportedly be associated with the different initial conditions of soil samples, where the specimen installed in the triaxial cell is expected to start from a somewhat higher suction due to the time required in the setting up process before the installation of the membrane (refer to section 4.4.2.2).

7.1.1.2   *Testing results on the high-porosity packing*

Several types of suction and stress paths have been followed, which are represented in Fig. 4.11, starting from a nearly normally consolidated state characterised by a mean overconsolidation ratio of around 1.2. Fig. 7.8 shows time evolution of axial, radial, shear and volumetric strains, as well as water content and degree of saturation changes, that undergoes the soil sample upon applying a suction change starting from the initial condition to a final matric suction of 0.45 MPa under a constant isotropic net mean stress of $(\sigma_m\text{-}u_a)$=0.600 MPa and a constant temperature of 22ºC. Radial strain evolution corresponds to both the intermediate part of the specimen (indicated with subscript 'c' and represented with solid lines) and to the average value throughout the sample height (indicated with hyphenated symbols and represented with dashed lines between selected points). Strain ratio $\varepsilon_1/\varepsilon_{3c}$ evolution is also indicated for a complementary description of sample distortion upon main wetting.

Isochrones showing the progressive development of the lateral profiles of the sample for the different stages indicated in Fig. 7.8 with vertical dashed lines are represented in Fig. 7.12a, using the technique described in section 3.3.4.2. These raw data are further transformed to lateral displacements

with reference to the initial configuration. For this purpose a program was developed to calculate these lateral displacements, based on determining the distance at a predetermined elevation (defined by the elevation points of the initial configuration) between the initial profile and the interpolation for the same elevation in the following sections. These data are further transformed to calculate the radial strains for the same specified elevations using the interpolated outputs from both transducers. Finally, a numerical integration is followed to calculate the average lateral strain representative of sample height at specific elapsed times. As observed in Fig. 7.12b, an inhomogeneous collapse deformation is developed along the specimen height as the wetting front advances, partially affected by end restraint effects of the porous stone platens tending to null deformation conditions at both ends. A striking aspect is that maximum collapse zone is shifted downward with respect to the mid-height of the sample, condition that can be probably associated with the non-uniformity of the static compaction procedure based on a volumetric criterion rather than on a maximum stress criterion (refer to section 4.3.2). The volume change determination taking into account the non-uniformity of the sample deformation is more representative of the whole specimen, specially when calculating degree of saturation changes. Fig. 7.16 shows the differences between measured mid-height radial strains and calculated average radial strains obtained from sample deformation profile considerations, where main differences appear in the first wetting stage. The same figure represents the influence of such differences in terms of void ratio and degree of saturation changes, assuming in the latter case that there is no error in water content estimation. Fig. 7.8 also represents degree of saturation, volumetric and shear strains calculated on a radial strain average basis, where systematically lower collapsible strains are reported compared to results obtained from a mid-height basis due to end restraint effects.

The volumetric evolution presented in Fig. 7.8 exhibits a dominant collapse as a result of the progressive wetting of the meta-stable aggregate packing, where a monotonic evolution of radial and shear strains is observed. However, at the beginning of the test some small swelling is recorded by the local LVDTs, before the macroscale contacts between aggregates become weaker and fail under local shear causing the macrostructural collapse. The transition between expansion and collapse behaviour is depicted in Fig. 7.15, using retention curve data presented in Fig. 5.22 and assuming that local equilibrium between liquid and vapour phases is reached despite the transient wetting stage. The transition is obtained at an estimated value of 1.4 MPa, which is represented with respect to the loading-collapse LC yield locus of the original packing and indicated by point C in Fig. 7.22. This yield locus is further dragged along during imbibition originating a macrostructural strain hardening of soil structure.

Differences between axial strains registered with both local LVDTs are represented in Fig. 7.15, where some sample tilting is detected in the main wetting phase with no significant consequences on further drying and wetting paths. Differences between both laser sensors are also indicated in the figure, where no significant values are detected and where main differences are associated with the first wetting path.

Shear strain development as indicated in Fig. 7.15 shows distortion of the sample upon wetting during the activation of the LC yield locus, due to the anisotropic loading condition imposed to the specimen during static compaction and originating a preferential fabric (transversally isotropic) in order to provide the greatest possible resistance to the applied stresses. This material anisotropy is further erased upon suction induced plastic straining at constant isotropic net stress, tending to align the main q : p yield curve to the current isotropic stress state and displaying and nearly isotropic evolution in further main drying and scanning wetting paths. The ratio of axial to lateral strain observed upon wetting increases progressively up to a maximum value of around 0.8 (average basis value), while shear strain increases up to a maximum absolute value of 0.4% (average basis value), which are both maintained throughout the main drying and scanning wetting paths.

It is expected that asymmetric yield curves and a non-associated flow rule induced by the one-dimensional fabrication stress history, tend progressively to the symmetric and elliptical constant suction yield curves in q : p plane with an associated flow rule as proposed by Alonso *et al*. (1990) and suggesting some form of rotational/kinematic hardening. Maâtouk *et al*. (1995) and Cui and

Delage (1996) presented data from unsaturated soils with anisotropic stress histories, which show constant suction yield curves in q : p plane inclined along the K_0 line, following a similar form to that of saturated anisotropic natural clays (Graham *et al.*, 1983). Cui and Delage (1996) suggested that lateral stress oedometer results at constant water content could be appropriate to evaluate the inclination of the elliptical q : p yield curves for axially symmetric static compacted samples. However, it appears that the angle of inclination may be somewhat dependent on suction as observed in Fig. 2.14, which shows some dependence of K_{0nc} with degree of saturation. Hueckel and Tutumluer (1994) and Wheeler (1997b) have proposed for saturated clays elliptical yield surfaces inclined at an angle corresponding to the K_0 compression line, which undergo a combined growth and rotation, depending usually on plastic volumetric and shear strains and their history. As indicated by Wheeler (1997b), the hardening law for changes of inclination of the yield curve assumes that plastic volumetric strains have the effect of aligning the yield locus about the current stress point, whereas plastic shear strains have the effect of erasing anisotropy and rotating the curve towards an isotropic orientation. In addition, Hueckel and Pellegrini (1996) have extended the framework of Hueckel and Borsetto (1990) to propose a rotational strain hardening thermoplastic model to analyse thermo-mechanical anisotropy of natural clays. Further research work is needed to assess the properties of anisotropic one-dimensionally compacted or consolidated clays related to unsaturated and thermal states. This way, it appears adequately enough to accept similar volumetric and rotational hardening laws to those under saturated conditions dependent on plastic volumetric and shear strains, irrespective of their origin (mechanical loading, suction or temperature) as a first tentative or admitting certain weighting functions as more experimental evidence is available. In addition, consequences on elastic moduli and thermal expansion coefficients dependent on the accumulated plastic pre-strain history are required to be considered following the concepts of elastoplastic coupling detailed in Hueckel and Tutumluer (1994) and Hueckel and Pellegrini (1996).

Fig. 7.9 and Fig. 7.10 represent the equivalent plots for suction changes $s_o = 0.45$ MPa $\rightarrow s_f = 0.20$ MPa and $s_o = 0.20$ MPa $\rightarrow s_f = 0.06$ MPa, respectively. Isochrones of the progressive development of lateral profiles and strains of the sample are indicated in Fig. 7.13 and Fig. 7.14 for the different stages represented in the time evolution figures with vertical dashed lines, where lower differences between the central zone and the average values are detected (refer to Fig. 7.16). A striking effect is certain tendency that systematically is observed in early stages corresponding to some swell detected by the local LVDTs, despite that the stress path has already reached the yield state. This way, it is expected that certain increase in the entrapped air pressure be developed during the early stages of the transient wetting phase inducing some small net stress unloading on the sample. This effect is more important at higher degrees of saturation, where entrapped air overpressure is more difficult of releasing. A further numerical simulation is required to analyse entrapped air overpressure effects due to wetting front advance from both drainage ends.

Time evolution of axial, radial, shear and volumetric strains in a main drying step ($s_o = 0.20$ MPa $\rightarrow s_f = 0.45$ MPa) are indicated in Fig. 7.11, where shear strain and strain ratio evolutions show a clear isotropic shrinkage. No important degree of saturation changes are detected, signifying that the air-entry value of the packing has not been surpassed and where water content changes and volumetric strains are coupled provided that the soil remains in a nearly saturated state.

7.1.1.3   *Compressibility aspects using DDL theory under nearly saturated conditions*

This section presents a simple mechanical-physicochemical model governing the behaviour of elastic volumetric strains under nearly saturated states based on mechanical effects acting at macroscopic scale and the balance of physico-chemical interactions between clay particles and the inter-aggregate pore solution. The following formulation is only used to derive a compressibility expression in terms of certain pore solution properties determined in section 2.2.2 and the specific surface and gravity of

solid particles, conscious of the limitation of incorporating parameters describing physico-chemical changes at microscale with macroscale mechanistic parameters in a single stress state variable.

Following Lambe's definition in a parallel connection or strain compatibility model (Hueckel, 1992a,b), intergranular stress is defined according to $p + \chi s \approx R_p - A_t$, which only includes long-range electrochemical forces per unit area with no mineral-mineral interparticle contact (strictly applicable to active clays at low confinements and nearly saturated states). R_p is associated with dominant double-layer repulsion due to the interaction between particles through water (Sridharan and Jayadeva, 1982; Mitchell, 1993) and A_t to long-range van der Waals electrostatic attractions, which are essentially independent of fluid properties between particles. Allam and Sridharan (1987) proposed a single-valued effective equation for unsaturated states including osmotic suction arising from long-range electrical surface forces and contractile skin stress constituents. Following Sridharan and Venkatappa Rao (1973), their approach was based in a mechanistic parallel connection model for intergranular stress, where long-range repulsion forces and intergranular stresses are connected in parallel, being in addition set in parallel with bulk water pressure. An extensive analysis of the deformation induced in clay by mechanical actions or changes in the permeant chemistry in terms of different mechanistic models for effective stress is presented in Hueckel (1992b).

R_p stresses between parallel particles can be estimated from the osmotic pressure between the inter-aggregate pore fluid concentration and the ionic concentration between particles (Mitchell, 1993; Iwata *et al.*, 1995). Equations derived from interacting diffuse double layer DDL theory can be applied to separations of solids larger than 20 Å (distant from the Stern layer), corresponding to adsorbed water contents higher than 16 % for illites (Hueckel, 1992b), although the trends resulting from DDL theory also appear to be valid for smaller interstices (Sposito, 1984). An alternative to osmotic pressure relationships with DDL theory is to use water adsorption theory (Low, 1980). Zhang *et al.* (1993) studied the effect of temperature on the swelling of montmorillonites based on this theory. Following the osmotic pressure concept, the equilibrium requirement is that the chemical potential of the pure water midway between parallel clay platelets and that of the free solution in inter-aggregate pores must have the same value. This equality of the chemical potential is achieved by a pressure difference, which at the same time is related to the external mechanical effect $p+\chi s$, assuming negligible A_t as further indicated and that the solution contains a single symmetrical electrolyte with cation c^+ and anion c^- species of the same valence:

$$p + \chi s = RT\left(c_{mp}^+ + c_{mp}^- - c_o^+ - c_o^-\right) \quad \text{with} \quad c_{mp}^- = c_o e^u \; ; \quad c_{mp}^+ = c_o e^{-u} \quad \text{and} \quad c_o = c_o^+ = c_o^-$$
$$p + \chi s = 2RTc_o\left(\cosh u - 1\right) \approx RTc_o u^2 \; ; \quad p + \chi s \approx RTc_o u^2 \tag{7.1}$$

where u is the non-dimensional midplane electrical potential function for interacting double layers in a parallel clay platelet system (Mitchell, 1993) and the approximation of the power series is sufficiently adequate for $c_o > 100$ mol/m^3 as suggested by Sridharan and Jayadeva (1982) (implying u < 0.630 for $R_p = 100$ kPa and T = 293K), which is the case for Boom clay pore fluid according to squeezing technique results presented in section 2.2.2. This interacting double layer midplane potential function can be expressed in terms of the dimensionless potential function z at the surface of the clay plate as (Sridharan and Jayadeva, 1982; Komine and Ogata, 1996a):

$$u = 8\tanh^{-1}\left[e^{-d/(2\vartheta)}\tanh(z/4)\right] \approx 8e^{-d/(2\vartheta)}\tanh(z/4); \quad \vartheta = \sqrt{\frac{\varepsilon_o \varepsilon_r RT}{2F^2 c_o \nu^2}} \tag{7.2}$$

where ϑ is the Debye's length or a measure of the thickness of the double layer (Yeung, 1992; Mitchell, 1993; Iwata *et al.*, 1995), and the approximation holds for low midplane potential values. Other parameters involved in these relationships are the permittivity of vacuum $\varepsilon_o = 8.85 \times 10^{-12}$ C^2/(J.m), the relative dielectric permittivity of the pore fluid $\varepsilon_{ro} = 80.4$ at $T_o = 293$K ($\varepsilon_r \approx 80.4$-

0.364(T-T$_o$); T in K), Faraday's constant F = 9.64×10^4 C/mol and the valence of the prevailing ion ν. Typical values of ϑ for Boom clay fabric assuming a pore water with c$_o$ = 100 mol/m^3 and a dominating Na$^+$ system (refer to section 2.1.1) are 0.97 nm at T = 293K and 0.90 nm at T = 353K, where no appreciable temperature effects are observed.

The surface charge density σ (in C/m^2) of Boom clay minerals can be estimated by knowing the cation exchange capacity in meq/100g (CEC ≈ 40 meq/100g as indicated in section 2.2.1.2) and the specific surface in m^2/g (S$_s$ ≈ 40 m^2/g), by means of the following expression (Mitchell, 1993; Shang *et al.*, 1994; Komine and Ogata, 1996a): $\sigma = 0.964 \, CEC / S_s \approx 0.964 \, C/m^2$. This surface charge density is related to a dimensionless potential function of 7.89, which is associated with $\tanh(z/4) \approx 1$ at a surface potential of 199 mV, disregarding the formation of the Stern layer and its shielding effect (for further details refer to Yeung, 1992; Shang *et al.*, 1994). The following expression: $p + \chi s \approx 64RTc_o e^{-d/\vartheta}$ is obtained combining Eq. (7.1) and Eq. (7.2) with the above approximation.

According to Santamarina and Fam (1995) and Fam and Santamarina (1996) two solutions can be utilised for long-range repulsion stress for parallel particles depending on interparticle distance d:

$$R_p = 64RTc_o e^{-d/\vartheta} \quad \text{for l arg e int er – particle distances} \quad d/\vartheta > 3; \quad \text{and}$$

$$R_p = 2RTc_o \left(\frac{2\pi^2\vartheta^2}{d^2} - 1 \right) \quad \text{for short int er – particle distances} \quad d/\vartheta < 2 \tag{7.3}$$

where the first expression is equivalent to the previous expression and to that proposed by Israelachvili (1991), assuming that the dimensionless surface potential z is high and that particles are sufficiently far apart so that the midplane potential u is low (weak overlap approximation). It is also admitted that the interparticle limit proposed in the above equation be compatible with assumptions imposed during the derivation of the first expression. The second expression is equivalent to that derived by Yong and Warkentin (1975). In addition, both equations predict similar values for $d \approx 2\vartheta$. At an equivalent interparticle distance of $d = 3\vartheta$ and T = 293K, the long-range repulsion or intergranular stress is associated with a value of 0.80 MPa (refer to Fig. 7.17). Long-range attraction A$_t$ at this interparticle distance can be estimated by means of the following expression (Sridharan and Jayadeva, 1982; Iwata *et al.*, 1995; Komine and Ogata, 1996a): $A_t = A_h / (6\pi d^3) \approx 0.06 MPa$, where A$_h$ is the Hamaker constant (around 3×10^{-20} J for kaolinite minerals) that is admitted to be only slightly sensitive to changes in concentration and in interparticle distances (Santamarina and Fam, 1995). As observed, the long-range attractive force is relatively small compared to the repulsive force caused by interaction of diffuse double layers.

On the assumption that particles are aligned parallel to each other and at nearly saturated states (χ→1), the void ratio e is related to the interparticle distance d through the specific surface S$_s$, the specific gravity of solid particles Gs and the density of free water ρ$_w$ at a reference temperature, as follows:

$$e = S_s Gs\rho_w d/2 \approx S_s Gs\rho_w \vartheta \ln[64RTc_o/(p+s)]/2 \quad \text{for} \quad p+s < 0.80 \, MPa$$

$$\delta\varepsilon_v^e \Big|_{\substack{T=const \\ c_o=const}} = \frac{\kappa}{(1+e_o)} \frac{\delta(p+s)}{p+s}; \quad \kappa = S_s Gs\rho_w \vartheta/2 \approx 0.05 \quad \text{at} \quad T = 22°C \tag{7.4}$$

where a non-linear elastic behaviour is considered characterised by a reference interparticle configuration and an elastic parameter κ dependent on specific surface and gravity of solid particles, pore fluid properties, concentration and valence of the prevailing ion. However, DDL prediction at higher temperatures reports somewhat lower κ values under the assumption that all the effects are

induced on Debye's length, which is not consistent with experimental observations. Mitchell (1993) has shown that including thermal effects on dielectric constant, the double layer thickness should be unaffected by temperature. On the other hand, Morin and Silva (1984) supported and opposite thesis on high-porosity clays, suggesting a reduction of double layer thickness.

Fig. 7.17 shows reversible changes in volumetric strain associated with changes in intergranular mean stress obtained from isotropic (constant (σ_m-u_a) data) and oedometer (constant (σ_v-u_a) data) results for both packings, compared to Eq. (7.4) prediction based on an average reference configuration of $e_o = 0.760$ representative of these packings. Examination of experimental results compared to DDL prediction shows some validity at least qualitatively of these concepts in the prediction of e - (p+s) relationships. The following interpolation is obtained for test results (indicated with thicker lines and letter A): $\delta\varepsilon_v^e / \delta(p + s) = 0.0270/(p + s)$, which is associated with $\kappa \approx 0.043$ assuming a reference $e_o = 0.590$ corresponding to the high-density packing. This value is somewhat higher if compared to isotropic unloading results performed on the high-density fabric and indicated in Fig. 7.20. However, the general trend of obtaining systematically higher pre-yield compressibility parameters under isotropic conditions is detected, condition that is equivalent to the one obtained in the Fig. 6.50 and Fig. 6.59. Another type of interpolation (represented with letter B) has also been adopted following the proposal of microstructural elastic volumetric strains outlined in Gens (1993): $\delta\varepsilon_v^e / \delta(p + s) = 0.561\exp[-6.04(p + s)]$, where intergranular stress is expressed in MPa (equivalent interpolations for oedometer results are presented in Eq. (6.10)).

Isothermal reversible changes in work conjugate extensive variable of matric suction with changes in intergranular mean stress under nearly saturated conditions are presented in Fig. 7.18, where the following interpolation fits isotropic (constant (σ_m-u_a)) and oedometer data (constant (σ_v-u_a)): $[G_s/(1 + e_o)]\delta w_e / \delta(p + s) = -0.058/(p + s)$. A higher compressibility parameter in terms of water content changes is obtained from the previous curve fitting results (associated with $\kappa_w \approx 0.092$ assuming a reference $e_o = 0.590$ corresponding to the high-density packing) if compared to the volumetric compressibility, purportedly related to the lower readability of the experimental setup with reference to water content changes. As indicated in Fig. 7.20, similar pre-yield compressibility values in terms of water content changes and skeleton deformation are expected.

7.1.2 Loading-unloading paths under constant suction

Net stress increase and decrease steps under constant (u_a-u_w) = 0.20 MPa and after a main wetting and drying path were carried out on the low-porosity fabric and in the mini-isotropic cell, following the test procedures detailed in section 4.2.1.2. Variations of specific volume v, state variable Gs.w and degree of saturation with net mean stress are shown in Fig. 7.20, where clear pre and post-yield zones are detected. Yield stresses are identified based on strain energy concepts (volumetric strain and water content incremental work input per unit volume), according to Eq. (6.20) and Eq. (6.21). The limit between pre and post-yield domains is in agreement for both volumetric strain and water content change considerations. Typical compressibility parameters are also indicated in the previous figure: $\kappa \approx 0.018$ and $\lambda(s) \approx 0.074$, where somewhat higher values compared to that under oedometer conditions are reported (refer to Fig. 6.50). The value of the parameter associated with water content changes in the post-yield zone is slightly lower ($\lambda_w(s) \approx 0.054 < \lambda(s)$), presenting the same value under pre-yield conditions ($\kappa_w \approx 0.018$), in accordance to model predictions as proposed by Wheeler (1996) (refer to section 6.4.1) and experimental results of Zakaria (1995) for isotropic unloading tests at constant suction. For an estimated value of $\lambda(0) \approx 0.080$ (refer to equivalent oedometer results presented in Fig. 6.57), the parameter indicated in Eq. (6.22) is around $\alpha(0.20\text{MPa}) \approx 0.018 < \lambda(0)$-$\kappa$, which presents an adequate agreement with results indicated in section 6.4.1 and section 6.4.2. The evolution of the degree of saturation exhibits an increasing trend in the post-yield zone, while it is nearly constant in the pre-yield stages, in accordance to oedometer results presented in Fig. 6.50 and Fig. 6.59, and as a consequence of the higher efficiency of loading effects in deforming soil skeleton

than expelling water. Yield point in relation to the loading-collapse LC yield locus of the original high-density packing obtained from static compaction and isochoric swelling pressure tests is presented in Fig. 7.22, where a dominating strain softening induced on main wetting is detected (yield point A at the left of the original packing). An adequate agreement in terms of stress state at yielding is obtained when comparing to the loading path at the same suction performed on the high-density fabric in the lateral stress oedometer cell and indicated with letter B in Fig. 7.22.

Fig. 7.19 shows the loading path A-B followed by the high-porosity packing at constant $(u_a-u_w) = 0.20$ MPa after a main wetting and drying path (refer to Fig. 4.11). Yield point is identified at around 0.70 MPa, which is also indicated with letter D in Fig. 7.22 with respect to the LC yield locus of the original packing, where a dominating strain hardening induced by the dragging of this yield locus upon main wetting is detected. The progressive development of specimen profiles and lateral strains throughout the specimen height is indicated in Fig. 7.21 at the end of each loading step, where a relative uniform pattern is recorded with no differences between mid-height and average values.

LC yield curves for the different packings obtained from static compaction and suction controlled isochoric test considerations are presented in Fig. 7.22, which have been fitted to the expression indicated in Eq. (6.24) to take into account aggregate deformability and strength at high suction values. Lateral stress states after compaction have been estimated assuming $K_{0nc} \approx 0.39$ for the high-density fabric (refer to Fig. 2.13) and a value of $K_{0nc} \approx 0.37$ for the high-porosity packing (refer to Fig. 2.12). As observed in Fig. 7.22, increasing fabrication stresses are required as total suction is increased in the 'intra-aggregate governing suction' zone (total suction values higher than 2 MPa), condition that is more remarkable in the high-density fabric. The same γ parameters, which control this rate of stiffness in the high-suction zone, to those obtained in section 6.4.1 and section 6.4.2 have been considered: $\gamma \approx 0.015$ for the high-density packing and 4.1×10^{-3} for the high-porosity fabric.

Admitting $(\sigma_m - u_a)_o^* = 0.7\,\mathrm{MPa}$, $(\sigma_m-u_a)^c = 0.1$ MPa and $s_{min} = 0.01$ MPa, the following parameters are obtained for the low-porosity fabric using a non-linear curve-fitting algorithm (least-squares method with some restrictions on compressibility coefficients): $\lambda(0) \approx 0.080$, $\kappa \approx 0.020$, $r \approx 0.739$ and $\beta \approx 1.019\,\mathrm{MPa}^{-1}$. As observed, differences in terms of net mean stresses compared to net vertical stress data are reflected in pre- and post-yield compressibility parameters displaying somewhat higher values in accordance to results presented in Fig. 6.50, as well as in r parameter (a somewhat higher value compared to vertical stress data) and β parameter (a somewhat lower value compared to vertical stress data). For a saturated net mean overconsolidation stress of $(\sigma_v - u_a)_o^* = 0.12\,\mathrm{MPa}$, $(\sigma_m-u_a)^c = 0.05$ MPa and equal reference suction s_{min}, the following parameters are obtained for the high-porosity packing: $\lambda_{oed}(0) \approx 0.110$, $\kappa \approx 0.020$, $r \approx 0.460$ and $\beta \approx 2.749\,\mathrm{MPa}^{-1}$. In this case, a lower post-yield compressibility parameter to that under net vertical stress considerations (refer to Fig. 6.67) has been selected, in accordance to the lower post-yield compressibility value detected in path A-B of Fig. 7.19. Main differences in terms of porosity effects are reflected in the post-yield compressibility parameter, in parameter r (decreasing with increasing porosity), parameter β (increasing with increasing porosity) and parameter γ (decreasing with increasing porosity).

7.2   Non-Isothermal Suction Controlled Paths on the High-Porosity Packing

7.2.1   General aspects and pore pressure build-up under quasi-undrained heating

7.2.1.1   *General aspects and testing results*

Heating-cooling cycles have been conducted under constant net isotropic stress and controlled matric suction to investigate reversible, irreversible and distortion features of volume change behaviour. In general, magnitudes of applied temperature corrections on zero and sensitivity shift are such that axial

strains are determined with somewhat higher precision and lower bias than lateral strains (refer to section 3.3.3 and section 3.3.4 for further details). The sample at a normally consolidated state was subjected to drained heating-cooling cycles (path B-C-D-E-F in Fig. 7.19 and Fig. 4.12) at a constant matric suction of $(u_a$-$u_w) = 0.20$ MPa and under a constant isotropic net mean stress of $(\sigma_m$-$u_a) = 1.00$ MPa, following the test procedures indicated in section 4.2.1.2.

Experiments are initially not true drained tests with restricted drainage due to soil permeability and ceramic disc impedance effects. A decrease in matric suction due to water pressure build-up, or in equivalent terms a decrease in intergranular (or effective) stress under nearly saturated states, is expected during this initial quasi-undrained stage. It is assumed that this analogous to unloading (or wetting) stage takes place under reversible conditions without appreciable yielding, where equal expansions in all directions are observed in Fig. 7.24 due to the isotropic stress state and isotropic sample properties that prevail in the specimen after the important plastic straining history that the sample has undergone up to the present state. This way, at every temperature rise, the sample initially dilates but afterwards in the main drained heating path a nearly isotropic compression is observed during pore pressure dissipation due to thermal collapse phenomenon associated with the loss of shear strength of the contacts between aggregates. In addition, the progressive loss of intra-aggregate water with increasing temperatures affecting intercluster voids may also induce further compression. Fig. 7.23 shows the development of sample profiles in the main heating path, corresponding to the nearly equilibrated states at the end of every 10°C temperature step. The increasing compressive lateral strains associated with increasing temperatures can readily be observed, where a relative uniform pattern is recorded with no differences between mid-height and average values.

Fig. 7.24 shows time evolution of axial, radial, volumetric and shear strains, as well as water volume changes at a reference temperature of 22°C (negative values denote water outlet), that undergoes the normally consolidated soil sample upon applying a temperature change starting from 22°C to 30°C (first step of path B-C in Fig. 7.19 and Fig. 4.12). The first phase up to 100 min corresponds to the quasi-undrained stage where water drainage is not allowed and then temperature is held constant for the remainder of the pore pressure equalisation period (drained stage after thermal equilibrium). Drained thermal consolidation phase with some water outlet and where no appreciable distortion of the sample is observed, is interrupted after 7 days testing, corresponding to a relatively stable volumetric steady state (a volumetric strain rate lower than 0.02%/day).

Fig. 7.25 to Fig. 7.27 show equivalent plots for temperature increments corresponding to the same main heating path B-C from 30°C to 40°C, from 40°C to 50°C and from 50°C and 60°C, respectively, where clear isotropic responses following the general trend previously outlined are observed (dilative quasi-undrained phases and compactive drained phases). As temperature increases, some spurious phenomena start to affect the control of the equalisation stages, such as free water evaporation through the air pressure line (refer to section 4.5.2) and the accumulation of dissolved air beneath the ceramic discs (refer to section 3.2.5). Evaporative and diffused air fluxes are indicated in the different plots (water volume change : elapsed time diagram), where increasing diffused air fluxes and starting to develop at lower elapsed times are detected at higher temperatures. Typical diffused air fluxes are indicated in Fig. 3.19, where values higher than $2{\times}10^{-6}$ (mm^3/s)/mm^2 are usually associated with the uncontrolled and progressive cavitation of the system and the consequent loss of continuity between the pore water and the water in the measuring system. In Fig. 7.27, soil shrinkage due to soil water evaporation and consequent suction increase is detected at elapsed times higher than 2000 min caused by diffused air accumulation (refer to the dashed lines in water volume change plot and diffused air fluxes indicated in the figure), which can be confused with the same volume change response associated with thermal contraction. This stage was interrupted when the uncontrolled and isotropic shrinkage was detected, reducing the temperature immediately to 40°C, after flushing the diffused air accumulated beneath the discs (refer to Fig. 7.28).

Fig. 7.28 and Fig. 7.29 represent time evolution of strains and water volume changes in main cooling steps corresponding to path C-D in Fig. 7.19 and Fig. 4.12. When temperature is lowered a decrement in pore water pressure develops (matric suction or intergranular stress increase) due to its greater volumetric expansion coefficient, which results at early-undrained stages of the test in an isotropic compactive phenomenon. This analogous to shrinkage associated with matric suction increase or compression due to intergranular stress increase phenomenon is expected to occur without appreciable yielding, where the main q : p yield surface grows with the decrease in temperature and the transient stress state remains in the elastic zone. The rate of cooling in the first stage is -20°C/hour and the regulation phase is maintained for 5 days, where a low drained thermal expansive trend with some water inlet is detected and further hindered by some shrinkage at elapsed times higher than 2000 min. Air diffusion fluxes are still high, but they develop at higher elapsed times. The following cooling stage down to ambient temperature (the cooling circuit indicated in Fig. 3.33 is used at temperatures lower than 25°C) allows the recovery of the appropriate air diffusion flux levels to start another heating stage. In this case, a clear isotropic drained thermal expansion associated with water inlet is detected in the equalisation phase that does not surpass the initial quasi-undrained contraction (a dominating contraction upon drained cooling process).

Fig. 7.30 and Fig. 7.31 represent time evolution of strains and water volume changes in scanning heating steps corresponding to path D-E in Fig. 7.19 and Fig. 4.12. In the first step and after the isotropic dilative quasi-undrained phase, a low isotropic drained thermal contraction phenomenon and associated with water outlet is detected that is further altered by the uncontrolled shrinkage due to the accumulation of diffused air that affects water availability at elapsed times higher than 2000 min. After flushing the drainage lines, it was decided to continue with another heating step (refer to Fig. 7.31), which was interrupted after 1 day due to uncontrolled air diffusion at elapsed times higher than 500 min.

Fig. 7.32 to Fig. 7.35 represent time evolution of strains and water volume changes in the different cooling steps corresponding to path E-F in Fig. 7.19 and Fig. 4.12. When temperature is lowered an isotropic compression is observed at early undrained stages, followed by some drained expansion associated with water inlet that is further affected by spurious shrinkage at high temperatures (accumulation of diffused air at elapsed times higher than 1000 min for the regulation phases at 50°C and 40°C). The rate of cooling in the first stage is -40°C/hour and the regulation phase is maintained for 2 days. Lower cooling rates are followed as temperature is decreased (-10°C/min for the temperature step 40°C→30°C). Fig. 7.34 shows a clear isotropic drained cooling expansion associated with water inlet that compensates the initial quasi-undrained contraction.

Afterwards, the specimen was isothermally unloaded at 22°C up to $(\sigma_m-u_a) = 0.10$ MPa and under the same matric suction (path F-G in Fig. 7.19 and in Fig. 4.12). A strict stabilisation period controlling diffused air fluxes was followed before starting the next heating-cooling cycle under a slightly overconsolidated state, represented by path G-H-I in Fig. 7.19 and Fig. 4.12. The temperature range is limited in this case to 50°C in order to minimise consequences on loss of continuity in the liquid water source detected in the first heating paths. Fig. 7.36 to Fig. 7.38 show time evolutions of strains and water volume changes that undergoes the overconsolidated sample upon applying a temperature change from 22°C to 50°C under constant suction and isotropic net mean stress conditions (path G-H in Fig. 7.19 and in Fig. 4.12). As observed in Fig. 7.36 and Fig. 7.37, similar trends of behaviour can be detected with respect to the transition between the dilative quasi-undrained stage and the regulation phase, where some isotropic contraction associated with water outlet is detected. However, lower dilative strains in the quasi-undrained stage are observed compared to those obtained in the main heating path followed on the normally consolidated sample (refer to Fig. 7.40). In addition, lower drained compression strains are observed in the regulation phase that do not compensate the initial dilative phenomenon, resulting in an overall expansion of soil skeleton, which is the major difference concerning normal and overconsolidated states. No clear trend is observed with respect to the small water volume changes detected upon heating, although certain water volume outlet seems to be

registered that tends to diminish at higher temperatures. Diffused air accumulation problems were detected in the last heating step, which induced uncontrolled shrinkage at elapsed times higher than 1500 min. Fig. 7.39 represents time evolution of strains and water volume changes in a cooling step performed on the overconsolidated sample corresponding to path H-I in Fig. 7.19 and Fig. 4.12, where some drained expansion is detected following the dominant isotropic contraction of the quasi-undrained cooling stage.

Total heating-cooling programme lasted for 21 weeks (refer to Table 4.3), at the end of which some signal degradation was registered with certain increase in the electrical noise, mainly concerning internal LVDTs. For this reason, time evolutions of the remaining cooling steps of path H-I in Fig. 7.19 were not represented.

7.2.1.2   *Pore pressure generation under quasi-undrained conditions*

The increase of pore water pressure upon heating under nearly saturated conditions with no change in boundary confining stress and air pressure ($\delta\sigma_m = 0$ and $\delta u_a = 0$) can be analysed assuming volumetric compatibility between soil matrix (indicated with subscript m) and its constituents (air, liquid and solid, indicated with subscripts a, l and s, respectively) and taking into account of both thermal expansion and compressibility coefficients (negative and positive values are considered respectively in consistency with positive compression strains). Following Agar *et al.* (1986), Vaziri (1988), Srithar and Byrne (1990), Vaziri and Byrne (1990) and Mitchell (1993), where the overall volume change is a function of temperature change δT, as well as pore fluid pressure change δu_w and the change in intergranular stress $\delta\hat{p}$, the following expressions are obtained for the volume change of each component and soil matrix in terms of their bulk moduli B_i and volumetric thermal-expansion coefficients α_i:

$$\delta V_i = -\left(\frac{\delta u_w}{B_i} + \alpha_i \delta T\right)V_i \quad \text{for} \quad i = a, l; \quad \delta V_s = -\left(\frac{\delta u_w}{B_s} + \alpha_s \delta T\right)V_s - \frac{\delta\hat{p}}{B_s'}V_m \quad \text{and}$$

$$\delta V_m = -\left(\frac{\delta u_w}{B_s} + \alpha_s \delta T + \frac{\delta\hat{p}}{B_m} + \alpha_m \delta T\right)V_m \quad \text{with} \quad V_l = n\,Sr\,V_m, \quad V_a = n(1 - Sr)V_m, \quad (7.5)$$

$$V_s = (1 - n)V_m$$

The last term of δV_s expression refers to the compressibility of solids under concentrated interparticle contacts due to a change in intergranular stress, assuming an equivalent compressibility B_s' similar to that under isotropic pressure B_s. The first two terms of δV_m expression assume soil mass with all grains in contact, as well as the same thermal-expansion coefficient and compressibility of soil grains (soil mass and soil grains undergo the same volumetric strain). The last two terms of δV_m expression refer to the compressibility and the thermal expansion coefficient of soil structure under drained conditions, associated with particle reorientation to permit soil structure to carry the same intergranular stress under a temperature change or to carry a different intergranular stress under a constant temperature.

After rearrangement of the terms, the following expressions for the excess pore water pressure are obtained under undrained conditions with no change in boundary stresses, corresponding to an intergranular stress change under nearly saturated conditions of $\delta\hat{p} = -\delta u_w$:

$$\delta u_w = -\frac{[n(1-Sr)\alpha_a + nSr\alpha_1 - n\alpha_s - \alpha_m]\delta T}{\dfrac{n(1-Sr)}{B_a} + \dfrac{nSr}{B_1} - \dfrac{(1+n)}{B_s} + \dfrac{1}{B_m}}$$

$$\delta u_w \approx -\frac{[n(Sr\,\alpha_f - \alpha_s - \alpha_m/n)]\delta T}{\dfrac{nSr}{B_f} + \dfrac{1}{B_m}} \quad \text{for} \quad Sr \rightarrow 1, \quad \frac{(1+n)}{B_s} \ll \frac{nSr}{B_f} \quad \text{and} \quad \frac{(1+n)}{B_s} \ll \frac{1}{B_m} \tag{7.6}$$

where the second expression is valid for nearly saturated states, assuming a homogenised compressible fluid with a pore fluid bulk-modulus B_f and thermal coefficient α_f, and assuming a solid particles bulk modulus $B_s \gg B_f$ and $B_s \gg B_m$ (usually around $B_s \approx 50$ GPa).

The pore-fluid (air-liquid mixture) bulk modulus can be estimated by means of the expression indicated in section 4.4.3.2 and proposed by Ghaboussi and Kim (1982) that takes into account the compressibility of the air portion due to free air compression and air dissolving into water. For $Sr_o \approx 94.3\%$ and an absolute pressure $u_a = 0.60$ MPa: $1/B_f \approx 0.12$ MPa^{-1}. The drained modulus of soil matrix can be estimated from drained constrained values presented in Fig. 2.35 ($E_k' \approx 40$ MPa) and assuming a Poisson's ratio of $\nu \approx 0.2$ (refer to section 2.3.1.2): $B_m = (1+\nu)E_k'/[3(1-\nu)] \approx 20\,\text{MPa}$. According to quasi-undrained main heating data presented in Fig. 7.40, the homogenised thermal coefficient is $\alpha_f \approx -[3.5+0.075(T-22)]\times 10^{-4}$ °C^{-1} admitting an initial porosity $n_o \approx 0.404$, $Sr_o \approx 94.3\%$ and a thermal coefficient of solids $\alpha_s \approx -2.9\times 10^{-5}$ °C^{-1} (refer to section 6.2.1.3). Values of coefficient of thermal expansion for soil structure upon main heating are obtained from Fig. 7.41: $\alpha_m \approx [3.8-0.058(T-22)]\times 10^{-4}$ °C^{-1} for a compressive plastic process, and around $\alpha_m \approx -[0.44+0.022(T-22)]\times 10^{-4}$ °C^{-1} for a dilative elastic process. At the beginning of the heating path the stress point is in contact with the yield surface, which undergoes shrinking upon heating as further discussed. However, the plastic strain hardening is a gradual process that develops with time as pore pressures dissipate, which can be seen as a heat induced consolidation/creep phenomenon at constant total stress. As a consequence, the quasi-undrained stage is not an entirely plastic process, but it will be considered as such to evidence the most unfavourable condition of pore pressure generation. Indeed, the macropore space increase generated in an elastic process upon heating allows accommodating pore water expansion without an excessive pore water pressure build-up, while a plastic contraction upon heating induces an opposite effect generating a higher pore pressure change. Typical temperature-induced pore pressure changes under quasi-undrained conditions and under constant boundary stress state $((\sigma_m-u_a) = 1.00$ MPa and $(u_a-u_w) = 0.20$ MPa) are the following ones for the different heating stages:

$$22\,^{\circ}\text{C} \rightarrow 30\,^{\circ}\text{C}; \quad \delta u_w/\delta T \approx 0.0052\,\text{MPa}\,^{\circ}\text{C}^{-1}; \quad \hat{p}^{-1}\delta u_w/\delta T \approx 0.0043\,^{\circ}\text{C}^{-1}; \quad \delta u_w \approx 42\,\text{kPa}$$

$$30\,^{\circ}\text{C} \rightarrow 40\,^{\circ}\text{C}; \quad \delta u_w/\delta T \approx 0.0049\,\text{MPa}\,^{\circ}\text{C}^{-1}; \quad \hat{p}^{-1}\delta u_w/\delta T \approx 0.0041\,^{\circ}\text{C}^{-1}; \quad \delta u_w \approx 49\,\text{kPa}$$

$$40\,^{\circ}\text{C} \rightarrow 50\,^{\circ}\text{C}; \quad \delta u_w/\delta T \approx 0.0047\,\text{MPa}\,^{\circ}\text{C}^{-1}; \quad \hat{p}^{-1}\delta u_w/\delta T \approx 0.0039\,^{\circ}\text{C}^{-1}; \quad \delta u_w \approx 47\,\text{kPa}$$

$$50\,^{\circ}\text{C} \rightarrow 60\,^{\circ}\text{C}; \quad \delta u_w/\delta T \approx 0.0044\,\text{MPa}\,^{\circ}\text{C}^{-1}; \quad \hat{p}^{-1}\delta u_w/\delta T \approx 0.0037\,^{\circ}\text{C}^{-1}; \quad \delta u_w \approx 44\,\text{kPa}$$

$$\tag{7.7}$$

As observed, the estimated water pressure build-up stays below matric suction value in such a way that no water overpressure is generated. Typical values of $\hat{p}^{-1}\delta u_w/\delta T$ are between 0.013 °C^{-1} and 0.018 °C^{-1} for saturated clays in the temperature range between 20°C and 40°C (Mitchell, 1993). Hueckel and Pellegrini (1989, 1991) suggested a thermo-plastic-hydraulic model, including both non-linear pore water expansion and thermoplastic compressive strain in skeleton, to interpret pore pressure generation and thermal failure of saturated Boom clay in response to heating at constant total stress under undrained conditions.

7.2.2 Thermo-mechanical behaviour under quasi-undrained conditions

Thermo-mechanical behaviour under quasi-undrained conditions with no change in boundary confining stresses can be taken into account by mass conservation equations, for which there is no relative displacement of the homogenised compressible fluid with respect to solid skeleton and considering an overall coefficient of thermal expansion for soil constituents. For a compressible fluid the volume constraint equation can be expressed as:

$$\frac{1}{V}(\dot{V}_a + \dot{V}_l) = -\dot{\varepsilon}_v - \frac{1}{V}\dot{V}_s \quad \text{with } \dot{V}_a, \dot{V}_l \text{ and } \dot{V}_s \text{ from Eq. (7.5)}, \dot{p} = -\dot{u}_w \text{ and } B_s' = B_s$$

$$\dot{\varepsilon}_v - \frac{\dot{u}_w}{B_{eq}} - \alpha_{eq}\dot{T} = 0; \quad \text{with} \quad B_{eq} = \frac{n(1-Sr)}{B_a} + \frac{n\,Sr}{B_l} - \frac{n}{B_s} \quad \text{or} \quad B_{eq} \approx \frac{n\,Sr}{B_f} \quad \text{for} \quad Sr \to 1 \quad (7.8)$$

$$\alpha_{eq} = n(1-Sr)\alpha_a + n\,Sr\,\alpha_l + (1-n)\alpha_s \quad \text{or} \quad \alpha_{eq} \approx n\,Sr\,\alpha_f \quad \text{for} \quad Sr \to 1$$

where B_{eq} and α_{eq} are the equivalent bulk modulus and thermal expansion coefficient of the constituents and superscript dot denotes partial differentiation with respect to time. Approximations hold for nearly saturated states and assuming a homogenised compressible phase, where $B_s \gg B_f$ and $\alpha_s \ll \alpha_f$ (usually over one order of magnitude).

For simplicity, in what follows the compressibility of the homogenised phase is neglected and volumetric strain in the quasi-undrained stage is assumed to be solely governed by thermal induced strains. This approach, although not exact, is sufficiently appropriate to describe certain phenomena induced by temperature changes. As observed in Fig. 7.40, the thermal expansion coefficient detected upon main heating at $(\sigma_m\text{-}u_a) = 1.00$ MPa and $(u_a\text{-}u_w) = 0.20$ MPa is somewhat higher (in absolute value) than the free water prediction at $e_o \approx 0.679$ and $Sr_o \approx 94.3\%$ and somewhat lower if entrapped air dilatation $(1\text{-}Sr_o)$ is considered assuming ideal gas law at constant air pressure ($\alpha_a|_{u_a} = -1/T$, with T the absolute temperature). Fig. 7.40 also represents the thermal dilatation of the homogenised fluid α_f that fits the experimental results of this main heating path, admitting non negligible thermal coefficient of solids of $\alpha_s \approx -2.9\times10^{-5}$ °C^{-1}. Undrained thermal expansion values of saturated Boom clay under a similar void ratio ($e \approx 0.654$) and obtained by Horseman *et al.* (1987) are also presented for comparison. A striking aspect is the drastic reduction (in absolute value) of the thermal dilatation coefficient upon main cooling, which cannot only be associated with porosity variation (down to $e \approx 0.651$). It appears that dissolved air, which accounts for an important component in thermal dilatation, could be released by nucleation or coalescence of bubbles from soil water with increasing temperatures. In addition, some part of water in soil is held by very high electro-chemical forces to the mineral surfaces, affecting its thermal expansion coefficient. On the basis of a microscopic model with parallel mineral platelets, Baldi *et al.* (1988) found that thermal expansion of low-porosity clay water is dependent on temperature, on inter-particle spacing and on effective stress, displaying lower values than under free water conditions.

Quasi-undrained main cooling and scanning heating paths at $e \approx 0.651$ and $Sr_o \approx 94.3\%$ have been fitted to the following expressions, assuming an inter-aggregate water content of $w_{ad} \approx 13\%$ (refer to section 5.1.1 and assuming no significant intra-aggregate water release upon main heating), solid thermal expansion $(1\text{-}n)\alpha_s$, no significant entrapped air content, and a dissolved air thermal expansion of $n\,h\,Sr\,\alpha_a$ (a volumetric solubility in water of $h \approx 0.017$ can be considered for the test temperature range according to Fig. 3.20):

$$\alpha_f = \left(1 - \frac{Sr_{ad}}{Sr}\right)\alpha_{lf} + \frac{Sr_{ad}}{Sr}\alpha_{lad} + h\,\alpha_a \approx -[150 + 4.5(T-22)]\times10^{-6} \text{ °C}^{-1} \quad (7.9)$$

where $n(Sr - Sr_{ad})\alpha_{lf}$ stands for thermal expansion of free water and $n\,Sr_{ad}\alpha_{lad}$ for adsorbed water at an estimated degree of saturation of $Sr_{ad} = w_{ad}Gs/e \approx 54\%$. This fitted expression presents somewhat lower values (in absolute values) compared to the semi-empirical formula for thermoelastic expansion of interstitial water in low porosity clays proposed by Baldi *et al.* (1988).

If free water at atmospheric pressure expands according to $\alpha_{lf} = -[230 + 7.9(T - 22)] \times 10^{-6}$ °C^{-1} and dissolved air is assumed as an ideal gas at constant air pressure $\alpha_a\big|_{u_a} = -1/(T + 273.15) \approx$ $-[3390 - 10.5(T - 22)] \times 10^{-6}$ °C^{-1} (the approximation holds for test temperature range):

$$\begin{aligned}
\alpha_{lad} &\approx -[84 + 1.9(T - 22)] \times 10^{-6} \text{ °C}^{-1} \quad \text{considering} \quad h = 0 \quad \text{(no dissolved air)} \quad \text{and} \\
\alpha_{lad} &\approx -[16 + 2.2(T - 22)] \times 10^{-6} \text{ °C}^{-1} \quad \text{considering} \quad h = 0.017
\end{aligned}$$
$$(7.10)$$

where values of the same order of magnitude of solid thermal expansion coefficient are obtained.

Based on Eq.(7.9) and assuming an entrapped air volume of $n(1\text{-}Sr)$ and a solid thermal expansion $(1 - n)\alpha_s$, the thermal expansion coefficient of the main heating path is predicted and represented in Fig. 7.40, showing quite good agreement with respect to the thermal homogenised fluid interpolation: $\alpha_f \approx -[350 + 7.5(T - 22)] \times 10^{-6}$ °C^{-1}.

7.2.3   Thermo-mechanical behaviour under drained conditions

Fig. 7.41 represents the development of volumetric strains at different temperatures in drained paths, after dissipation of thermally induced pore water pressures and after a relatively stable volumetric steady state is reached. The existence of important plastic compressive strains associated with the main heating path on the normally consolidated state is a relevant feature of the data. Main heating effects affecting rearrangement of the macrostructure of clay skeleton are not erased by the following stage of main cooling and scanning heating paths, which present a quasi-elastic behaviour. On the other hand, overconsolidated state exhibits a quasi-reversible volume expansion during drained heating.

During drained heating two different phenomena take place. Firstly, a quasi-reversible phenomenon due to the expansion of the mineralogical components and adsorbed water of the aggregates and certain particle rearrangement, since expanding bulk water is free to leave the clay mass. This drained thermal expansion varies with temperature as further discussed and with stress state as observed in Fig. 6.25 or in a more generalised way with the actual overconsolidation ratio to introduce certain dependence on hardening parameters under a coupled elastoplasticity concept. This reversible volumetric thermal strain is given in incremental form according to Eq. (6.12), where the following parameters are obtained for test conditions prevailing at constant intergranular stress state $\hat{p}$ (refer to Fig. 7.41):

$$\frac{\delta\varepsilon_v^e}{\delta T}\bigg|_{\hat{p}} = \alpha(\Delta T, \hat{p}) = \alpha_m + \alpha_o(\hat{p}) + \alpha_1(\hat{p})\Delta T \quad \text{with} \quad \alpha_i(\hat{p}) = \alpha_i^a + \alpha_i^b \ln\frac{\hat{p}}{\hat{p}_r}$$

$$\alpha_m + \alpha_o(\hat{p} \approx 1.2 \text{ MPa}) \approx -(3.8 \pm 2.0) \times 10^{-5} \text{ °C}^{-1} \quad \text{and} \tag{7.11}$$

$$\alpha_m + \alpha_o(\hat{p} \approx 0.3 \text{ MPa}) \approx -(5.0 \pm 2.0) \times 10^{-5} \text{ °C}^{-1} \quad \text{with} \quad \alpha_o^b \approx 8.6 \times 10^{-6} \text{ °C}^{-1}$$

$$\alpha_1(\hat{p} \approx 1.2 \text{ MPa}) \approx -2.1 \times 10^{-6} \text{ °C}^{-2} \,; \quad \alpha_1(\hat{p} \approx 0.3 \text{ MPa}) \approx -2.3 \times 10^{-6} \text{ °C}^{-2}$$

and ΔT stands for the temperature difference with respect to a reference state at 22°C. Drained thermal expansion coefficient $\alpha(\Delta T, \hat{p})$ includes that of the clay solid mineral α_m, which is assumed not to depend on stress level (refer to section 7.2.1.2), and that of the porous skeleton ($\alpha - \alpha_m$), dependent on stress state (or overconsolidation ratio) and temperature. Nevertheless, when comparing with oedometer test results described in section 6.2.1.3 based on isothermal data that present higher volumetric strain accuracy, these drained reversible thermal coefficients are somewhat higher then the corresponding ones at approximated stress states reported by Eq. (6.13). However, isotropic thermal expansion values show an adequate tendency within the accuracy of the experimental setup, which allow detecting the temperature and stress state influence.

The second effect is an irreversible meta-stable compressive phenomenon that results in the failure of inter-aggregate contacts and induces a rearrangement of the structure of soil skeleton. This compactive phenomenon, in accordance with collapsible effects, appears to be more pronounced in normally consolidated states and medium or high-porosity packings with well-defined inter-aggregate voids. From an elastoplastic point of view, collapsible strains upon matric suction decrease are associated with a reduction of the elastic domain introducing a dependence on the decrease of apparent cohesion and preconsolidation stress with suction (Alonso *et al.*, 1990). In addition, irreversible thermal strains in skeleton as resulting from drained tests can also be described by employing concepts of thermoplasticity theory (Boley and Weiner, 1960) and an adaptation of modified Cam-clay model (Atkinson and Bransby, 1978; Wood, 1990) to thermal loading (Hueckel and Borsetto, 1990; Hueckel and Baldi, 1990; Seneviratne *et al.*, 1993; Gens, 1995). This way, the irreversible thermal mechanism on clay skeleton has been taken into account by introducing the dependence of yield surface $f(p, s, q, p_c^*) = 0$ with temperature through its dependence on the preconsolidation stress $p_o(s, p_c^*(\varepsilon_v^p, \Delta T))$ and the apparent cohesion $p_s(s, \Delta T)$, following the proposal of Gens (1995) (refer to Fig. 7.42). The skeleton response to stress states within the main q : p yield surface is thermoelastic, and the response to changes of stress states at the yield surface is thermoplastic. The yield surface in non-thermal conditions is a function of plastic volumetric strain ε_v^p and suction, and expands (strain hardening) with compactive plastic volumetric strains. In thermal conditions, the thermoelastic domain shrinks with an increasing temperature (thermal softening) and it is assumed to expand when cooling occurs (refer to Fig. 7.42).

Main drained heating at constant isotropic stress state as imposed in the tests for the normally consolidated state is admitted to be an isotropic plastic process, with the thermal softening due to the increase in temperature being compensated for by the volumetric strain hardening. On the other hand, drained cooling at constant isotropic stress state is assumed a reversible isotropic process, where temperature appears as a state variable inducing elastic volumetric strains and as an internal variable modifying the yield surface. Loading-unloading criteria dependent on stress rates and temperature rates are described in Hueckel and Borsetto (1990) and Gens (1995). Loading-collapse yield locus (LC in Fig. 7.42) for an isotropic compression at fixed suction $p_o(s, p_c^*(\varepsilon_v^p, \Delta T))$ is given as (Alonso *et al.*, 1990): $\left(p_o / p^c\right) = \left(p_c^* / p^c\right)^{(\lambda(0) - \kappa)/(\lambda(s) - \kappa)}$, where p^c is a reference stress and the post-yield compressibility parameter as a function of suction $\lambda(s)$ is given in a general form by Eq. (6.24). For simplicity it is assumed that both the compressibility parameter in the post-yield range $\lambda(s)$ as well as the compressibility parameter in the pre-yield range κ are not largely affected by temperature. However, some temperature dependence on these parameters has been detected as indicated in Fig. 6.57 and Fig. 6.67. Typical values of these parameters under isothermal conditions are indicated in Fig. 7.19: $\lambda(s = 0.20\text{MPa}) \approx 0.057$ and $\kappa \approx 0.005$.

The dependence on maximum saturated isotropic stress $p_c^*(\varepsilon_v^p, \Delta T) = p_o^*(\varepsilon_v^p) + A(\Delta T)$ is modelled assuming an uncoupled thermal softening and strain hardening (no thermal ductilisation) through a

thermal softening function $A(\Delta T) = a_1 \Delta T + a_2 \Delta T^2$ (Hueckel and Borsetto, 1990; Hueckel and Baldi, 1990), where a_1 and a_2 are coefficients of thermal sensibility of the yield surface. The form of this expression has been chosen in a way to keep separate the thermal and plastic strain dependence of the yield surface. A second temperature ductilisation effect, as described by Gera *et al*. (1996) and Hueckel *et al*. (1998), takes into account the amount of strain hardening at different temperatures. However, these phenomena may be jointly viewed as a consequence of thermal softening and globally described by an exponential expression as suggested by Picard (1994) and Gera *et al*. (1996). $p_o^*(\varepsilon_v^p)$ is the usual Cam-clay hardening parameter that depends only on plastic volumetric strains according to $\delta p_o^* = \left((1 + e_o) p_o^* / (\lambda(0) - \kappa) \right) \delta \varepsilon_v^p$ (Alonso *et al*., 1990). The consistency condition for an temperature increment δT at constant stress state, $\delta p = 0$, $\delta s = 0$ and $\delta q = 0$ at yielding, implies that:

$$\frac{\partial f}{\partial T} \delta T + \frac{\partial f}{\partial \varepsilon_v^p} \delta \varepsilon_v^p = 0 \; ; \quad \frac{\delta \varepsilon_v^p}{\delta T} = \frac{-\left[\dfrac{\partial f}{\partial p_s} \dfrac{\partial p_s}{\partial T} + \dfrac{\partial f}{\partial p_o} \dfrac{\partial p_o}{\partial p_c^*} \dfrac{\partial p_c^*}{\partial T} \right]}{\dfrac{\partial f}{\partial p_o} \dfrac{\partial p_o}{\partial p_c^*} \dfrac{\partial p_c^*}{\partial \varepsilon_v^p}} \tag{7.12}$$

Assuming no thermal dependence of apparent cohesion ($\partial p_s / \partial T = 0$), the above expression transforms to:

$$\frac{\delta \varepsilon_v^p}{\delta T} = \frac{-\partial p_c^* / \partial T}{\partial p_c^* / \partial \varepsilon_v^p} = \frac{-(\lambda(0) - \kappa)(a_1 + 2a_2 \Delta T)}{(1 + e_o) p_o^*} \tag{7.13}$$

Linear interpolation has been adopted to fit $\delta \varepsilon_v^p / \delta T$ data, which is shown in Fig. 7.41. Due to the fact that the soil remains in a nearly saturated state, without having been exceeded the air-entry value of the packing estimated in an air overpressure between 0.3 MPa and 0.6 MPa, the saturated post-yield compressibility parameter remains close to the value indicated in Fig. 7.19: $\lambda(0) \approx 0.057$. For soil conditions prevailing at the beginning of the main heating path ($e_o \approx 0.679$, $T_r = 22°C$ and $p_o^* \approx 1.0$ MPa for a nearly saturated condition), coefficients of thermal sensibility of the yield surface are: $a_1 \approx -1.5 \times 10^{-2}$ MPa.°C^{-1} and $a_2 \approx 6.3 \times 10^{-5}$ MPa.°C^{-2}, remaining the thermal softening function always negative.

Fig. 7.43 presents this thermal softening function $A(\Delta T)$ compared to measured values of preconsolidation pressure change of saturated Boom clay ($e \approx 0.48$) at different temperatures reported by Sultan *et al*. (1998), where an adequate agreement is observed between both results at least up to 50°C. The stress value at which yield occurs decreasing with temperature based on data reported by Sultan *et al*. (1998) up to 100°C have been fitted to an equivalent thermal softening function, where the following parameters are obtained: $a_1 \approx -1.3 \times 10^{-2}$ MPa.°C^{-1} and $a_2 \approx -1.2 \times 10^{-4}$ MPa.°C^{-2}. Two sets of coefficients of thermal sensibility of the yield surface, accounting for different elastic domains at a given temperature, for saturated Boom clay at $e \approx 0.50$ reported by Pellegrini and Trentesaux (1998) have been adapted and represented in Fig. 7.43, displaying the following material parameters: $a_1 \approx -8.6 \times 10^{-2}$ MPa.°C^{-1} and $a_2 \approx 2.2 \times 10^{-4}$ MPa.°C^{-2} for the first set; and $a_1 \approx -1.8 \times 10^{-2}$ MPa.°C^{-1} and $a_2 \approx -9.5 \times 10^{-5}$ MPa.°C^{-2} for the second set (see also Hueckel and Pellegrini, 1991), the latter presenting a better agreement with test results reported by Sultan *et al*. (1998) and in the present study. Thermal softening aspects in normally consolidated states and at different degrees of saturation have been detected in the static compaction tests performed at different temperatures under oedometer conditions and reported in section 2.3.1. However, further research work is required to extend thermal softening aspects in normally consolidated and isotropic stress states under constant water content

conditions (closed system to vapour) covering the 'intra' and 'inter-aggregate governing suction' zones. In addition, the influence of the deviatoric stress on thermal softening has not been systematically studied to date, as most available data are obtained from isotropic tests.
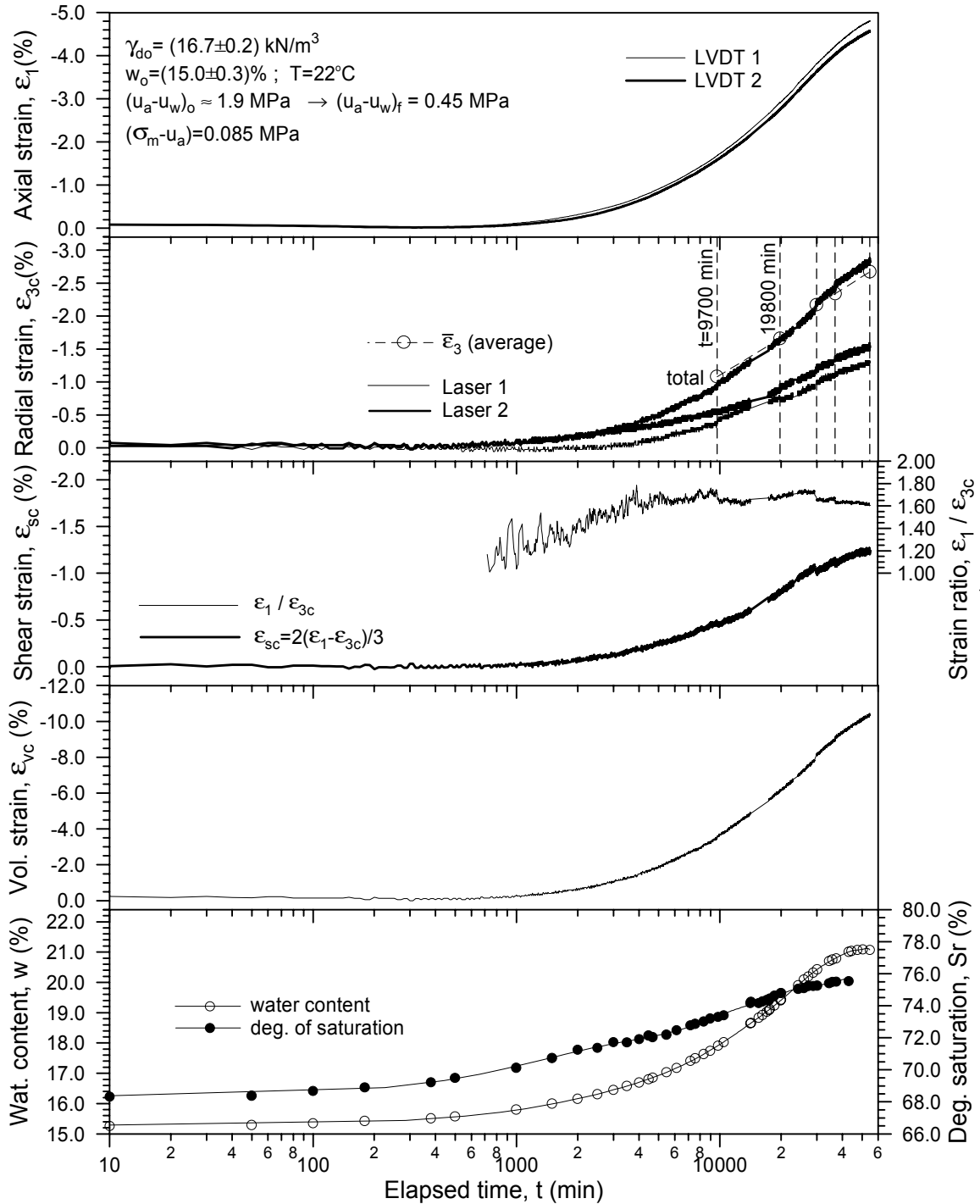
Figure 7.1   Time evolution of axial, radial, shear and volumetric strains, water content and degree of saturation for the high-density packing in a main wetting path ($s_o \approx 1.9$ MPa $\rightarrow s_f = 0.45$ MPa).
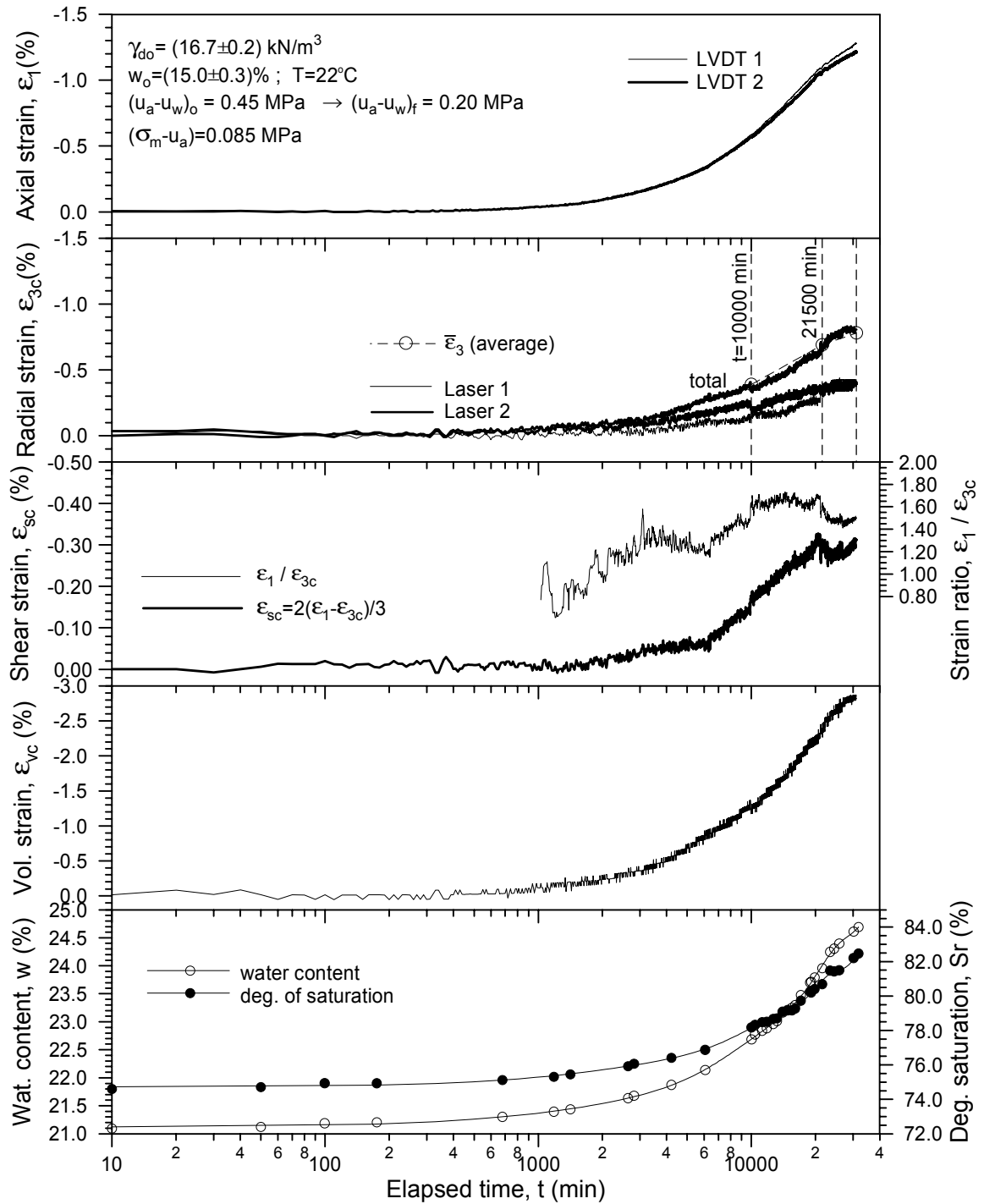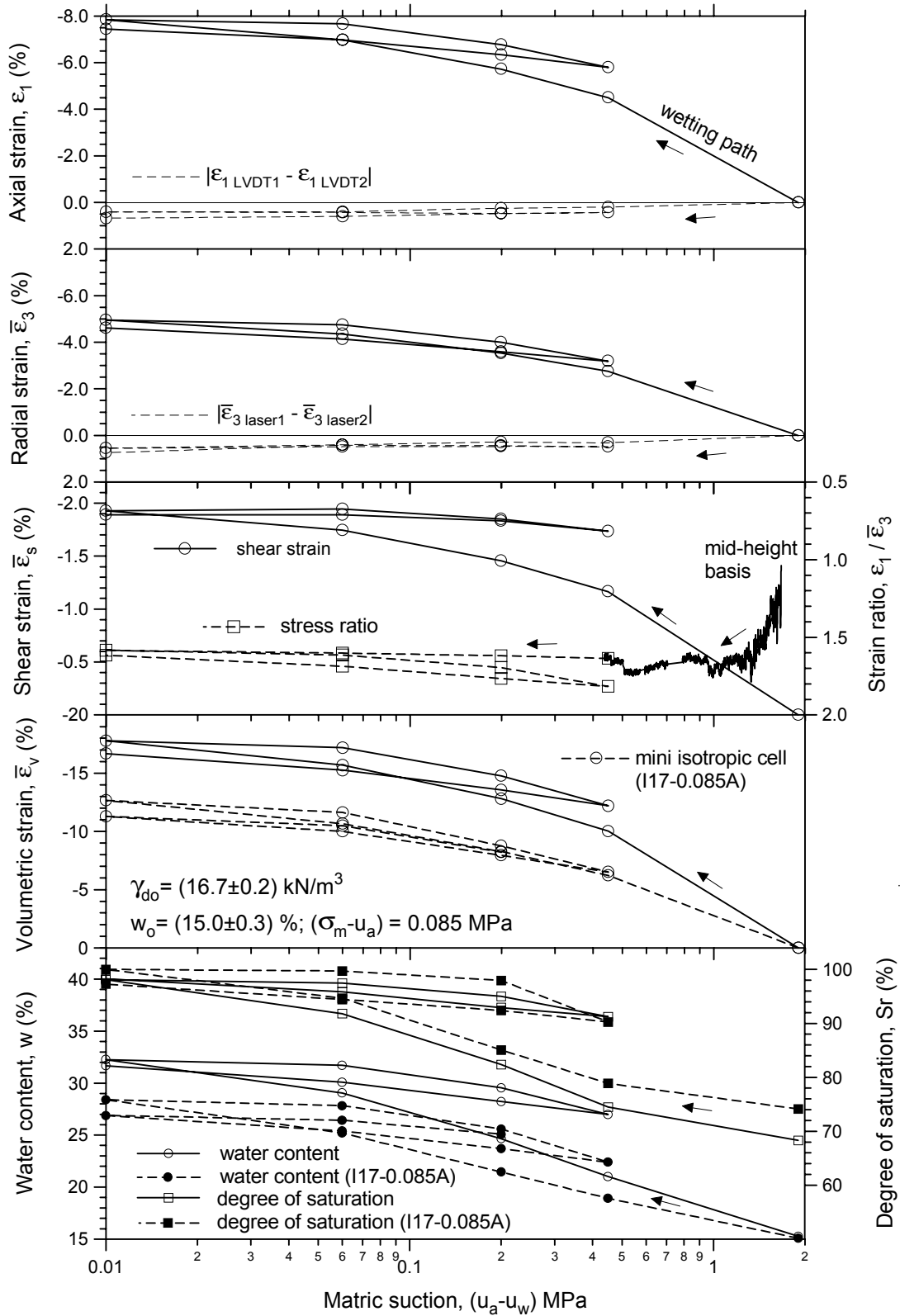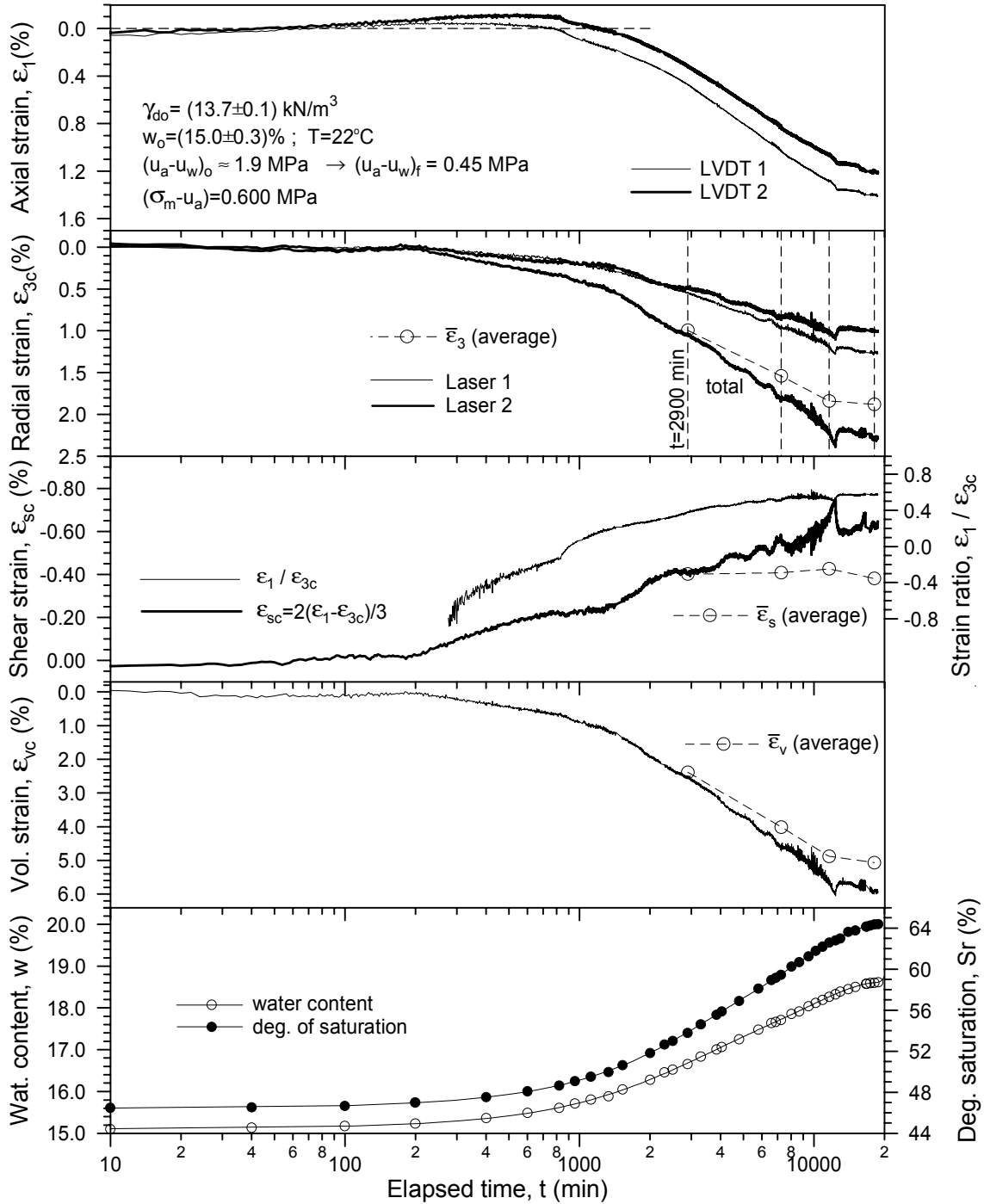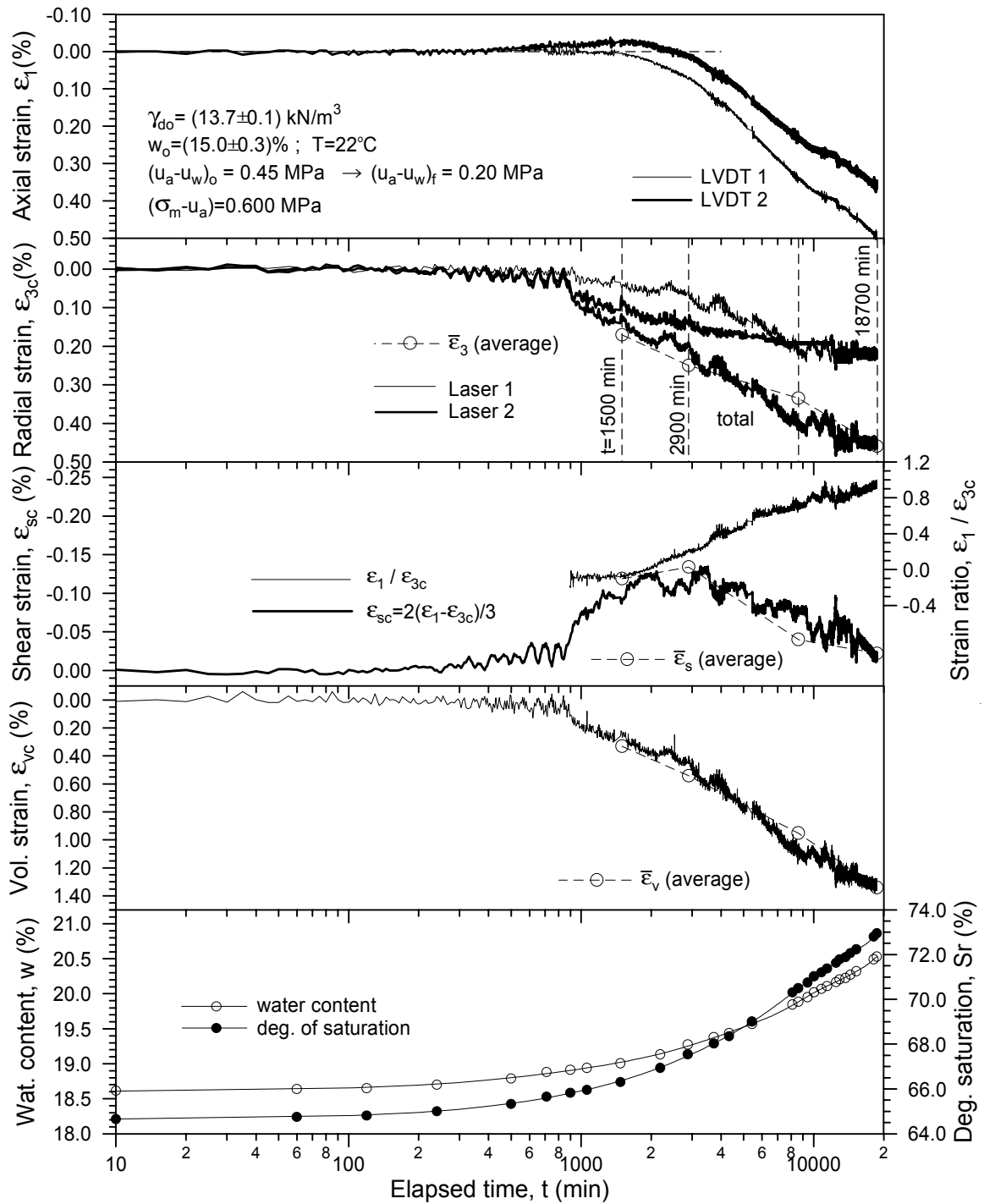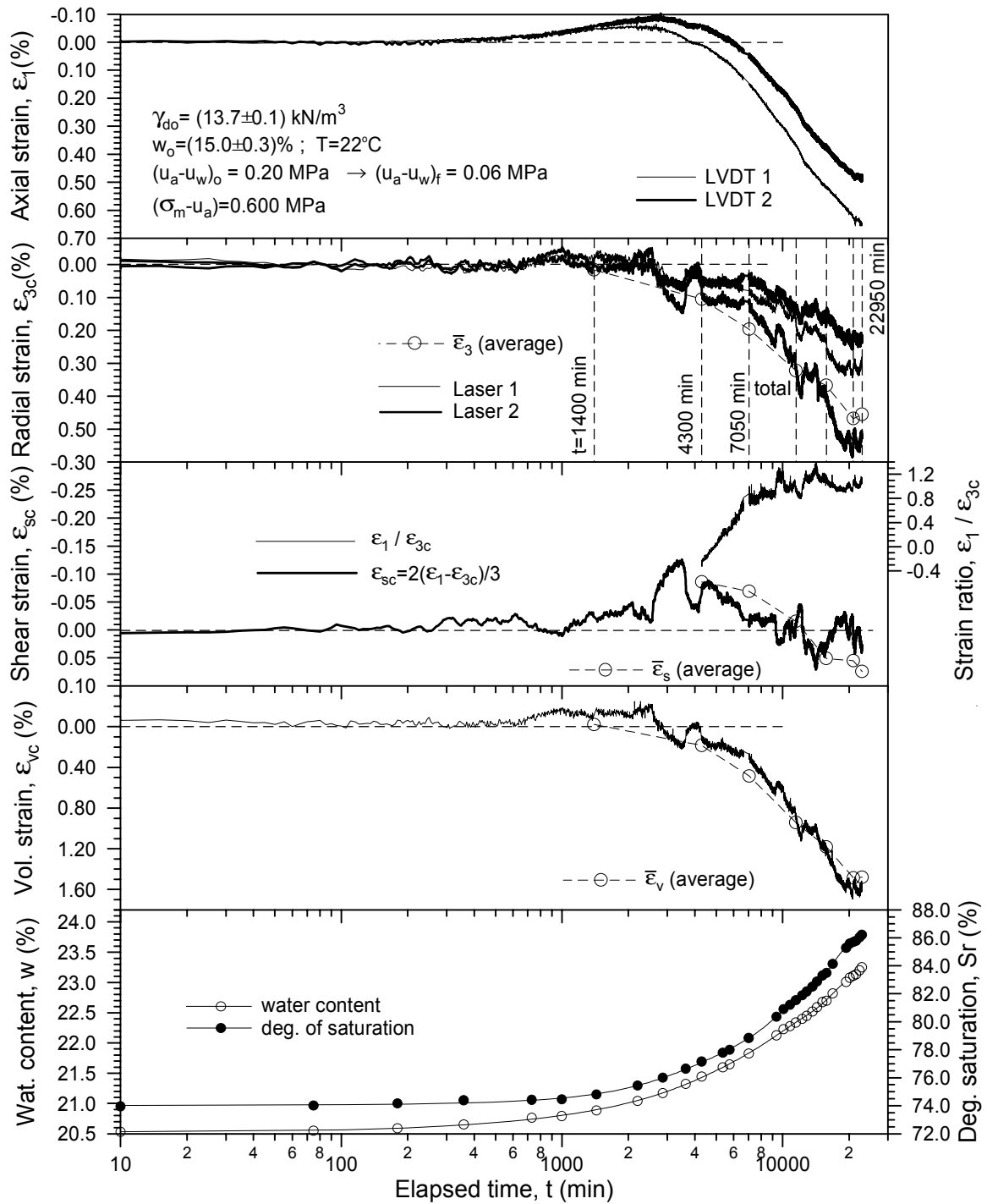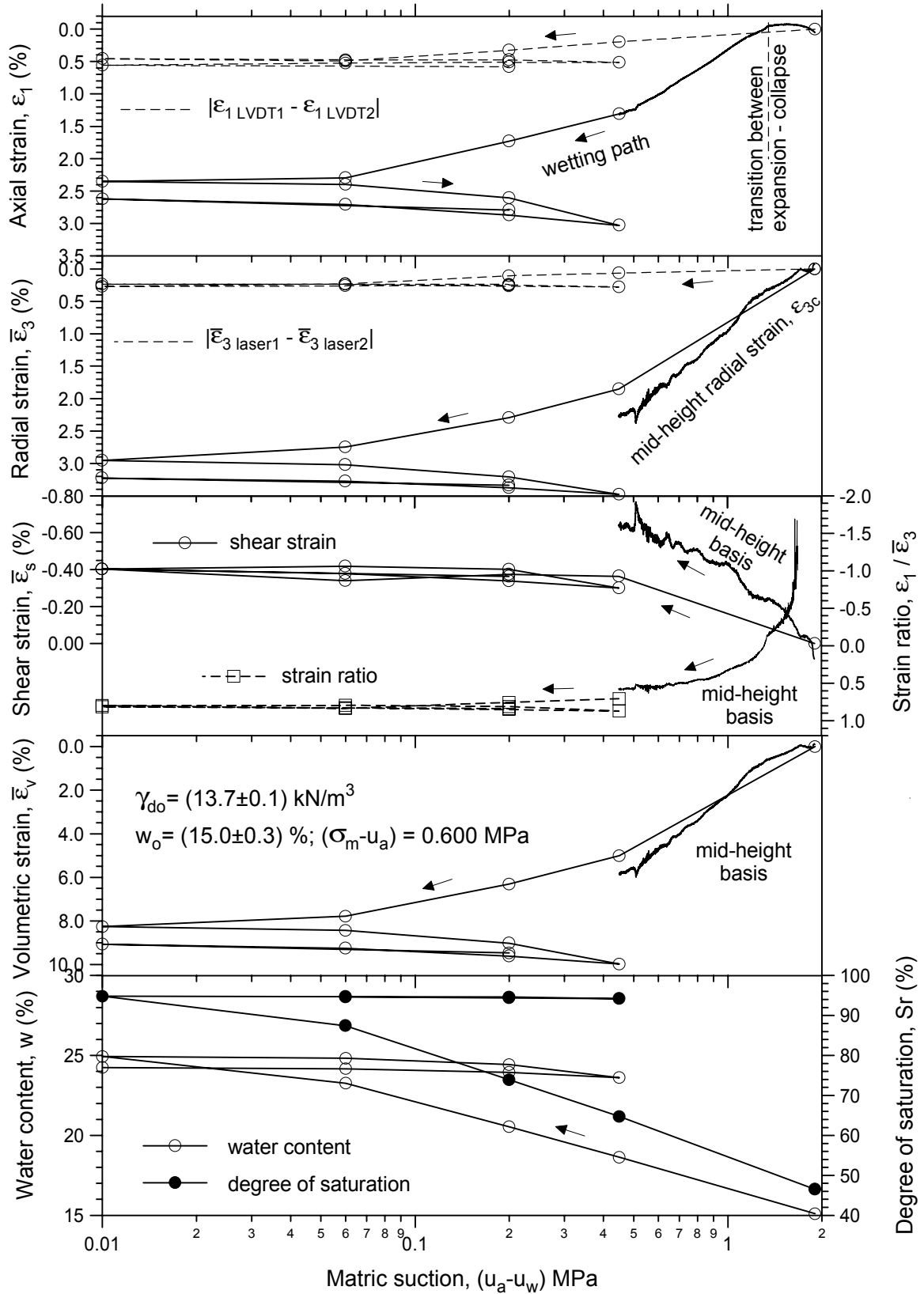
Figure 7.2   Time evolution of axial, radial, shear and volumetric strains, water content and degree of saturation for the high-density packing in a main wetting path (s_o = 0.45 MPa $\rightarrow$ s_f = 0.20 MPa).
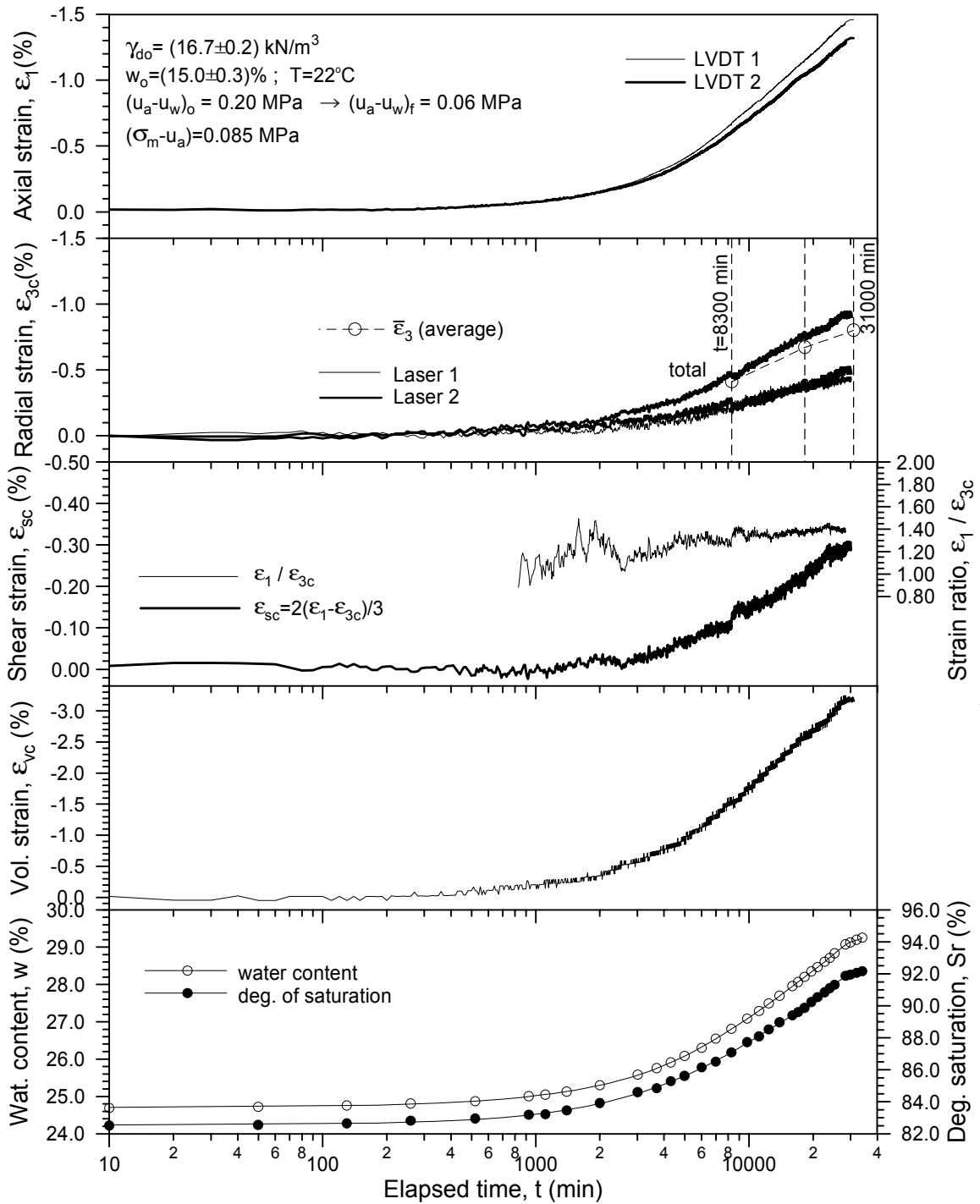
Figure 7.3 Time evolution of axial, radial, shear and volumetric strains, water content and degree of saturation for the high-density packing in a main wetting path ($s_o = 0.20$ MPa $\rightarrow$ $s_f = 0.06$ MPa).
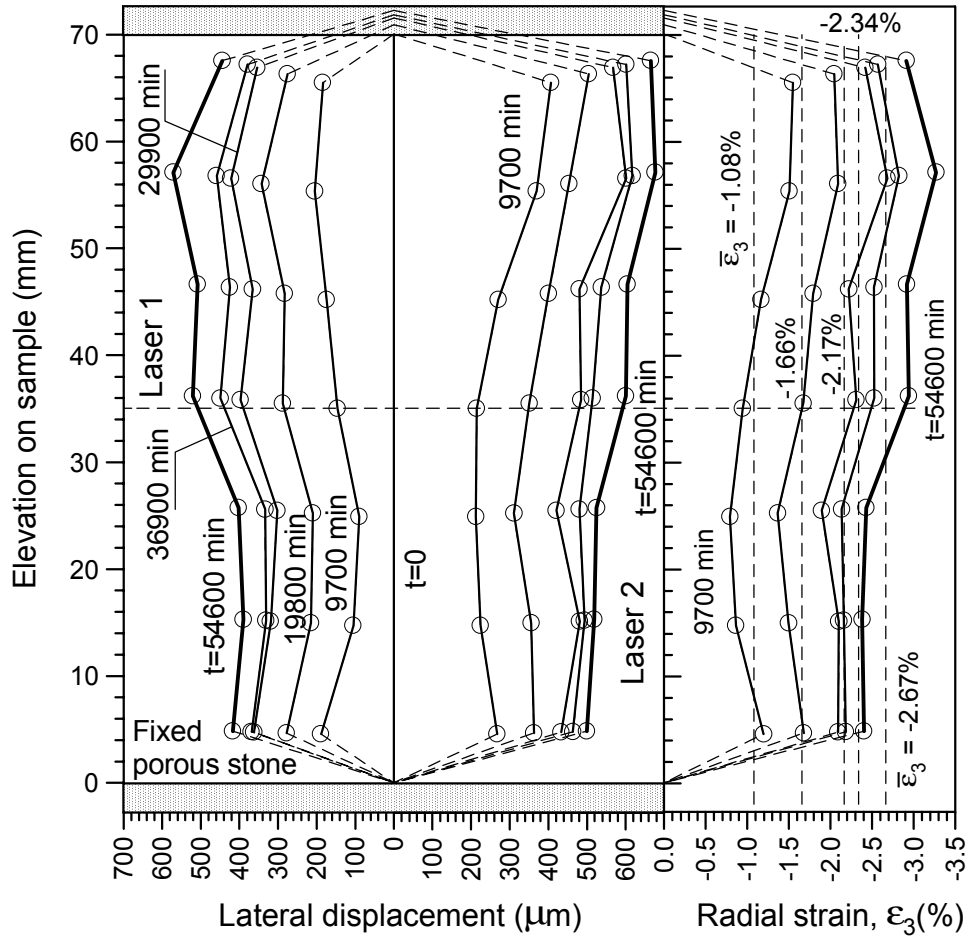
Figure 7.4   Progressive development of the lateral profile and lateral strains of the high-density specimen in a main wetting path ($s_o \approx 1.9$ MPa $\rightarrow s_f = 0.45$ MPa).
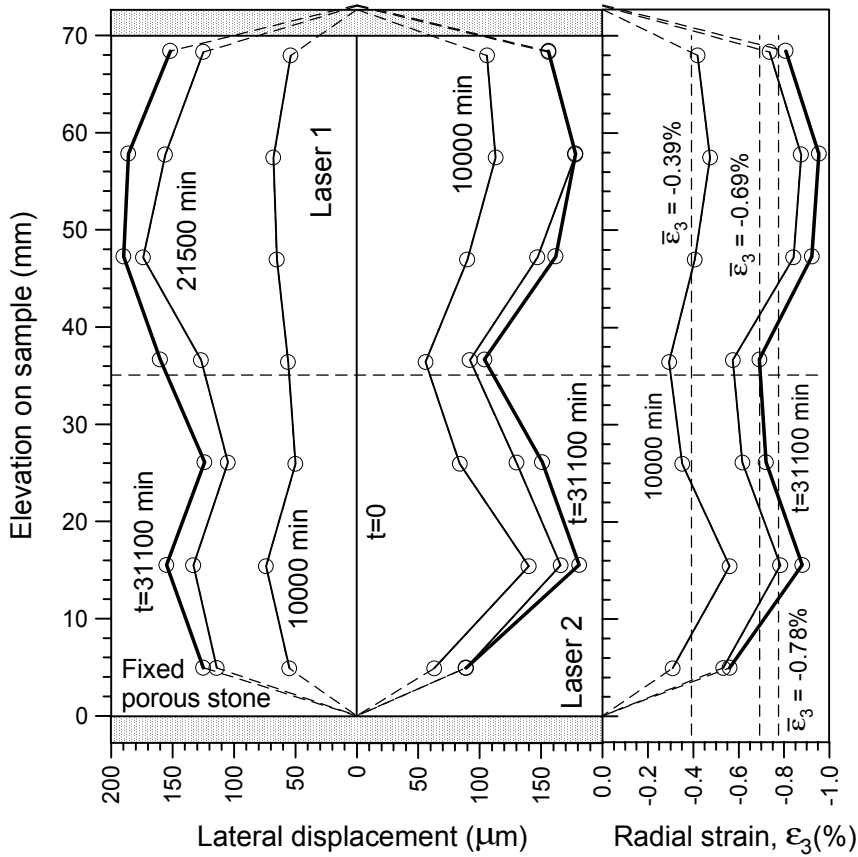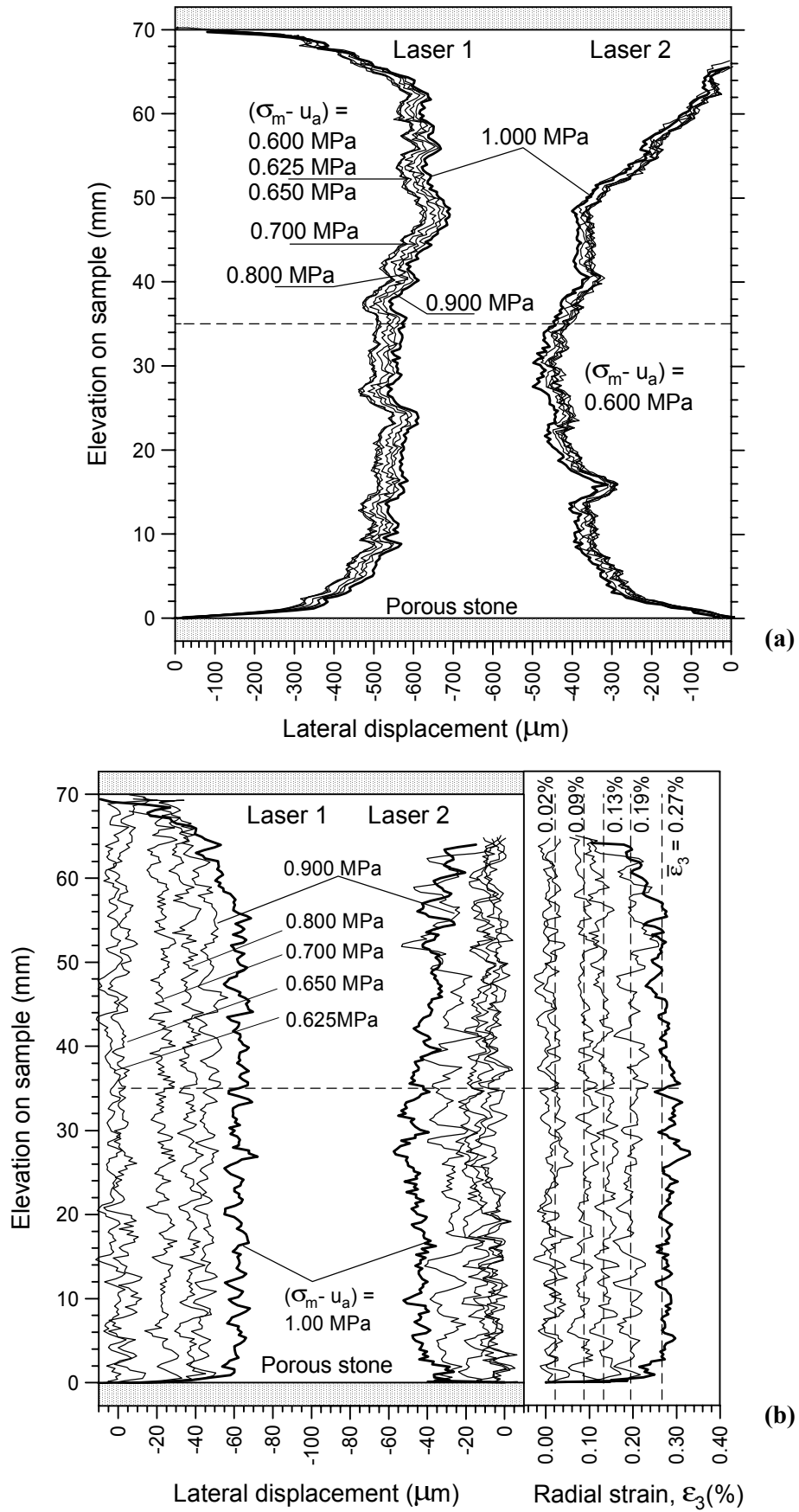
Figure 7.5   Progressive development of the lateral profile and lateral strains of the high-density specimen in a main wetting path ($s_o = 0.45$ MPa $\rightarrow$ $s_f = 0.20$ MPa).
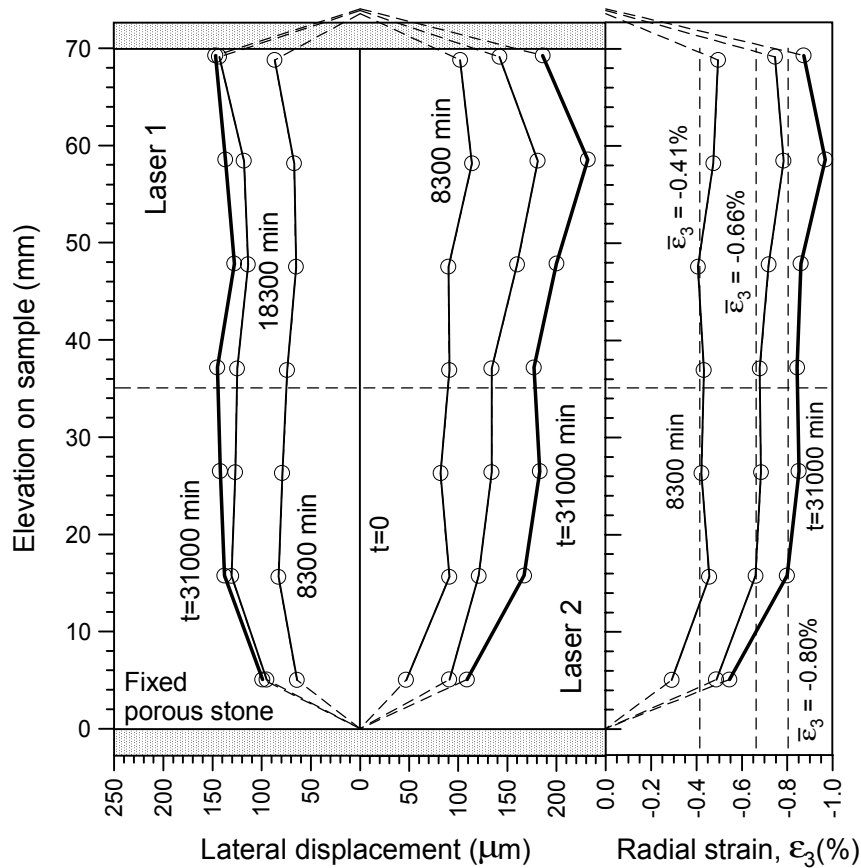
Figure 7.6   Progressive development of the lateral profile and lateral strains of the high-density specimen in a main wetting path ($s_o = 0.20$ MPa $\rightarrow$ $s_f = 0.06$ MPa).

Figure 7.7   Variation of axial, radial, shear and volumetric strains, strain ratio, water content and degree of saturation for the high-density packing in wetting-drying cycles under a constant isotropic net stress.

Figure 7.8   Time evolution of axial, radial, shear and volumetric strains, water content and degree of saturation for the high-porosity packing in a main wetting path ($s_o \approx 1.9$ MPa $\rightarrow s_f = 0.45$ MPa).

Figure 7.9   Time evolution of axial, radial, shear and volumetric strains, water content and degree of saturation for the high-porosity packing in a main wetting path (s_o = 0.45 MPa $\rightarrow$ s_f = 0.20 MPa).

Figure 7.10   Time evolution of axial, radial, shear and volumetric strains, water content and degree of saturation for the high-porosity packing in a main wetting path ($s_o = 0.20$ MPa $\rightarrow$ $s_f = 0.06$ MPa).

Figure 7.11   Time evolution of axial, radial, shear and volumetric strains, water content and degree of saturation for the high-porosity packing in a main drying path (s_o = 0.20 MPa $\rightarrow$ s_f = 0.45 MPa).
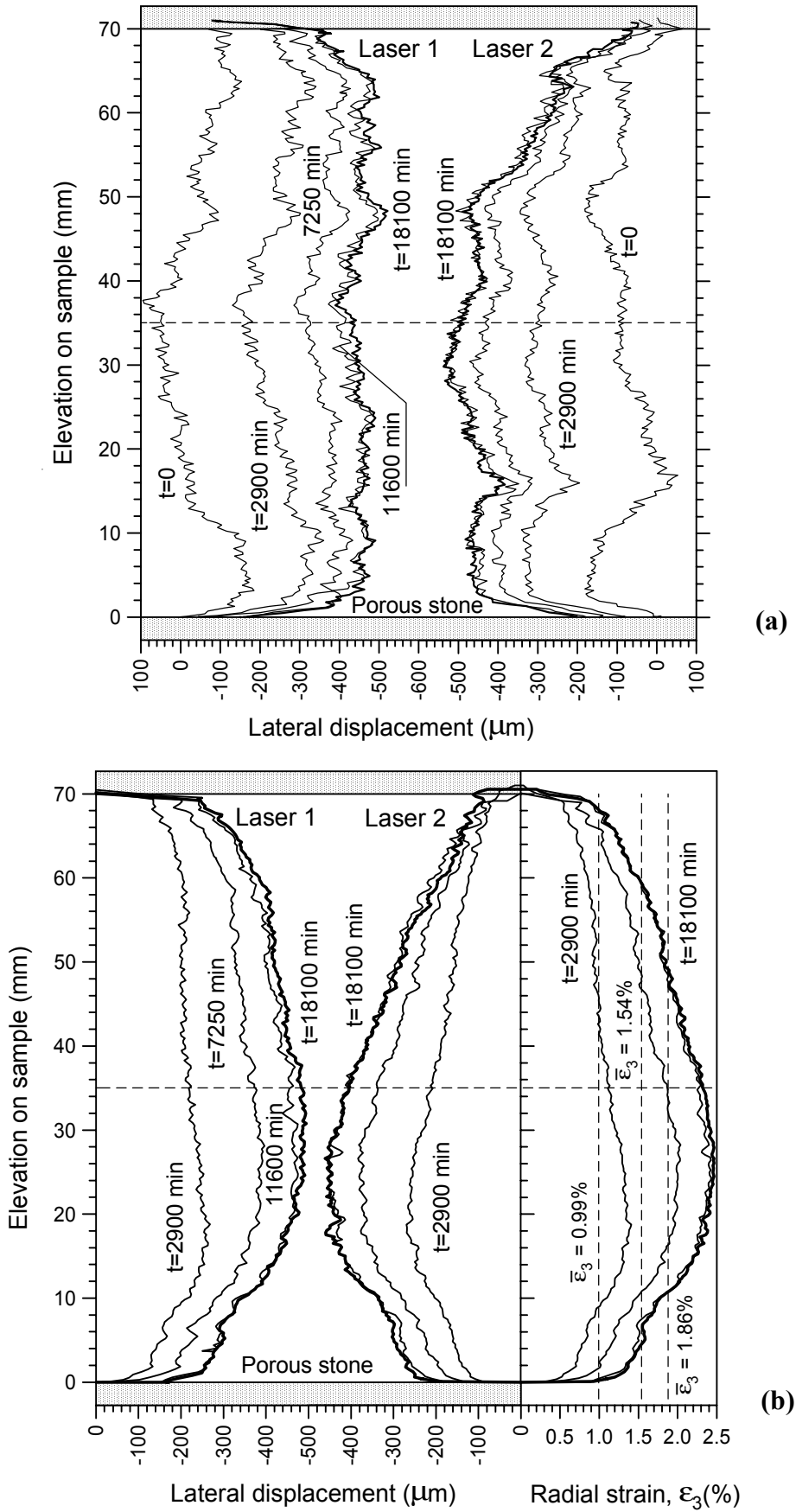
Figure 7.12   Progressive development of the lateral profile and lateral strains of the high-porosity specimen in a main wetting path ($s_o \approx 1.9$ MPa $\rightarrow s_f = 0.45$ MPa): a) raw data and b) processed data.
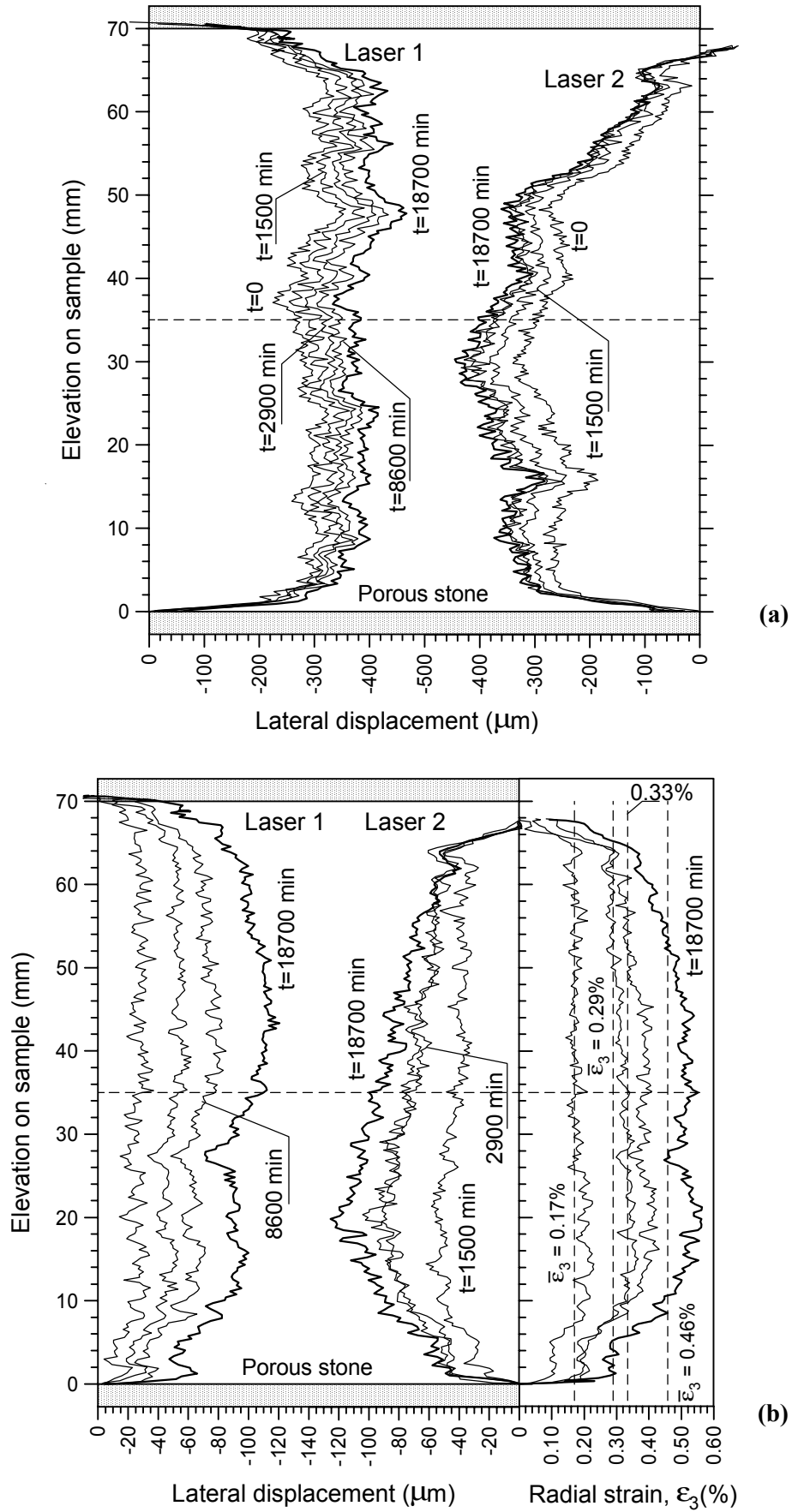
Figure 7.13   Progressive development of the lateral profile and lateral strains of the high-porosity specimen in a main wetting path ($s_o = 0.45$ MPa $\rightarrow s_f = 0.20$ MPa): a) raw data and b) processed data.
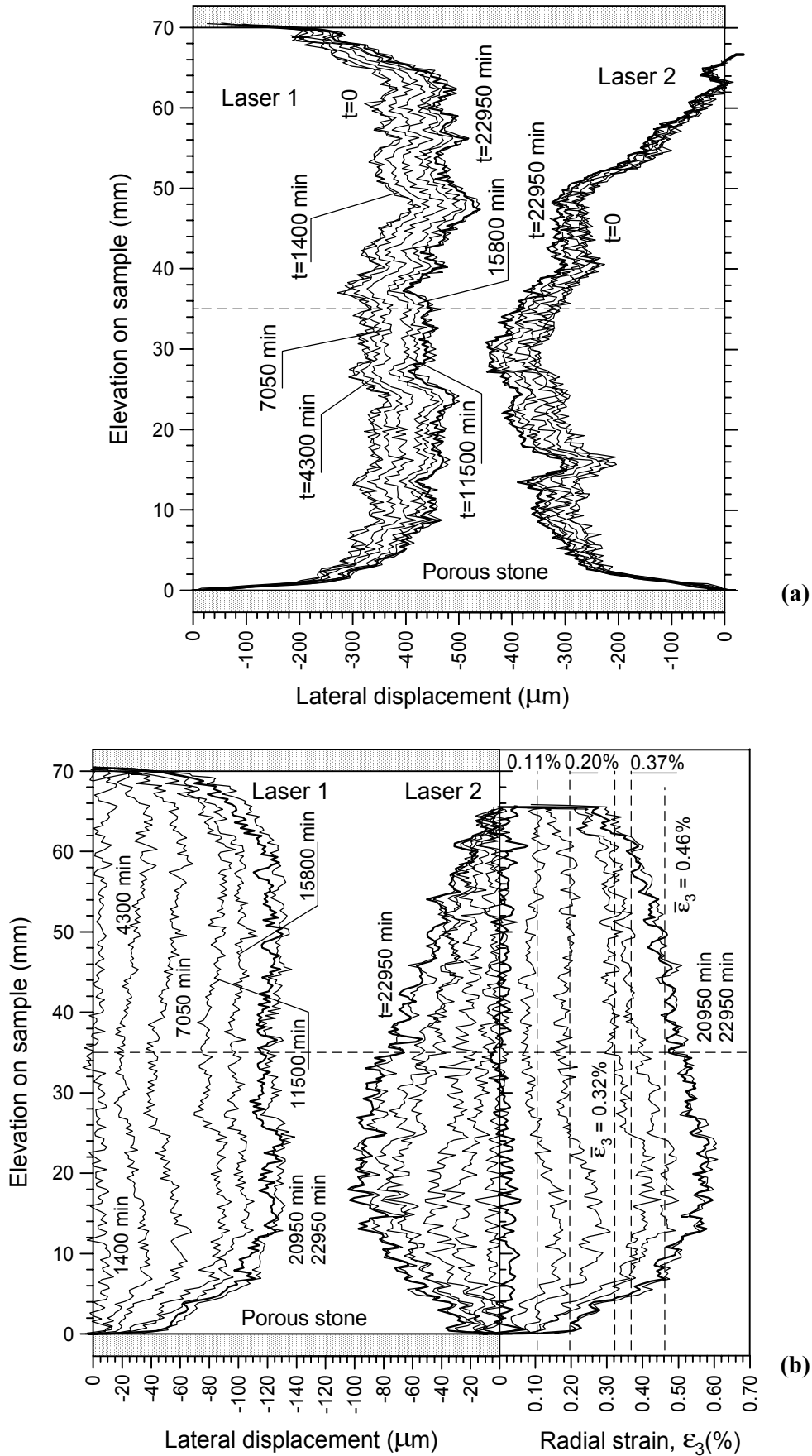
Figure 7.14 Progressive development of the lateral profile and lateral strains of the high-porosity specimen in a main wetting path ($s_o = 0.20$ MPa $\rightarrow s_f = 0.06$ MPa): a) raw data and b) processed data.

Figure 7.15   Variation of axial, radial, shear and volumetric strains, strain ratio, water content and degree of saturation for the high-porosity packing in wetting-drying cycles under a constant isotropic net stress.
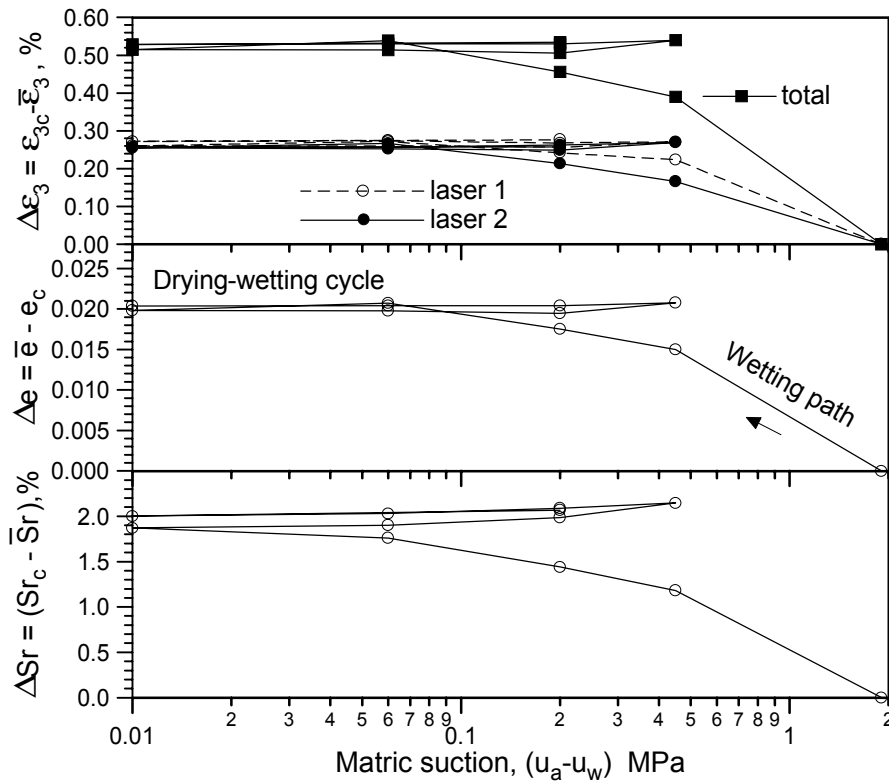
Figure 7.16   Differences between measured mid-height radial strains (subscript c) and calculated mean value radial strains and their consequences on void ratio and degree of saturation errors.
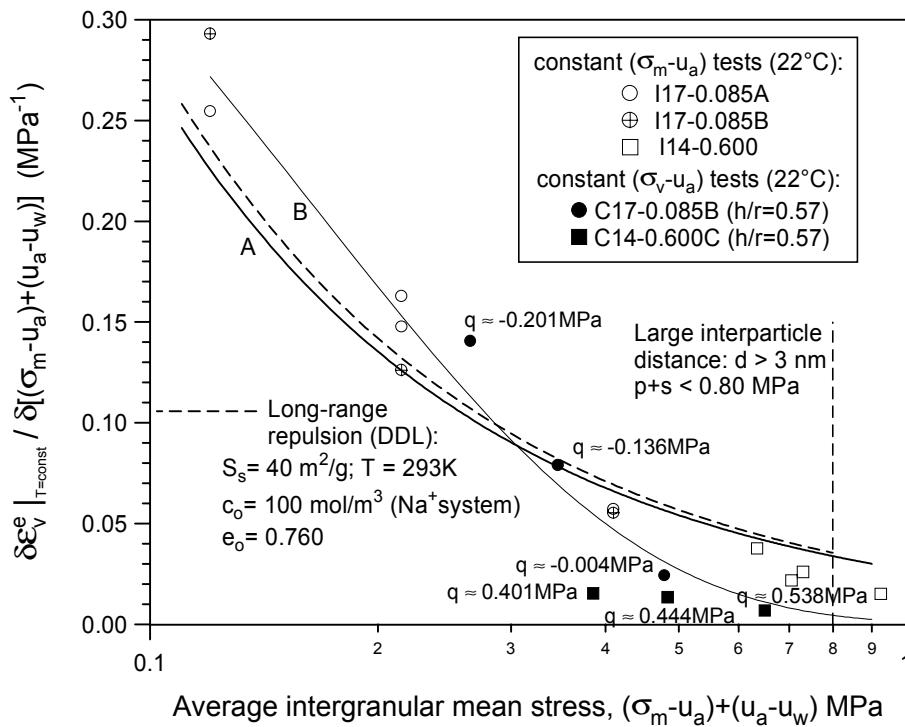
Figure 7.17   Reversible changes in volumetric strain associated with changes in intergranular mean stress obtained from constant $(\sigma_m - u_a)$ and $(\sigma_v - u_a)$ data.
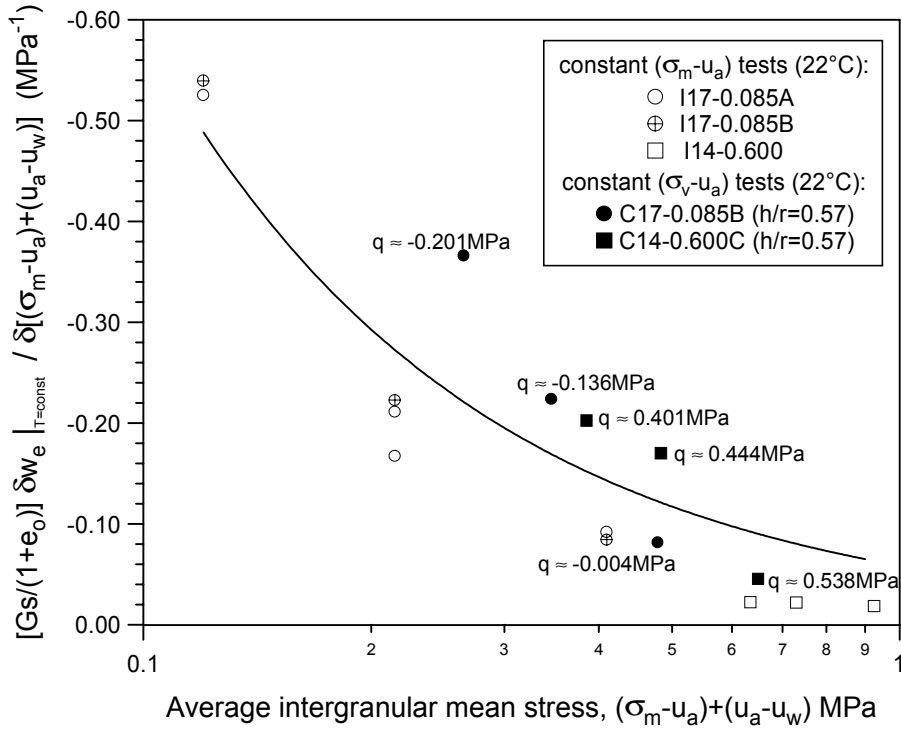
Figure 7.18   Reversible changes in work conjugated variable of matric suction with changes in intergranular mean stress obtained from constant (σ_m-u_a) and (σ_v-u_a) data.
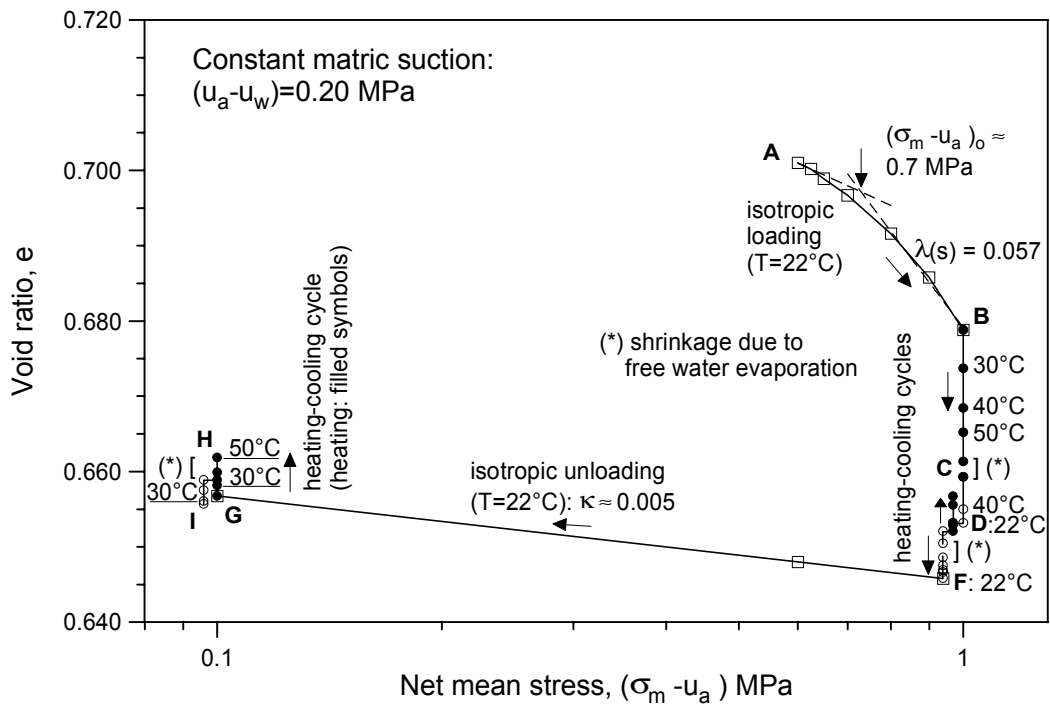
Figure 7.19   Void ratio-net mean stress diagram showing loading/unloading and heating/cooling paths at constant matric suction.
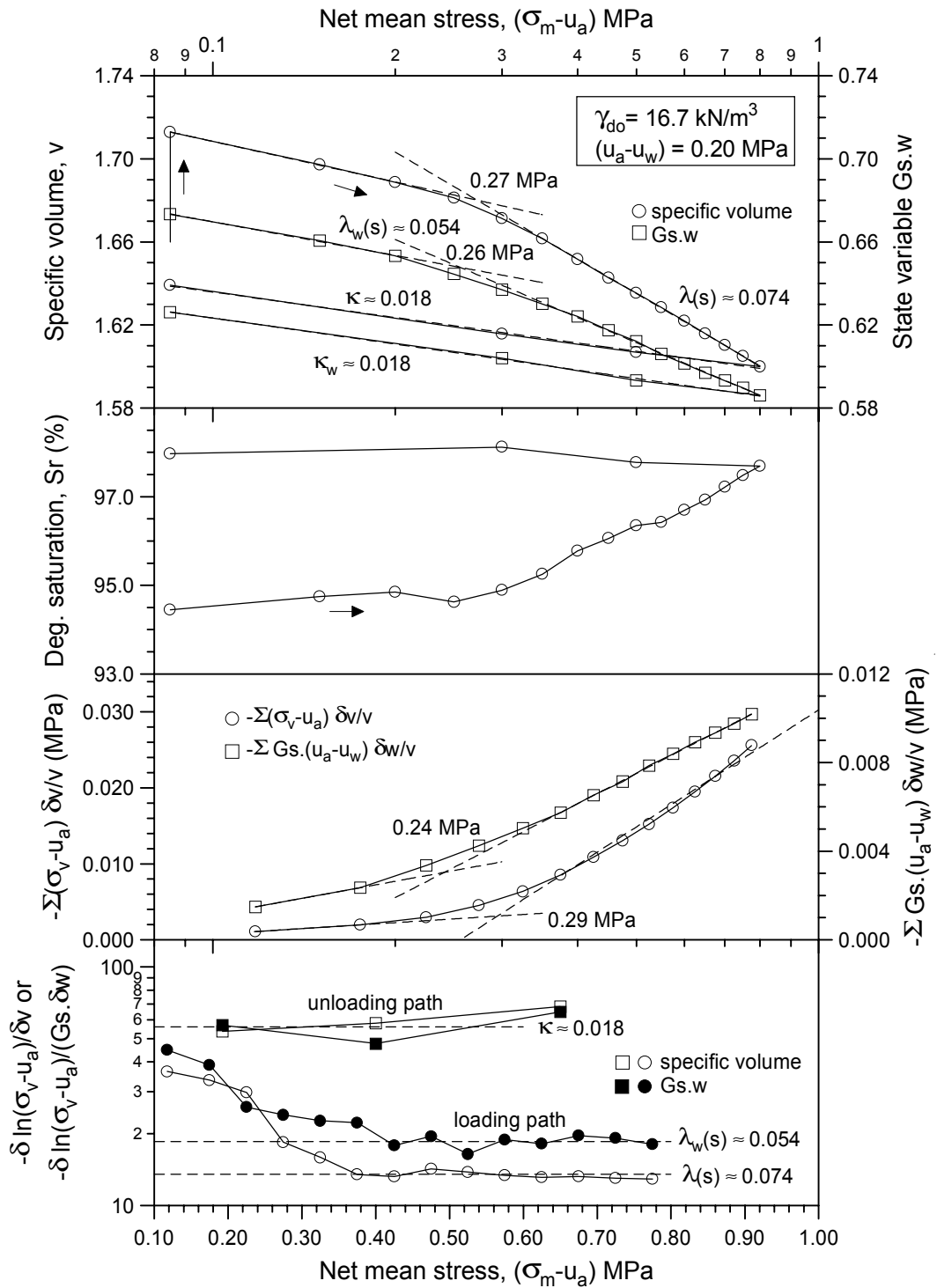
Figure 7.20   Loading-unloading paths on the high-density fabric at constant $(u_a-u_w) = 0.20$ MPa. Evolution of specific volume, state variable Gs.w and degree of saturation.

Figure 7.21   Progressive development of the lateral profile and lateral strains of the high-porosity specimen in a loading path at s = 0.20 MPa: a) raw data and b) processed data.
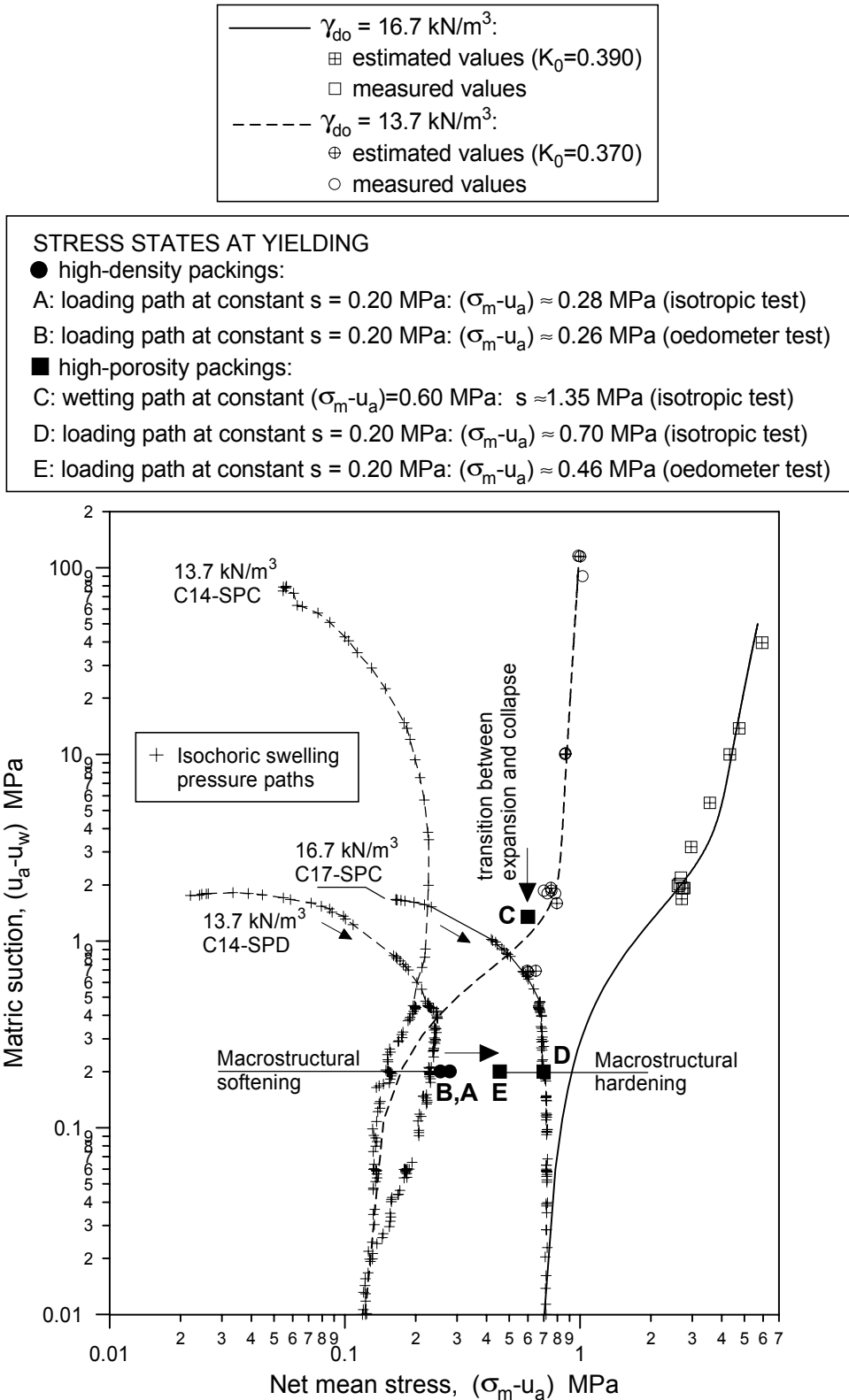
Figure 7.22   LC yield curves for both packings obtained from static compaction and suction controlled tests. Stress states at yielding and strain hardening/softening effects.
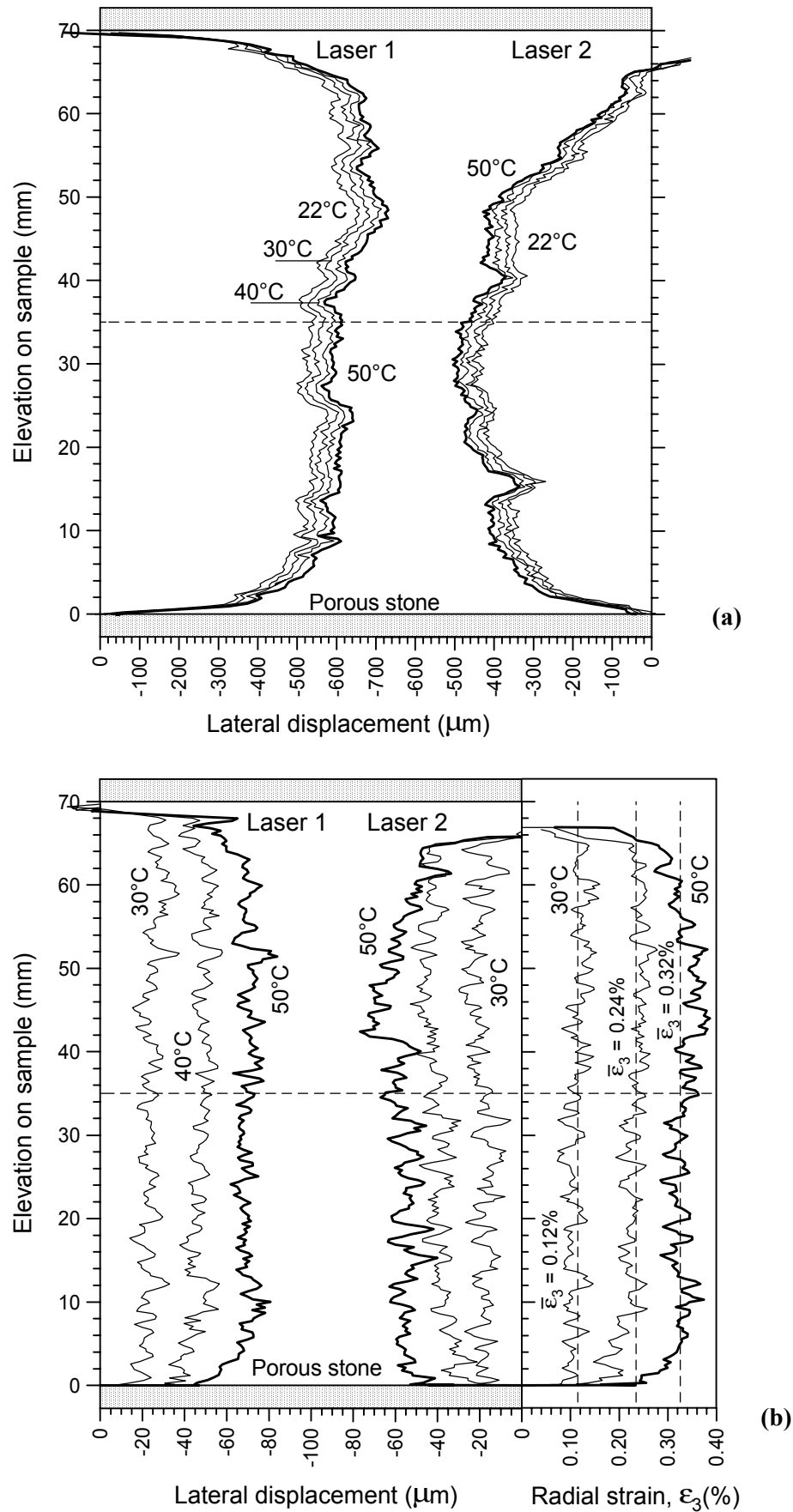
Figure 7.23 Progressive development of the lateral profile and lateral strains of the high-porosity specimen in a drained heating path at s = 0.20 MPa and $(\sigma_m-u_a) = 1.00$ MPa: a) raw data and b) processed data.
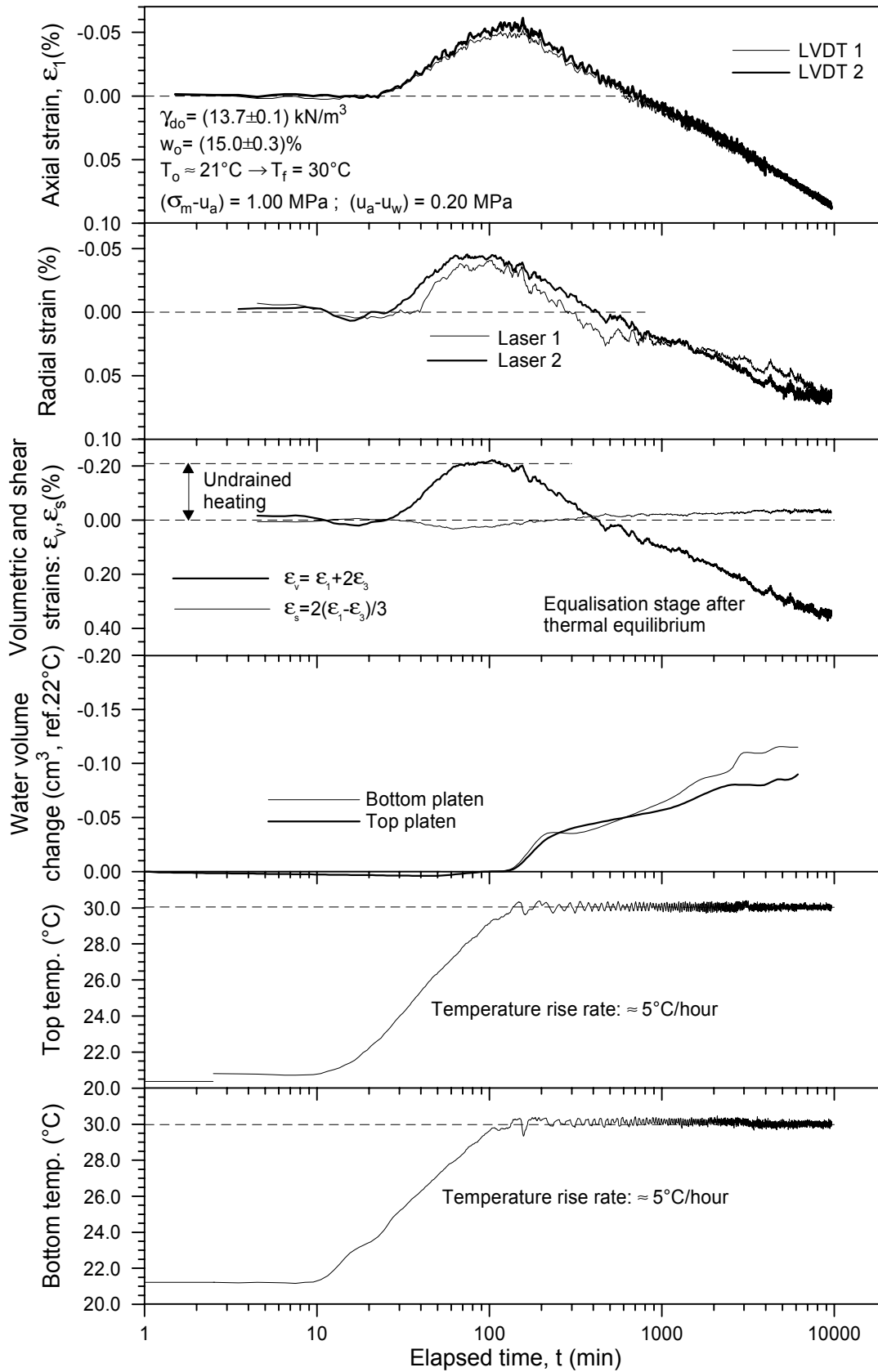
Figure 7.24   Time evolution of strains and water volume change for a normally consolidated state during heating and regulation phase at p = 1.00 MPa and s = 0.20 MPa (21°C to 30°C in path B-C).
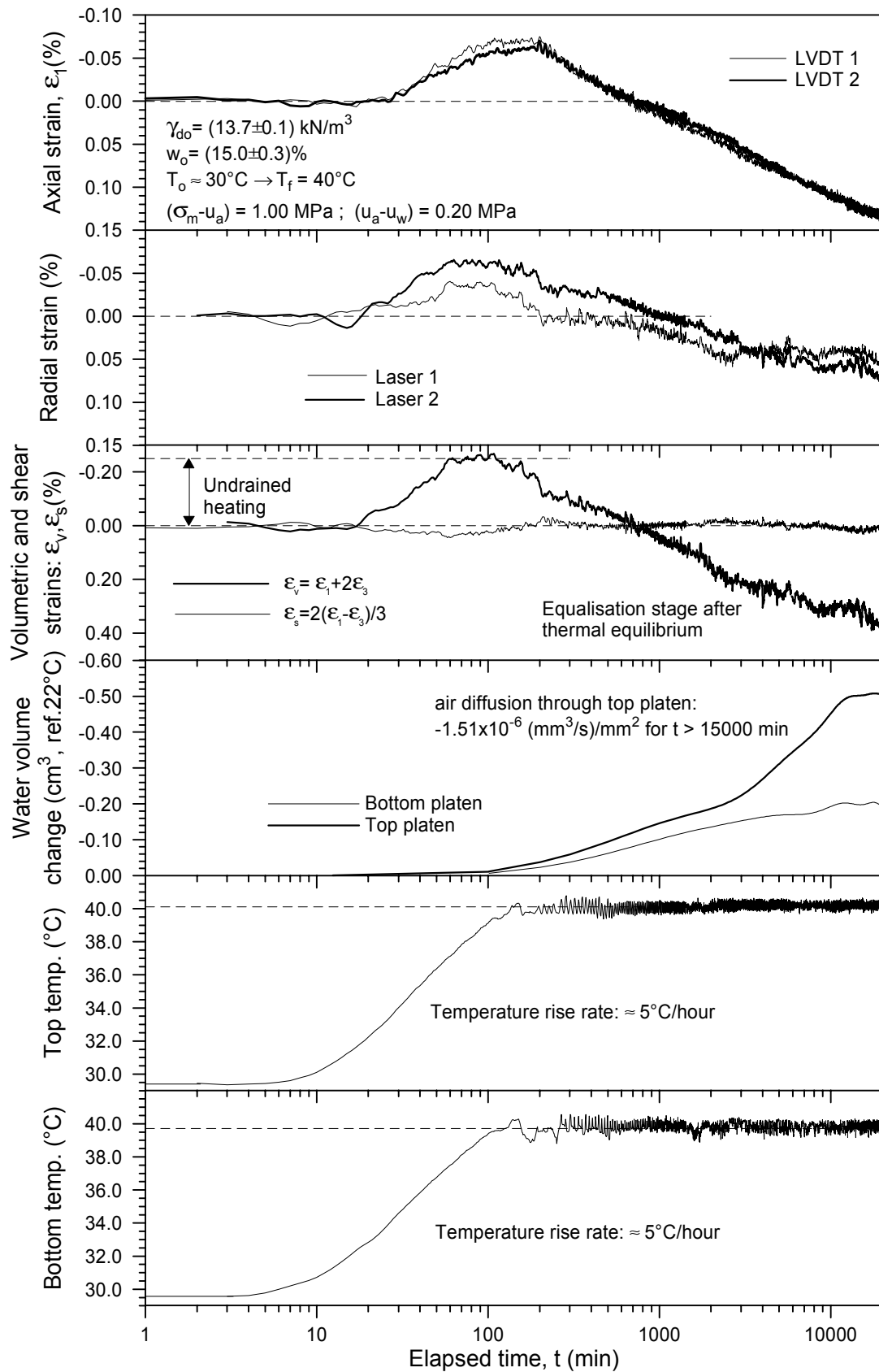
Figure 7.25   Time evolution of strains and water volume change for a normally consolidated state during heating and regulation phase at p = 1.00 MPa and s = 0.20 MPa (30°C to 40°C in path B-C).
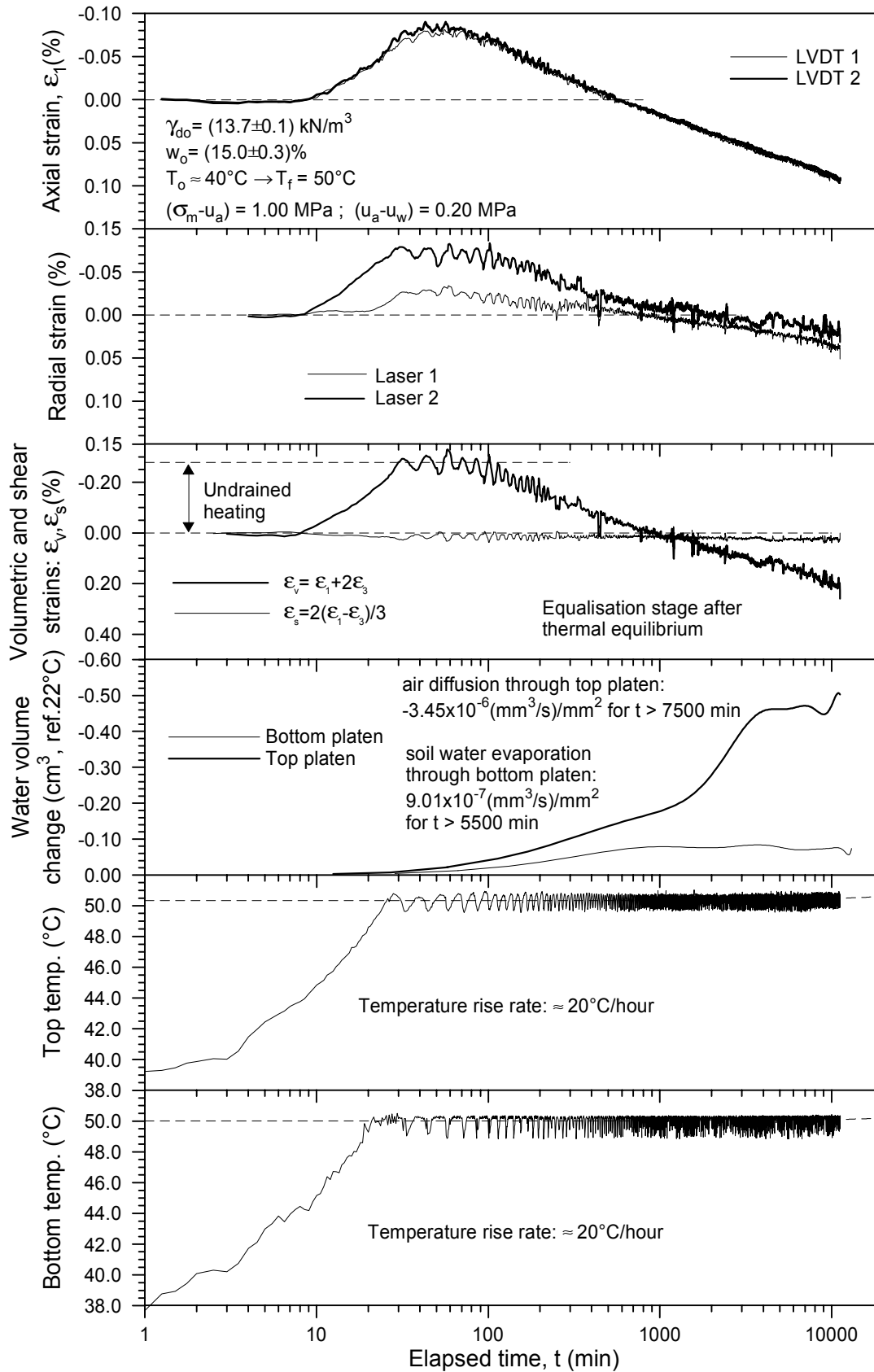
Figure 7.26   Time evolution of strains and water volume change for a normally consolidated state during heating and regulation phase at p = 1.00 MPa and s = 0.20 MPa (40°C to 50°C in path B-C).
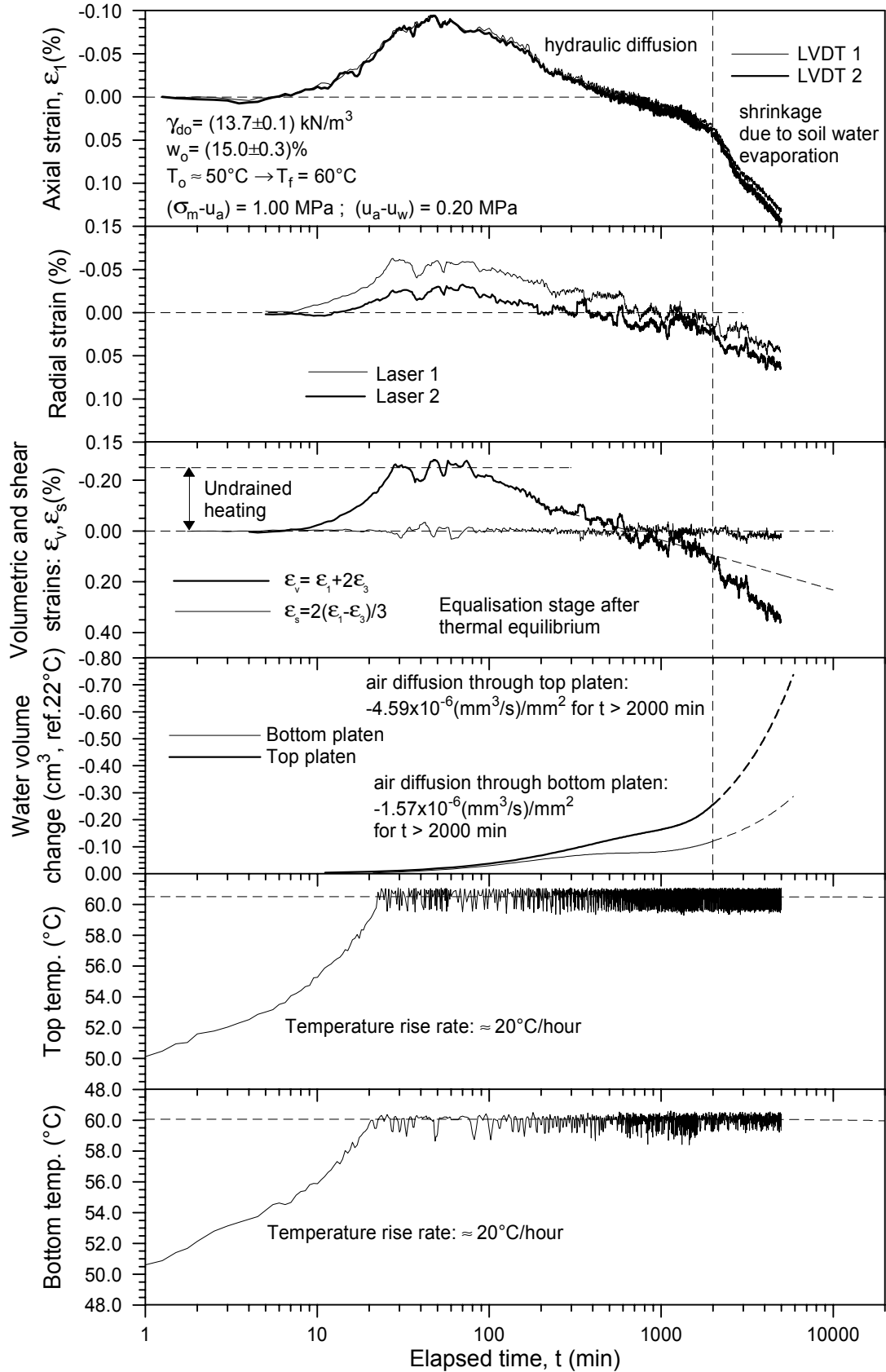
Figure 7.27 Time evolution of strains and water volume change for a normally consolidated state during heating and regulation phase at p = 1.00 MPa and s = 0.20 MPa (50°C to 60°C in path B-C).
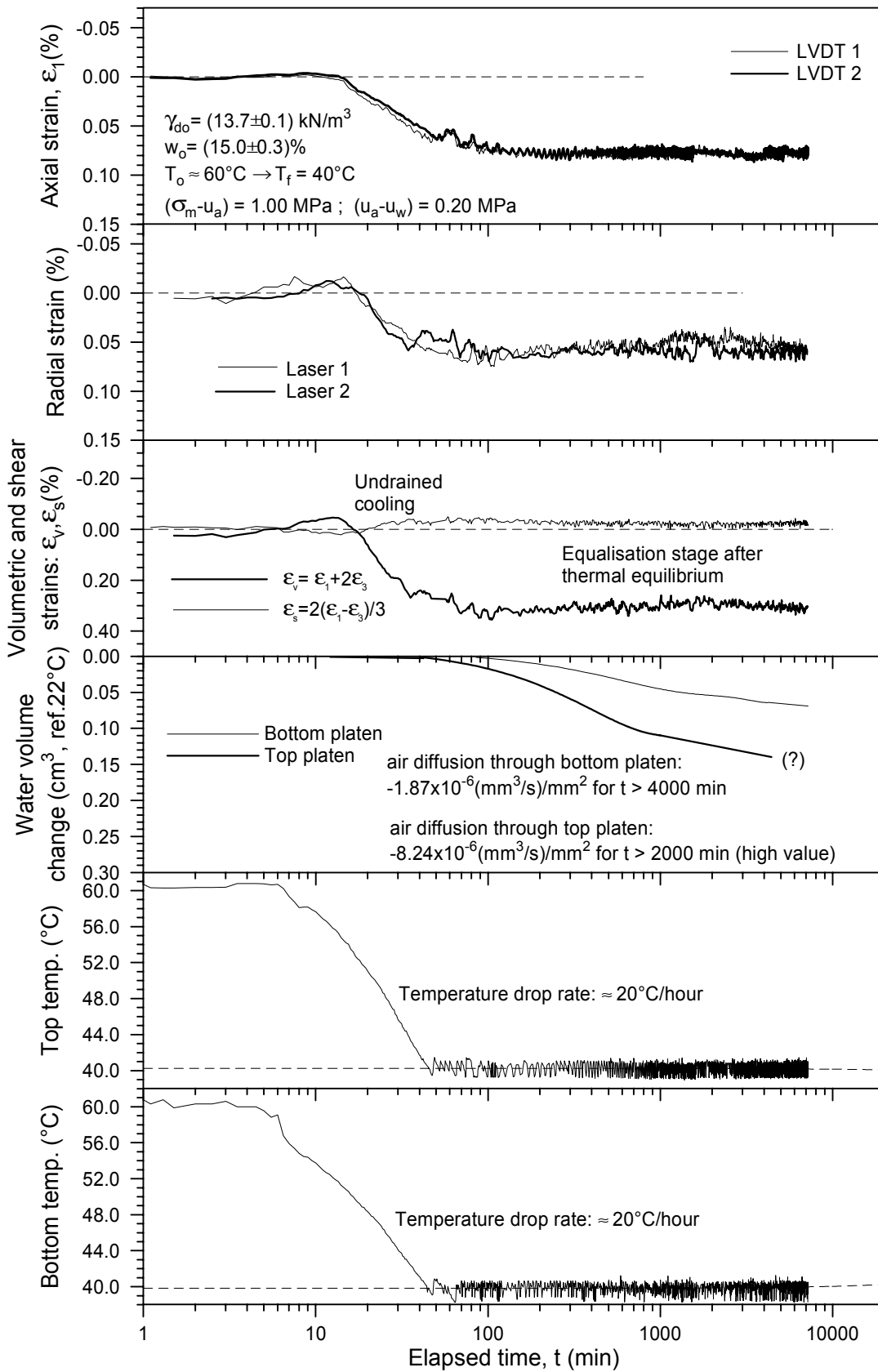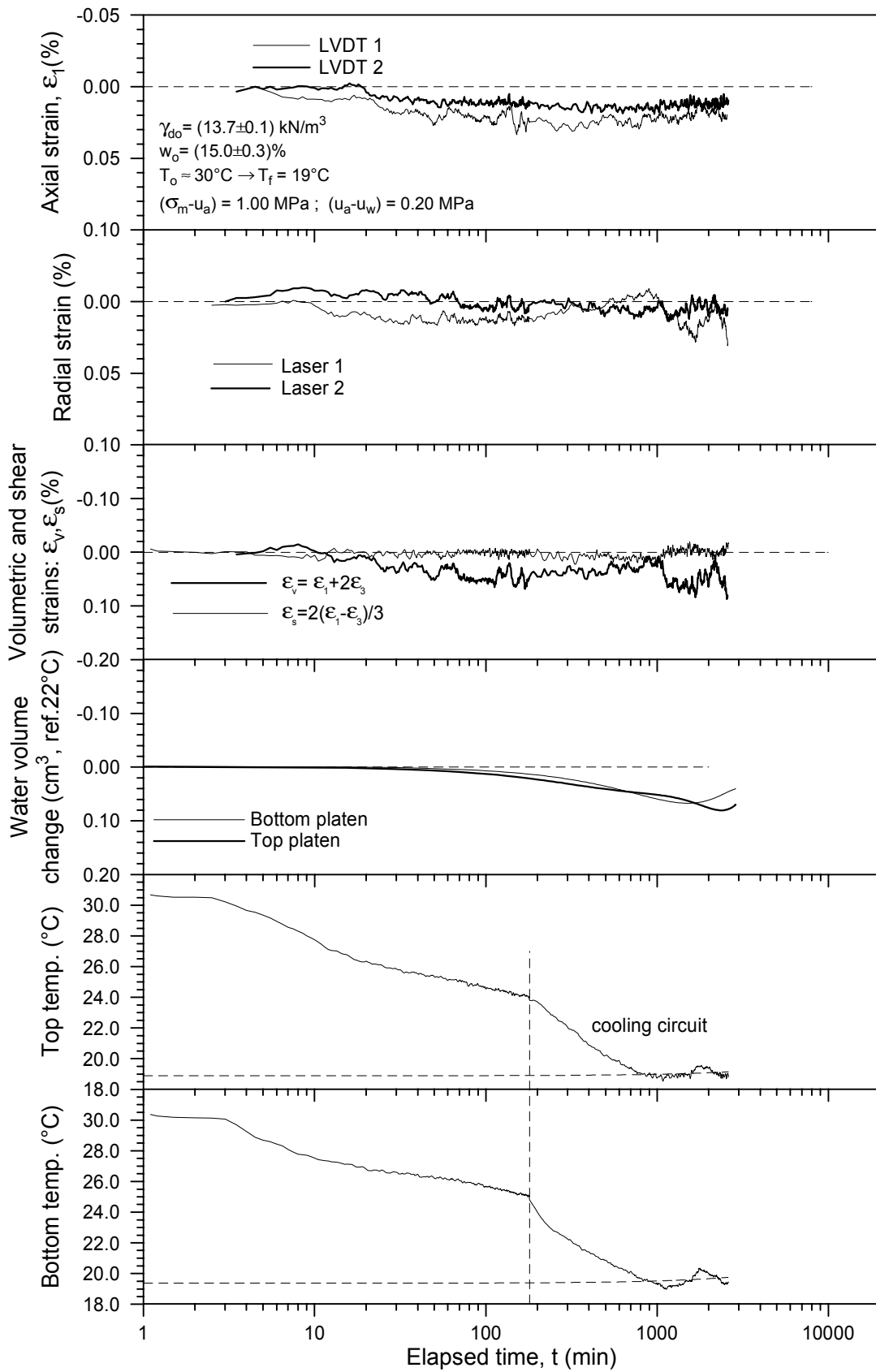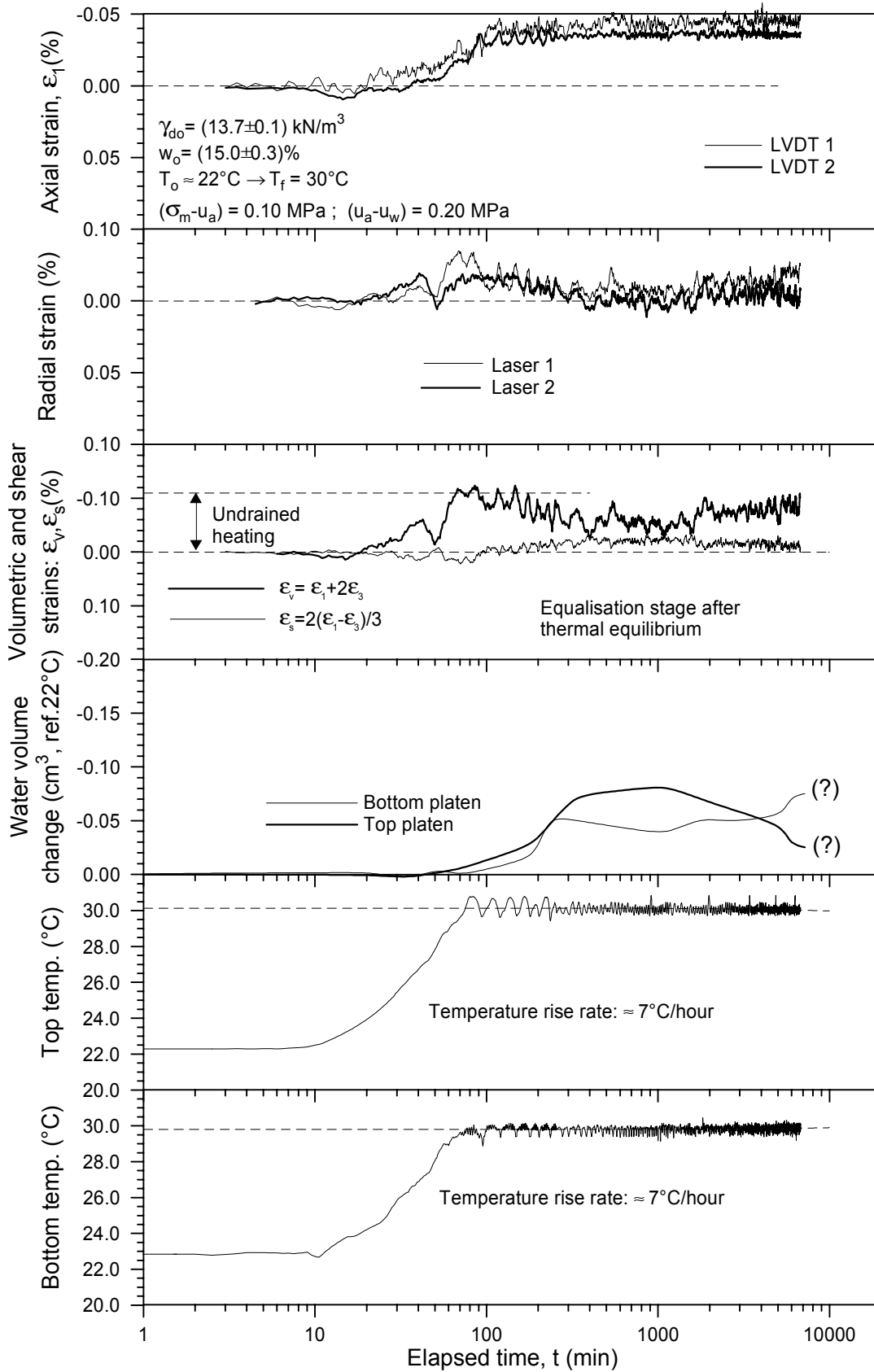
Figure 7.28 Time evolution of strains and water volume change during cooling and regulation phase at p = 1.00 MPa and s = 0.20 MPa (60°C to 40°C in path C-D).
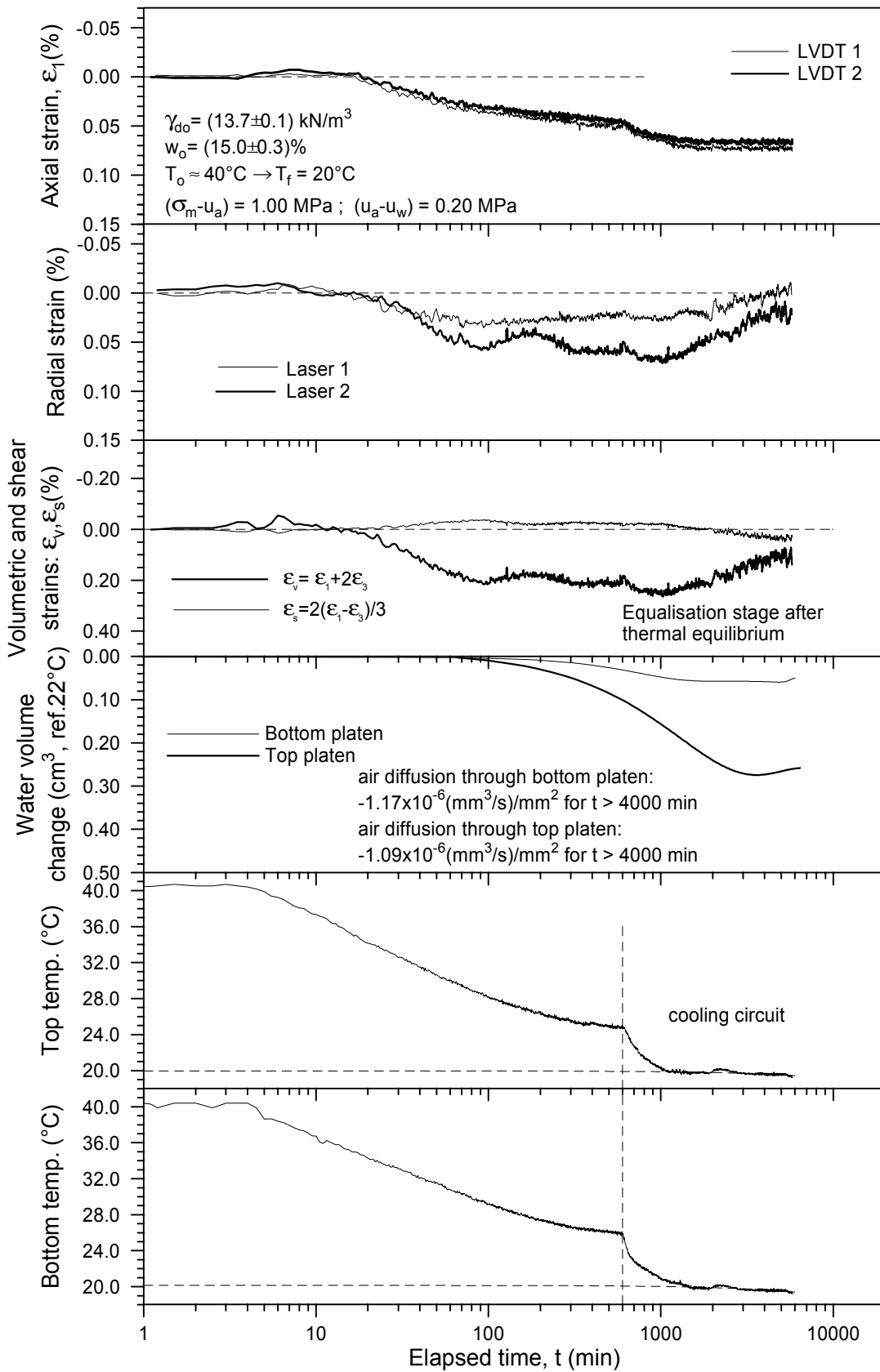
Figure 7.29   Time evolution of strains and water volume change during cooling and regulation phase at p = 1.00 MPa and s = 0.20 MPa (40°C to 20°C in path C-D).
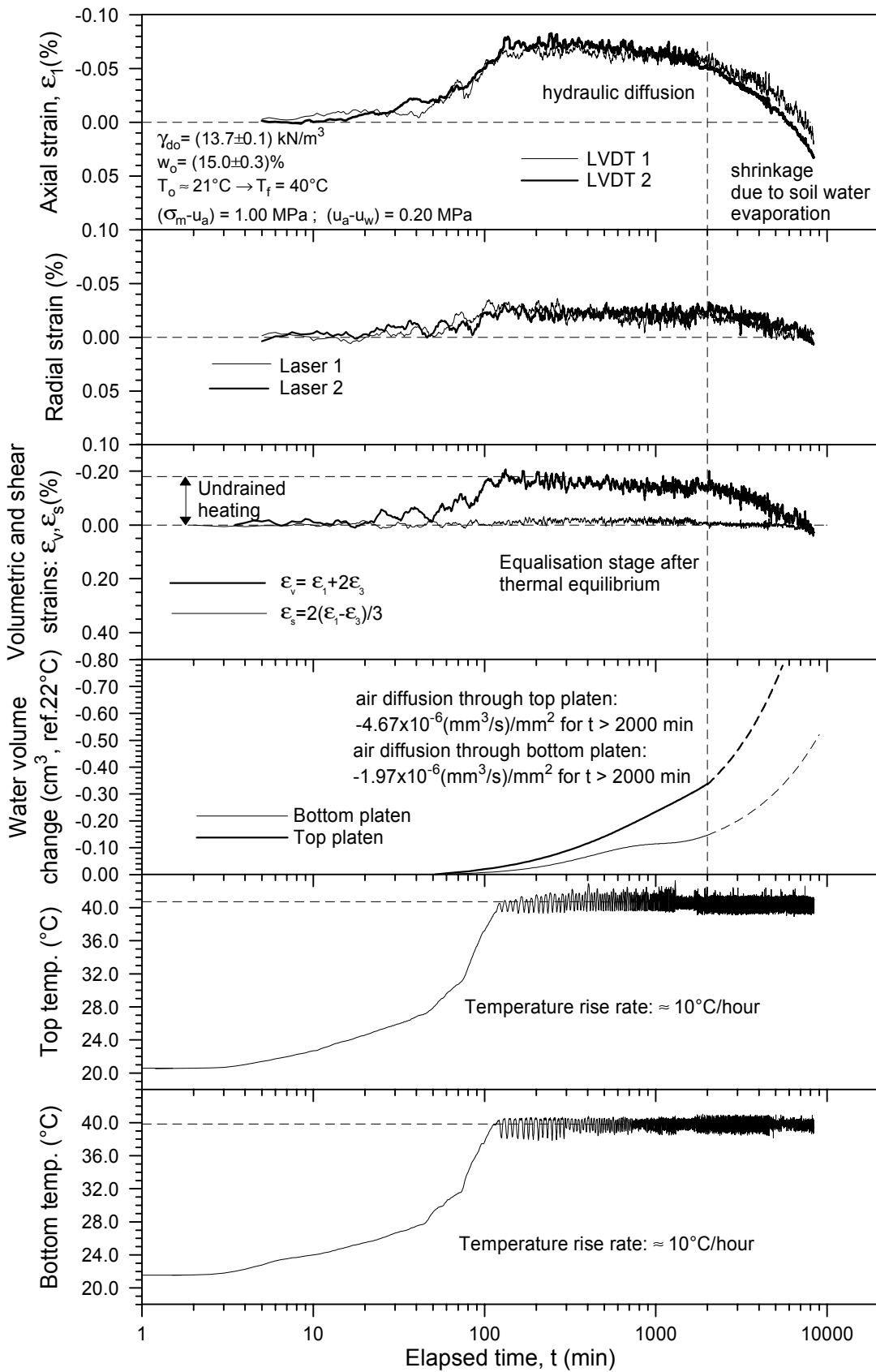
Figure 7.30   Time evolution of strains and water volume change during heating and regulation phase at p = 1.00 MPa and s = 0.20 MPa (21°C to 40°C in path D-E).
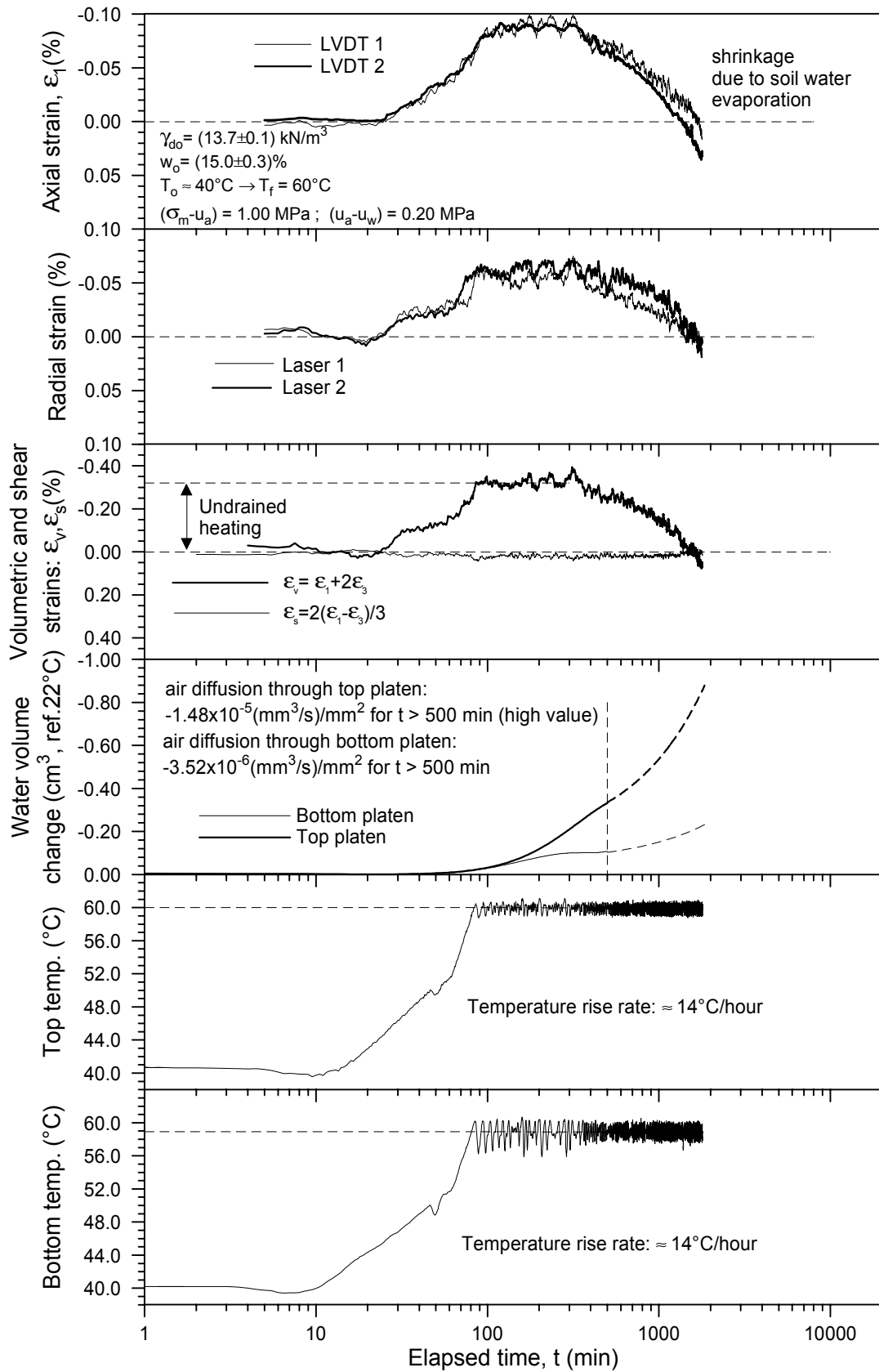
Figure 7.31 Time evolution of strains and water volume change during heating and regulation phase at p = 1.00 MPa and s = 0.20 MPa (40°C to 60°C in path D-E).
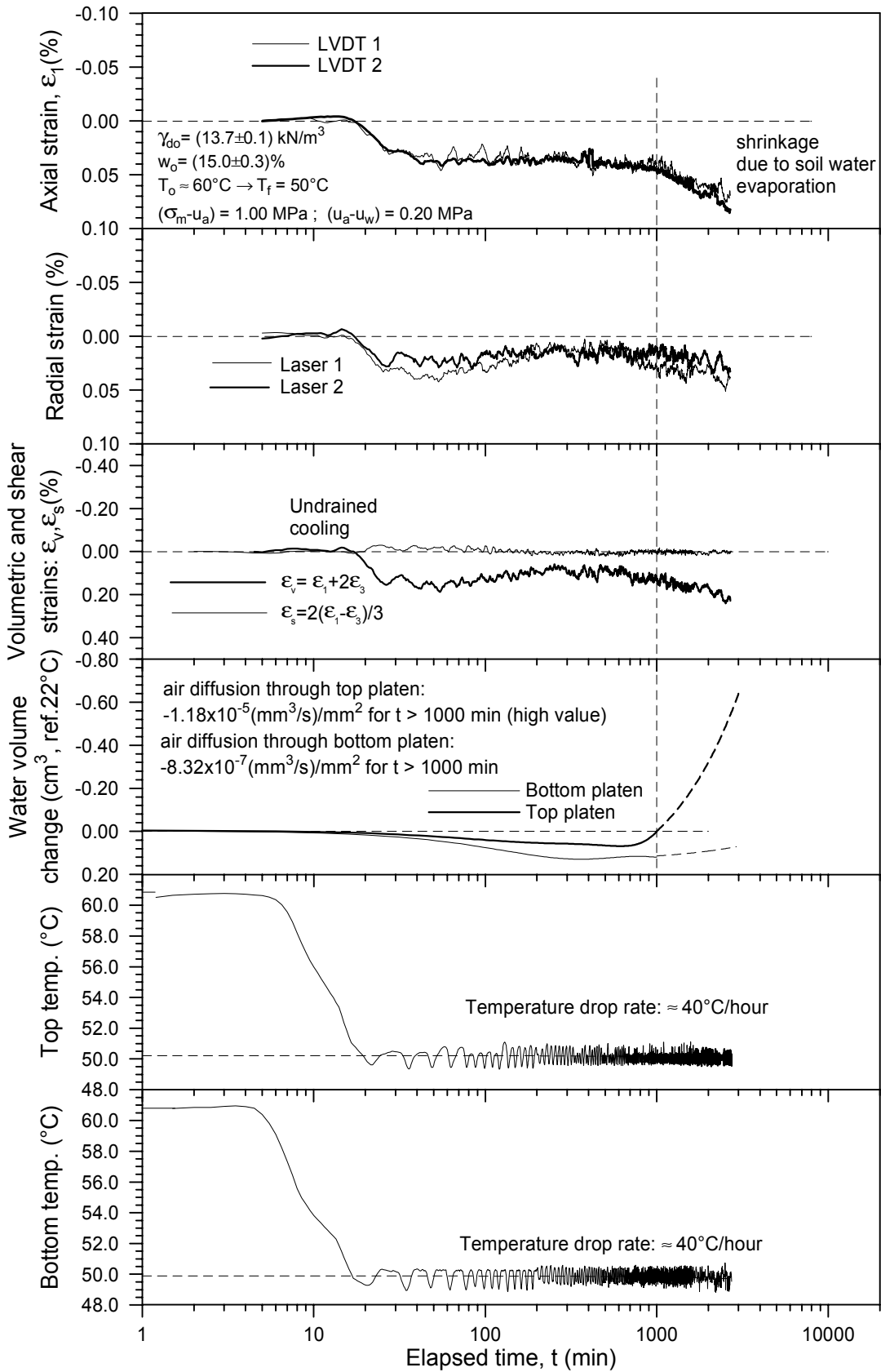
Figure 7.32   Time evolution of strains and water volume change during cooling and regulation phase at p = 1.00 MPa and s = 0.20 MPa (60°C to 50°C in path E-F).
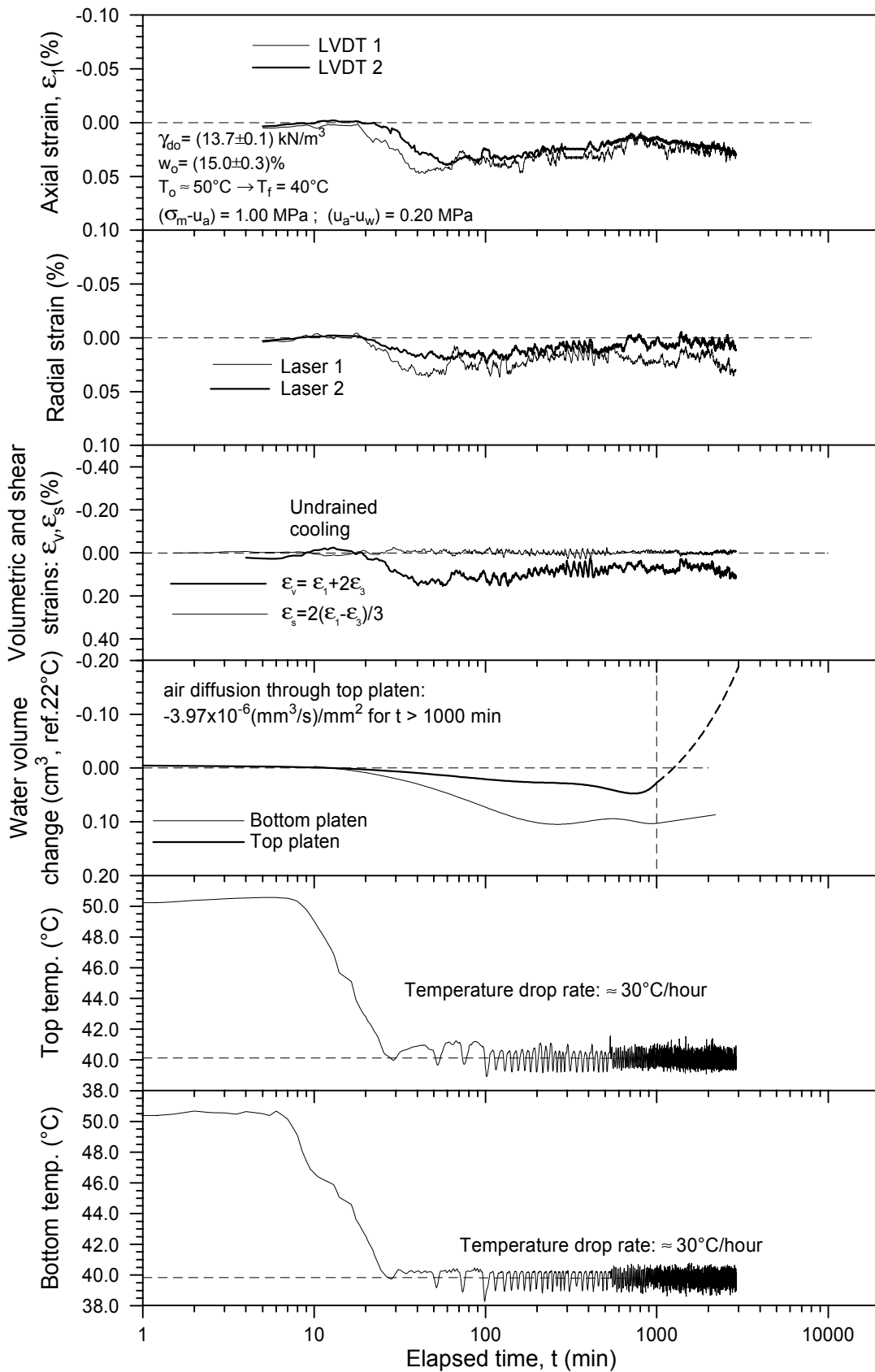
Figure 7.33   Time evolution of strains and water volume change during cooling and regulation phase at p = 1.00 MPa and s = 0.20 MPa (50°C to 40°C in path E-F).
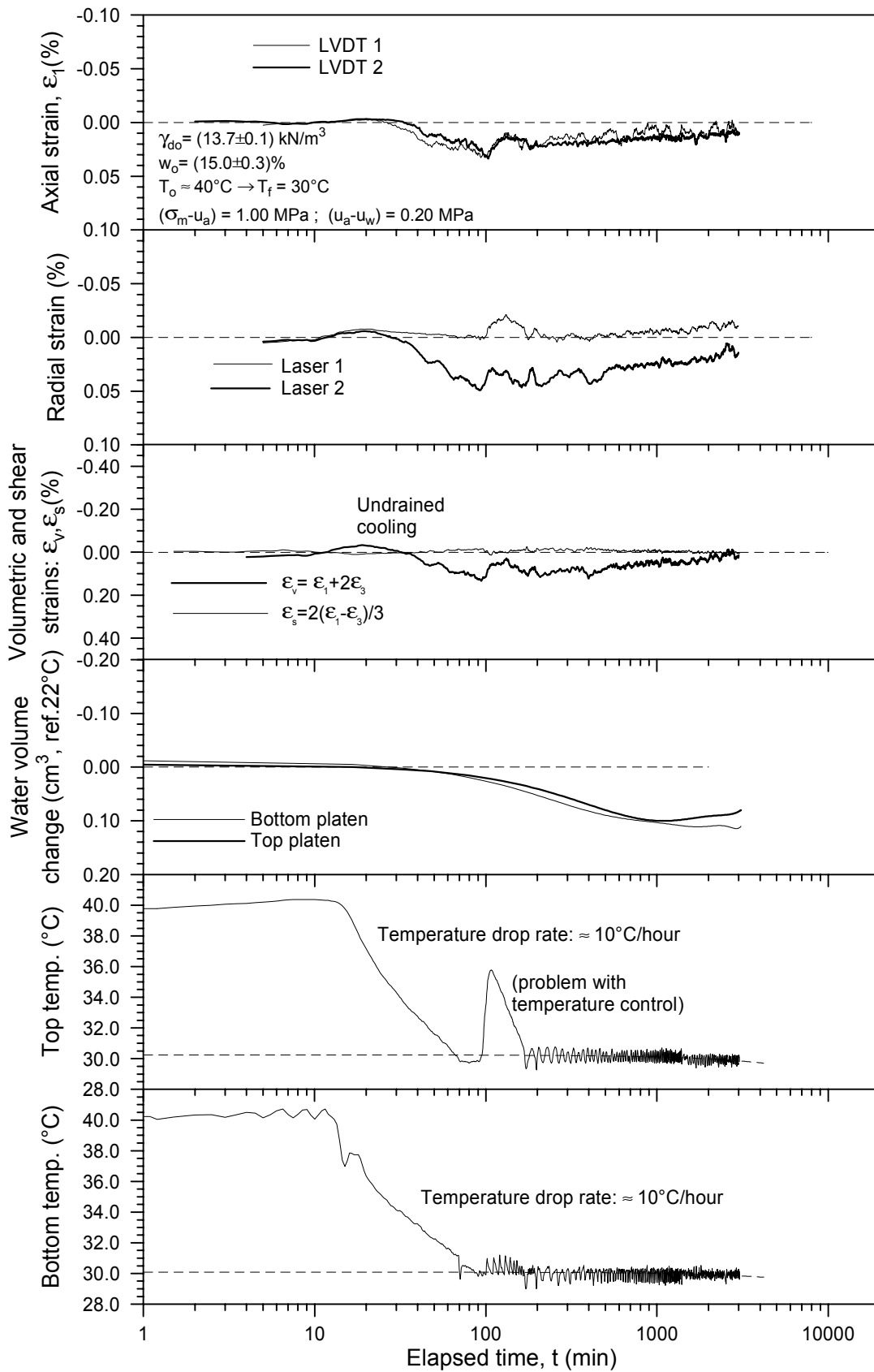
Figure 7.34   Time evolution of strains and water volume change during cooling and regulation phase at p = 1.00 MPa and s = 0.20 MPa (40°C to 30°C in path E-F).

Figure 7.35   Time evolution of strains and water volume change during cooling and regulation phase at p = 1.00 MPa and s = 0.20 MPa (30°C to 20°C in path E-F).
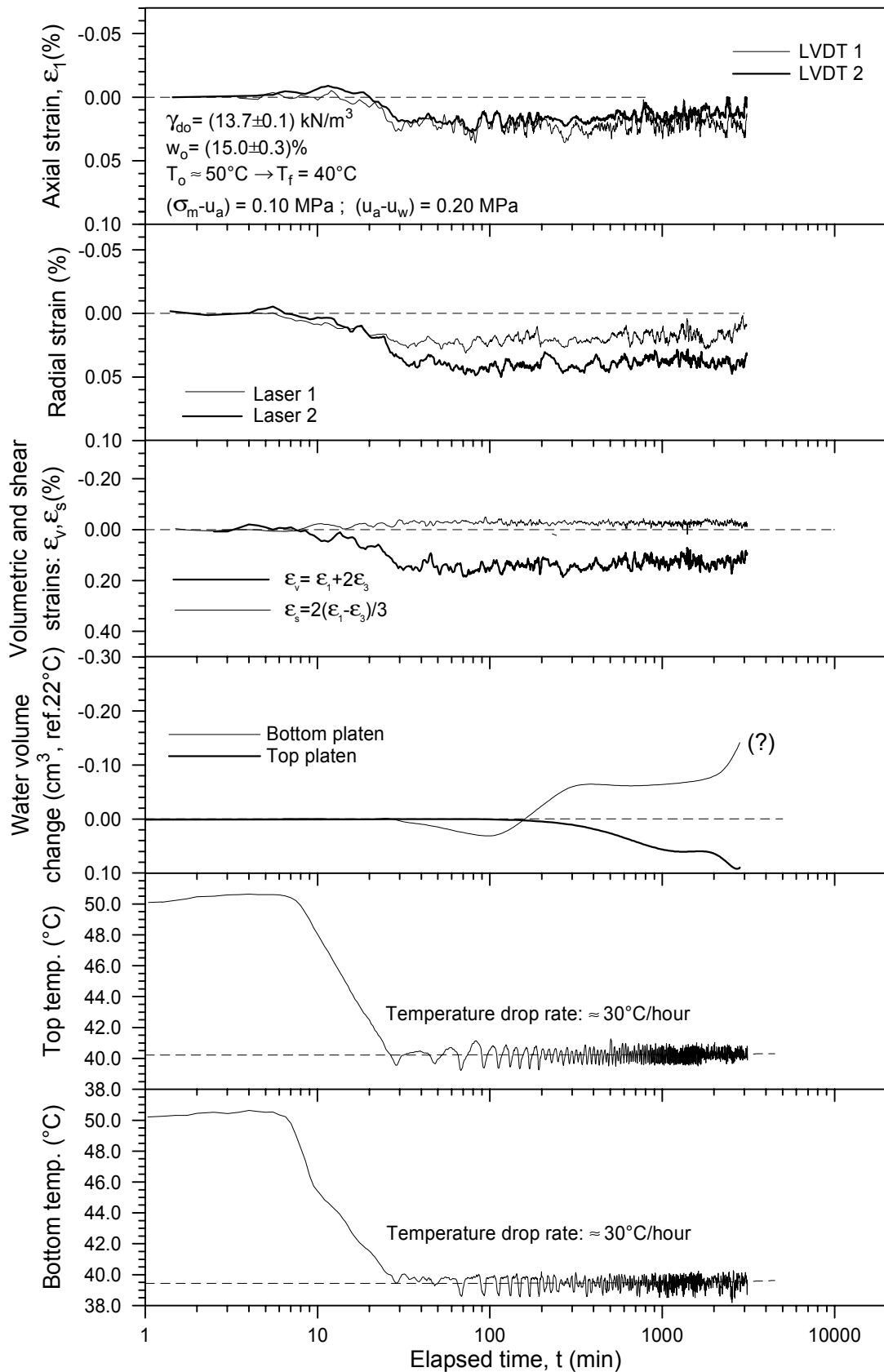
Figure 7.36   Time evolution of strains and water volume change for an overconsolidated state during heating and regulation phases at p = 0.10 MPa and s = 0.20 MPa (22°C to 30°C in path G-H).
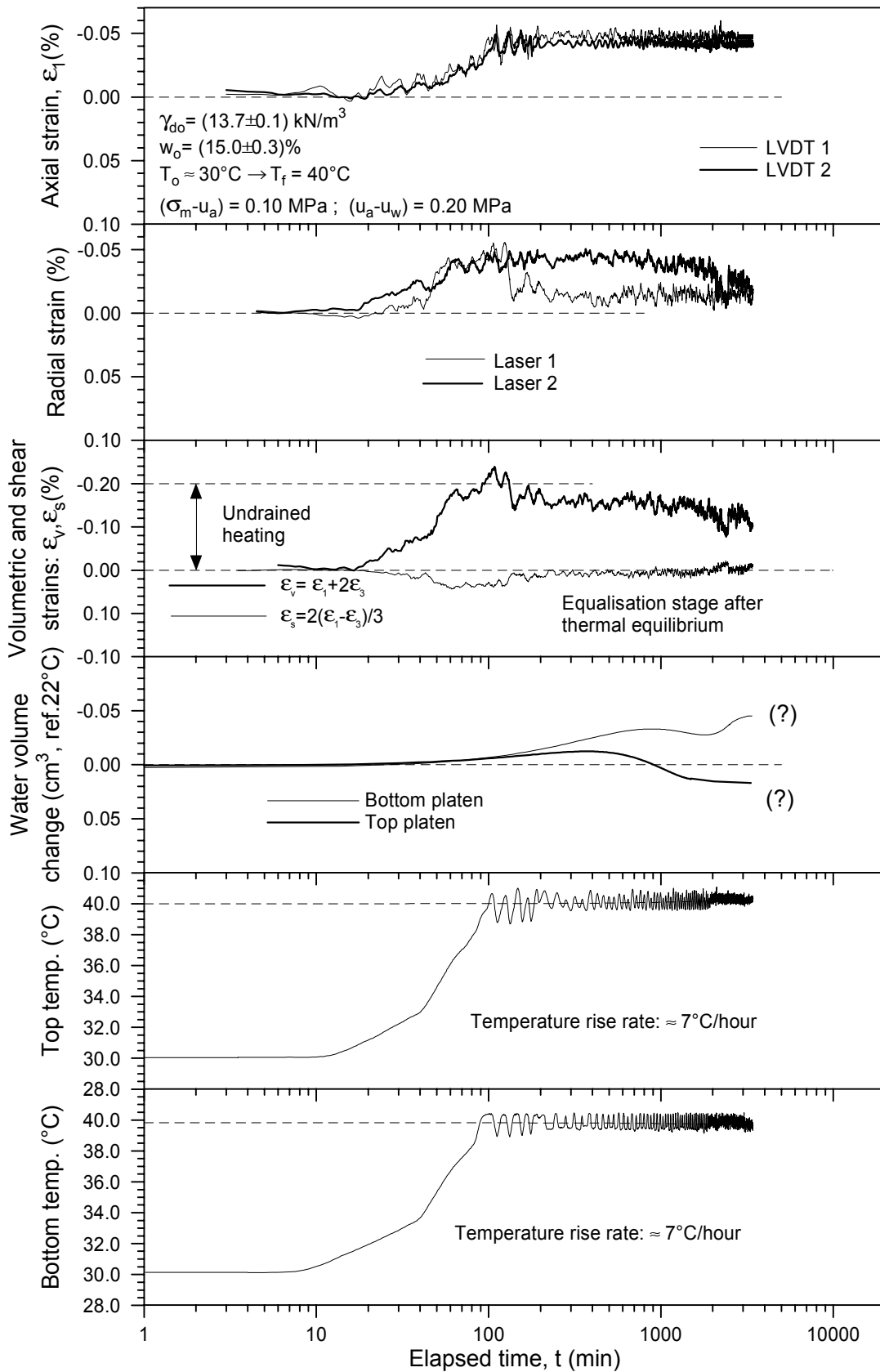
Figure 7.37   Time evolution of strains and water volume change for an overconsolidated state during heating and regulation phases at p = 0.10 MPa and s = 0.20 MPa (30°C to 40°C in path G-H).
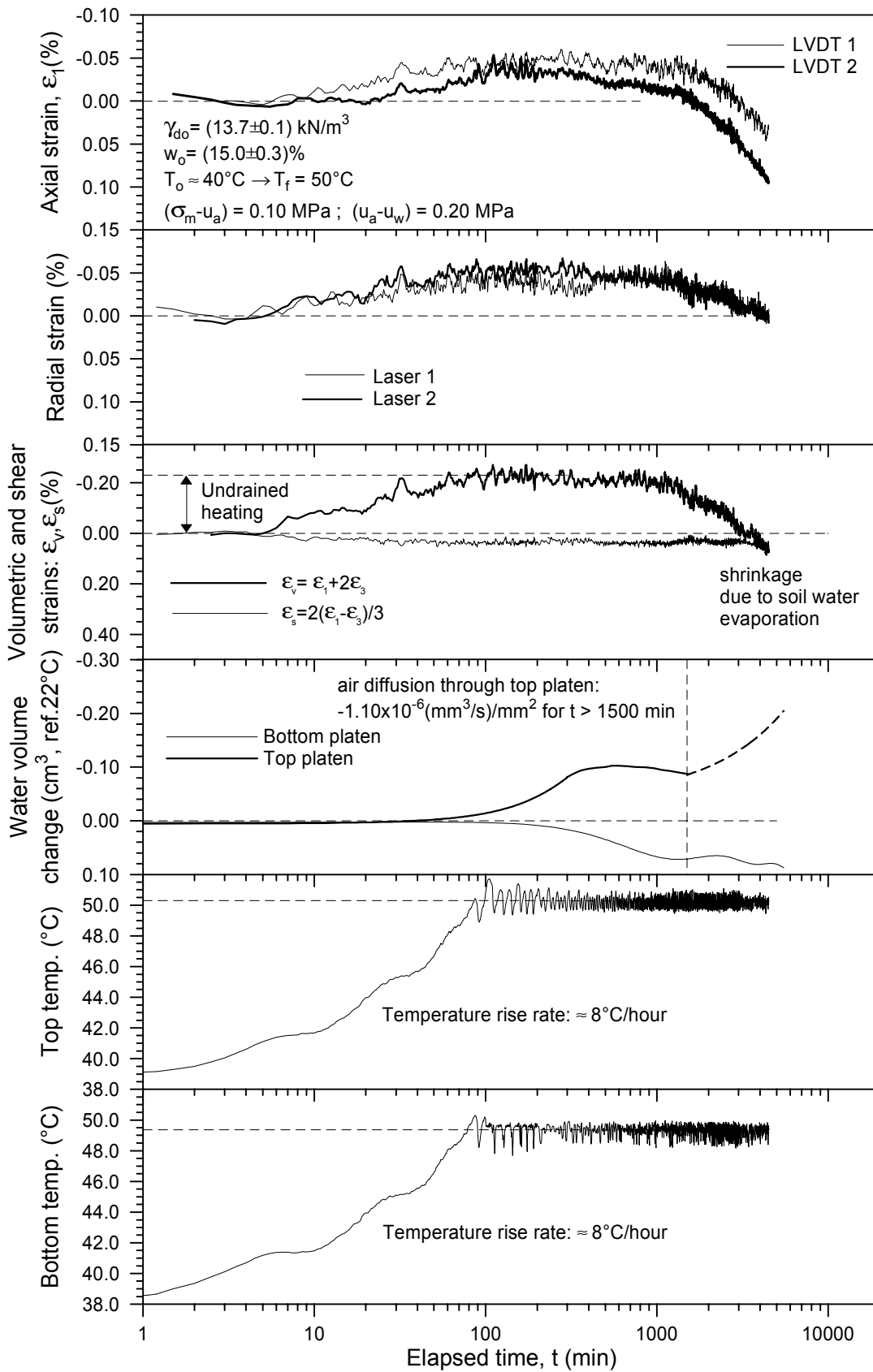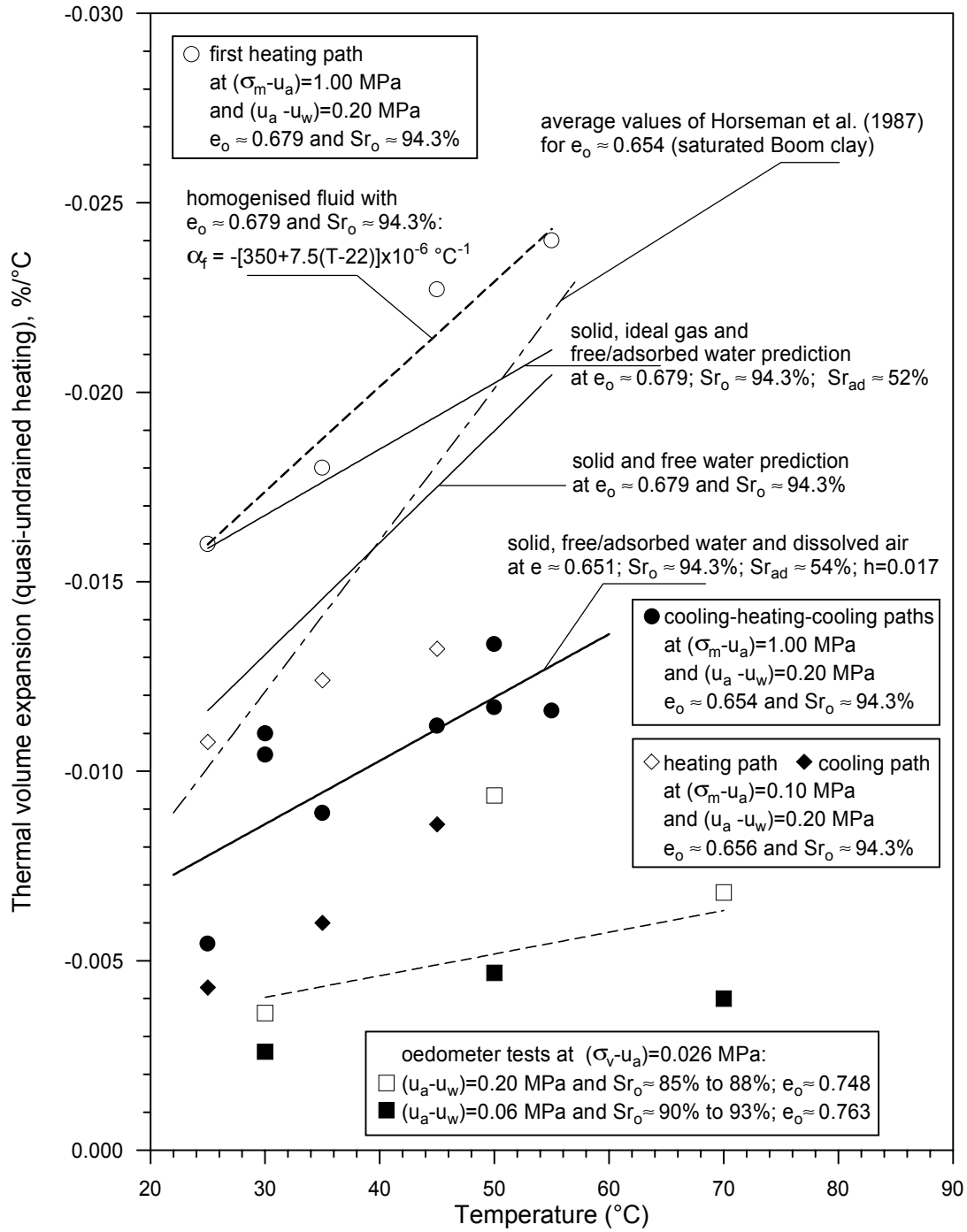
Figure 7.38   Time evolution of strains and water volume change for an overconsolidated state during heating and regulation phases at p = 0.10 MPa and s = 0.20 MPa (40°C to 50°C in path G-H).

Figure 7.39   Time evolution of strains and water volume change for an overconsolidated state during cooling and regulation phases at p = 0.10 MPa and s = 0.20 MPa (50°C to 40°C in path H-I).

Figure 7.40   Thermal volume expansion coefficients under quasi-undrained heating conditions plotted against different temperatures.
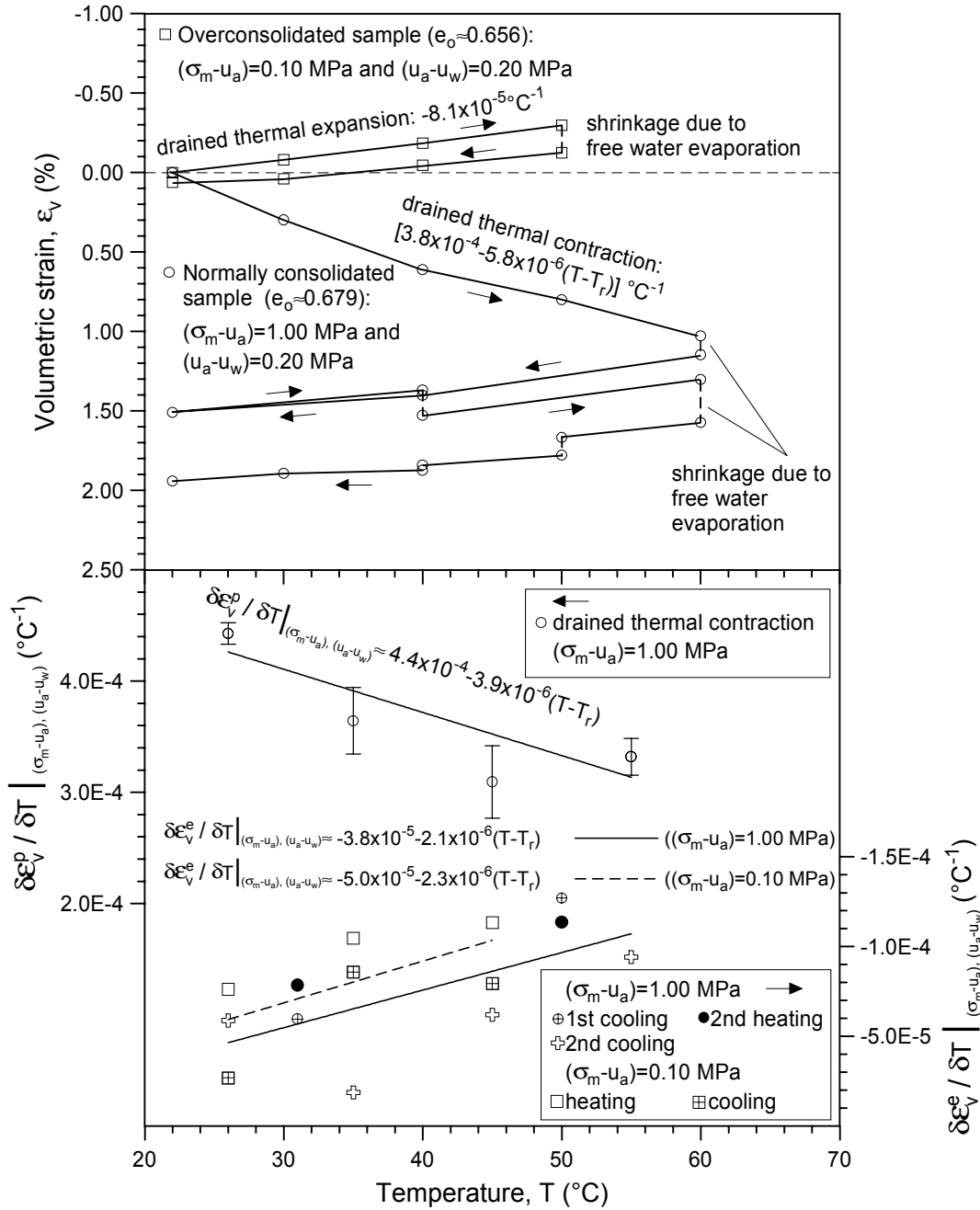
Figure 7.41   Drained volumetric thermal strains versus temperature for normal and overconsolidated states.
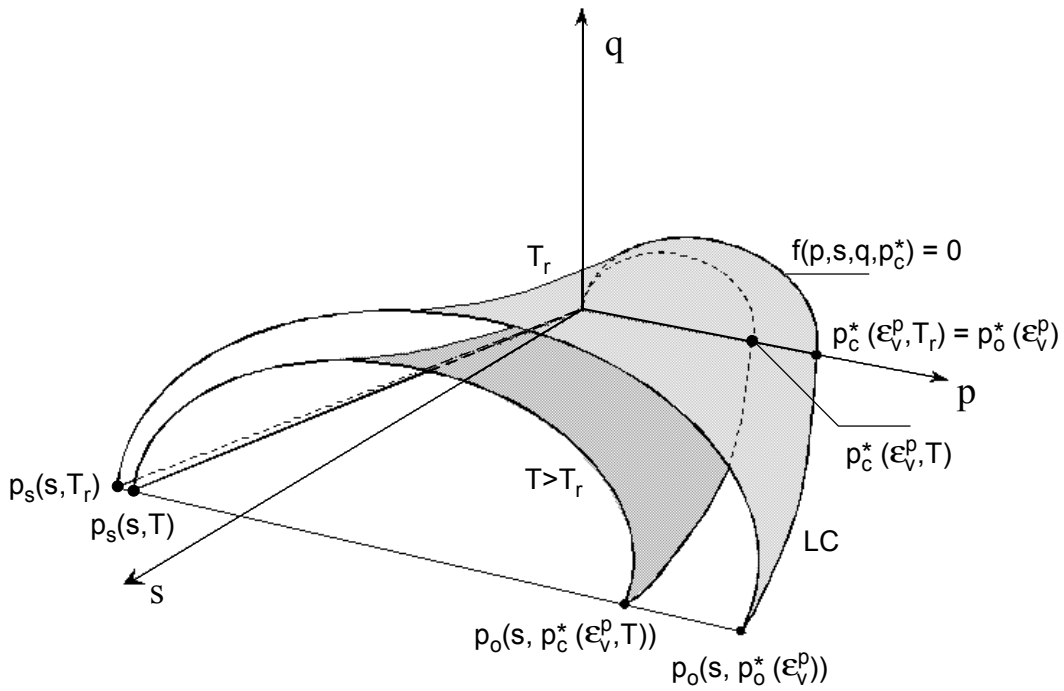
Figure 7.42   Three-dimensional view of the yield surfaces in (q, p, s) stress space at different temperatures.
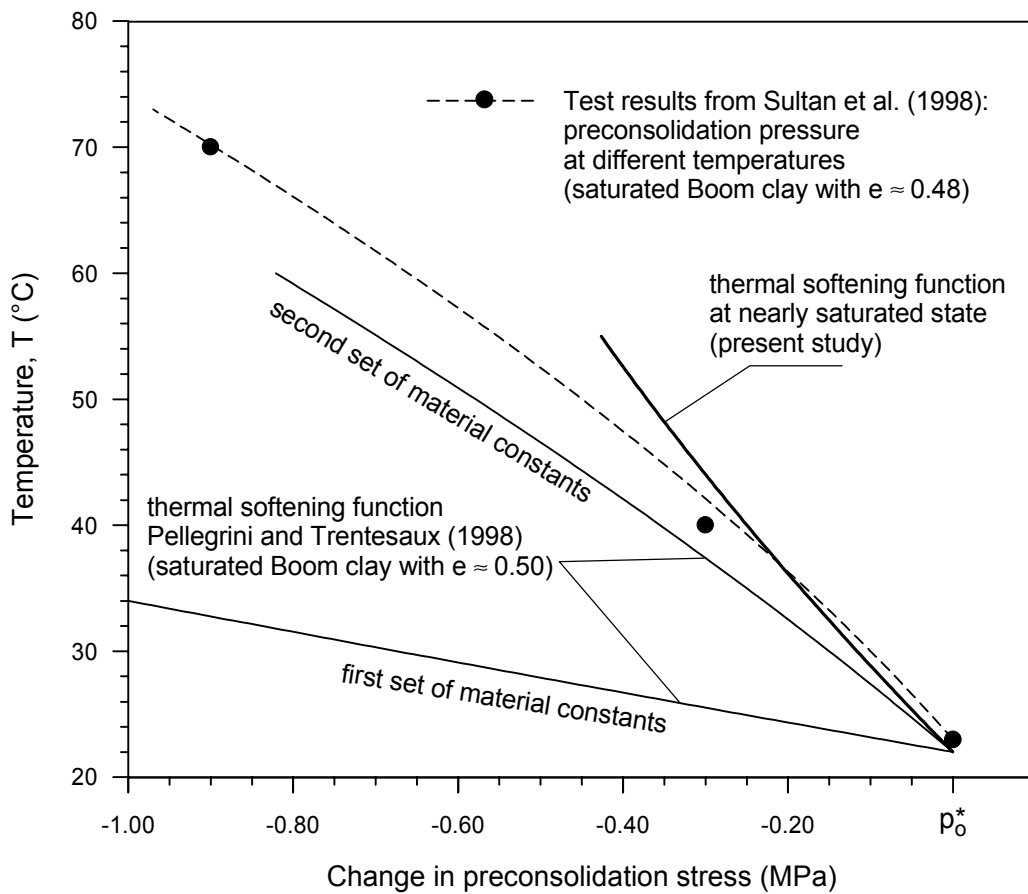

Figure 7.43   Thermal softening functions compared to measured values of preconsolidation pressure changes induced by temperature.